Alma Mater Studiorum – Università di Bologna

School of Science
Department of Physics and Astronomy (DIFA)
Master's Degree Program in Astrophysics and Cosmology

Determination of the potential habitability of super-Earths

Presented by:
Julien Boughon

Supervisor:
Prof. Leonardo Testi

ACADEMIC YEAR 2023-2024
Graduation date III

Abstract

One of the most fundamental questions of science remains the existence of any lifeform beyond the Earth. The numerous detections of exoplanets since the discovery of 51 Pegasi b in 1995 has deeply increased the credibility of the research on habitable worlds in our Galaxy. As such, the diversity of the exoplanet populations, ranging from low-mass planets such as super-Earths and sub-Neptunes to high-mass planets such as Neptune-like/sub-Neptune planets and hot Jupiters has improved our understanding of planetary systems, in particular planet formation theory. Consequently, there is a wide range of planetary systems architectures, all drastically different from the Solar System configuration, emphasizing the uniqueness of our planetary system.

The discovery of super-Earths, exoplanets with masses and sizes greater than Earth's but significantly lower than that of Uranus and Neptune, has opened new perspectives for searching planetary habitability beyond our Solar System. Through a comprehensive review of exoplanetology literature, this thesis investigates the potential for super-Earths to harbor habitable surface conditions by identifying fundamental parameters, as represented in the "planets are hard" diagram from Meadows & Barnes (2018), published in Springer Nature. This diagram includes planetary properties such as internal structure and atmospheric composition; planetary system architecture; and stellar activity effects on long-term habitability. Therefore, after a synthetic view of theoretical frameworks of the current literature of exoplanetary research, including detection methods and exoplanet populations, this work aims to provide a global understanding of the conditions leading to habitability on super-Earths' surface, expanding our knowledge of both astrobiology and exoplanetology fields.

Ultimately, this compilatory thesis explores the Nasa Exoplanet Archive database to estimate the number of super-Earths that could be considered potentially habitable by applying a primary reasoning on the stability of liquid water, thus based on their equilibrium temperature. A python program named habitabilita24 is implemented to analyze this database in addition to determine the number of potential habitable zone-planets by considering their eccentricity. The results indicate that ten super-Earths can potentially harbor habitable conditions and that 798 exoplanets could be located in habitable zone, which is a promising prospect for the search for life beyond the Solar System.

Contents

Chapter 1

Introduction

1.1 Planets in the Solar System

When it comes to studying planetary systems, the only stellar system benchmark we must consider is our own Solar System, which shows quite a unique architecture. Indeed, its architecture comprises four inner terrestrial planets and four outer gas giants, that are Mercury, Venus, Earth, Mars, Jupiter, Saturn, Uranus, and Neptune, respectively. First, terrestrial planets present solid surfaces and are differentiated into three internal layers: a metallic core, silicate shell (mantle and crust) and a volatile envelope of gases and ices. In the case of the Earth, a supplementary layer indispensable for habitability is found: a layer of liquid water [1]. The bulk composition of terrestrial planets, mostly oxygen, iron, silicon, magnesium and other minor chemical elements, including aluminum, calcium, sulfur and nickel, is consistent with the composition of chondrites. Chondritic meteorites are essentially the building blocks of terrestrial planets [1]. On the other hand, gas and icy giants are mostly made of gas such as hydrogen and helium in their atmosphere and interiors [2]. In addition to planets there are also minor bodies such as asteroids and dwarf planets: numerous asteroids are eccentrically orbiting between the orbits of Mars and Jupiter in the so-called main asteroid belt. However, other asteroids also come from the Kuiper belt region, where dwarf planets such as Pluto, Makemake or Eris are found beyond Neptune's orbit and are referred to as trans-Neptunian objects. The outer boundary of the solar system is known as the Oort Cloud, where a plethora of eccentric minor bodies is located, which is essentially a mix of asteroids, comets, or dwarf planets. According to the International Astronomical Union (IAU), with the declassification of Pluto, characterized first as a planet in 1930 by Clyde Tombaugh and retrograded to the dwarf planet nomenclature in 2006 because of its insufficient mass and its perturbed orbit, a planet can be defined based on the following criteria:

- A celestial body that is orbiting the Sun or any other star and is not able to sustain any nuclear fusion.

- Has a sufficient mass to hold hydrostatic equilibrium, that is the balance between the gravitational forces and the pressures forces.

- A planet has cleared out its orbital environment to maintain its orbit.

Currently, within the Solar System, Mercury, Venus, Earth, Mars, Jupiter, Saturn, Uranus, and Neptune currently satisfy the above criteria. The uniqueness of the architecture of the Solar System is also well emphasized by the fact that only one planet is known to be hosting life, present in many forms, structured from bacteria to humans, which is shown by complex biological life encountered on Earth. Besides, Earth being in the habitable zone, as well as Venus and Mars depending on the habitable zone model (section 3.1) but remain inhabited because of their extreme environmental conditions: severe greenhouse effect for Venus and

sterile and glacial environment for Mars. In other words, Venus is at the inner edge of the habitable zone and Mars at the outer edge of this habitable zone, as shown in figure 1.1.

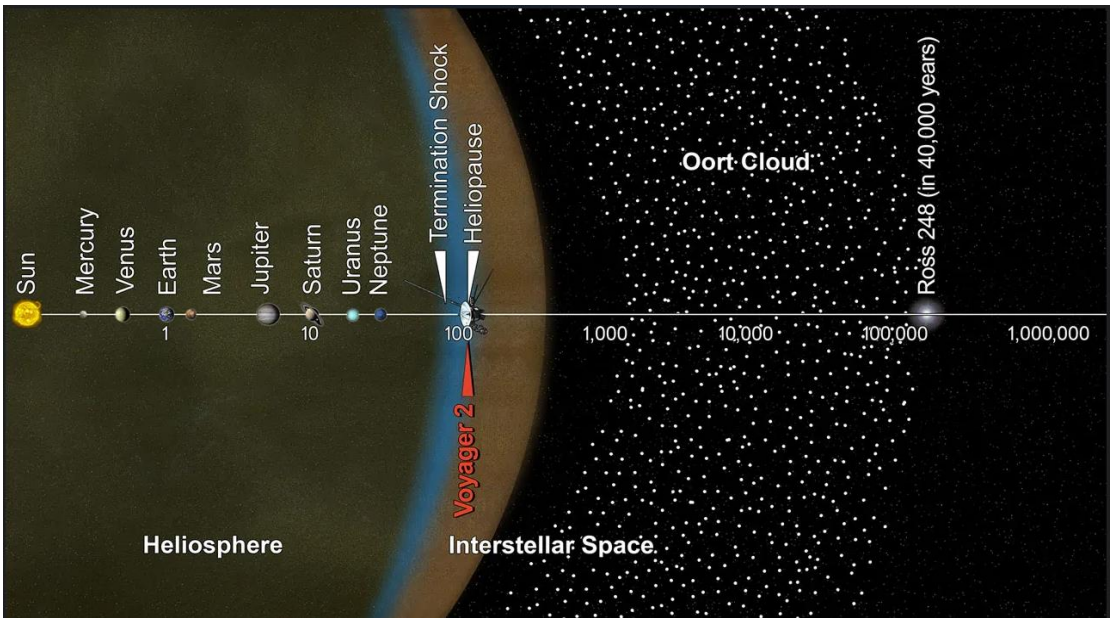

Figure 1.1: Artist's representation to scale of the solar system based on Voyager 2 mission data, where scaled-bar distances are indicated in astronomical units (AU). Image from [3].

1.2 Generalities on exoplanets

The field of exoplanetology was officially born with the detection of the first exoplanet around a main sequence solar-type star in 1995, a breakthrough accomplished by Michel Mayor and Didier Queloz at the Geneva Observatory. This new kind of planet appears to be drastically different than those of the Solar System and is called 51 Pegasi b [4]. This exoplanet is characterized as a hot Jupiter, located at 0.05 AU from its host star, 51 Peg, and has a minimum mass of 0.5 M_J (Jupiter's mass). It was detected through the radial velocity technique [4] that will be detailed in the next chapter. Since 1995, the number of detections has been increasing sharply thanks to the development of other detection methods such as planetary transit and gravitational microlensing. Nowadays, as reported in the NASA Exoplanet Archive [5], more than 5700 exoplanets have been confirmed. Therefore, the detection statistics are consistent with most stars hosting planetary systems. It strongly suggests that there could be billions of exoplanets in the Milky Way, which is very promising for the search of exolife. In other words, the large diversity of exoplanets raises the question of how many of these planets could host suitable conditions to develop life. It is relevant to note that the vast majority of known exoplanets do not present similar conditions to the ones in the Solar System, especially with that of the Earth, which is currently the only known planet to host life. Besides, the history of this relatively young scientific research field has been fully furnished over the years thanks to the elaboration of sophisticated instrumentation such as the Hubble Space Telescope (HST), Kepler Space Telescope (KST), and the James Webb Space Telescope (JWST). Furthermore, the detection of numerous extrasolar planets allows researchers to observe a wide range of populations and distinct architecture of planetary systems, as illustrated in figure 1.2. The figure shows the distribution of all confirmed exoplanets based on their mass M_p (expressed in Jupiter's mass) and their semi-major axis a_p (in astronomical units (AU)). We can notice that most planets comprise masses between $M_p = 0.01\, M_J$ and $M_p = 10\, M_J$, where M_J denotes

Jupiter's mass. Regarding the typical distance to their host star, most planets are located between $a_p = 0.01\ AU$ and $a_p = 10\ AU$. A much more detailed description of the numerous and most important exoplanet populations that are Neptune-like/sub-Neptunes planets, hot Jupiters and super-Earths will be performed in chapter 2.

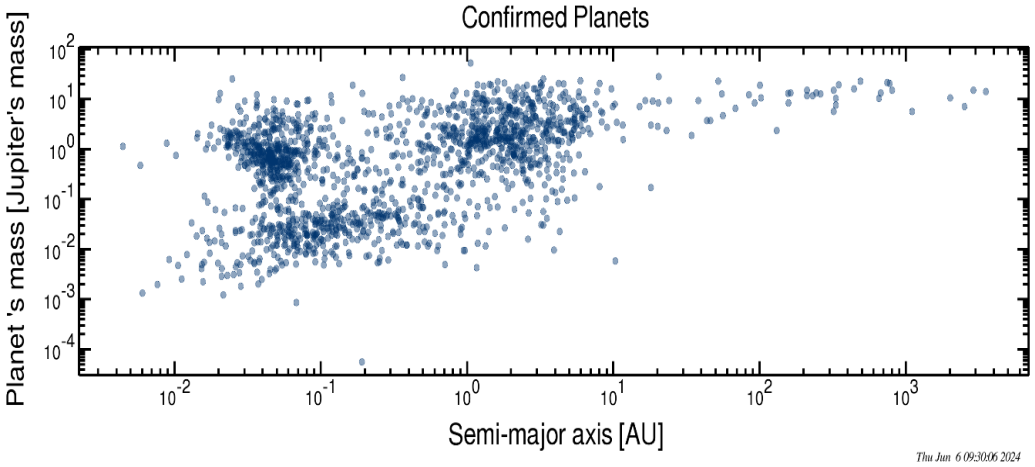

Figure 1.2: Distribution of confirmed planets as a function of their mass (y-axis) and their orbit's semi major axis (x-axis). Plot from [5].

1.3 Introduction to habitability and definition of life

One of the most important questions to investigate when studying extrasolar planets is the existence of life on these far worlds. As mentioned before, the only example of existing life is obviously proved by the presence of the Earth. Indeed, the first lifeforms appeared on our planet 3.8 billion years ago, which led life to develop under many forms throughout time, from an initial anoxic environment to an oxygen-rich environment during the Great Oxygenation Event, from Archean bacteria (during the Hadean period nearly four billion years ago) to current hominids [6], successively. Concretely, living organisms need specific molecules and nutrients such as carbon, nitrogen, hydrogen and oxygen, these molecules being brought by atmospheric composition (carbon and oxygen), water molecular structure (hydrogen and oxygen atoms) and the landmass that can deliver some nutrients [6]. Hence the following question yet to be investigated: where do the building blocks of life come from? Currently, there are two persuasive theories trying to elude this origin: the abiogenesis and the panspermia theories. The abiogenesis theory [7] proposes a chemical origin of life, where organic elements are produced from inorganic matters through physicochemical processes, leading to their reassembling into complex organisms. One piece of evidence of this theory is the fact that some amino acids can be synthesized within an inorganic environment, as it was the case during early Earth [7]. This remarkable result was demonstrated by the Miller-Urrey experiment in 1953 to reproduce the primitive conditions on Earth [7]. On the other hand, the panspermia hypothesis suggests an extraterrestrial origin of organic compounds: primitive life could have existed into the Solar System or in the Milky way and could have been brought by meteorite or asteroid impacts, either coming from the Solar System or our Galaxy [8]. As a result, life must have survived though extreme conditions. Despite its richness on Earth, the notion of life is quite complex to define but we could define it as a system that can reproduce itself and evolves into a given

environment, which is consistent with the Darwinian point of view. Based on the study of life on Earth, habitability requires three major criteria. The first criterion is the need of liquid water on the surface of the planet, conditioned by an average equilibrium temperature allowing the liquid state of this latter. From a chemical point of view, water is available in liquid state for temperatures between 273 K and 373 K. The equilibrium temperature is dependent on the atmospheric pressure and on the amount of stellar radiation received by the planet. It is important to note that stellar radiation is conceptually different from the solar wind since this latter consists in the emission of charged particles (protons, electrons and ions), which is detrimental to planet's atmospheres as it can lead to erosion. Then, habitability also depends on whether there is a greenhouse effect, potentially affecting the stability of liquid water and the average equilibrium temperature. For instance, Earth's equilibrium temperature is equal to 255 K. However, by taking the greenhouse effect into consideration, this equilibrium temperature increases to 288 K. This value is essentially the temperature of Earth's surface. The detailed derivation of planet's equilibrium temperature will be presented in chapter 2. The last criterion for habitability is the presence of fundamental chemical elements such as carbon, hydrogen or oxygen since they are part of fundamental biochemical reactions, indispensable for building any complex life.

1.4 The habitable zone and the search for habitability in the solar system

From an astronomical point of view, Earth is located in the so-called habitable zone, defined as the distance from the host star allowing the existence of surface liquid water and depending on the architecture of the planetary system. However, a planet evolving in the habitable zone does not necessarily imply that it is habitable since the three previously criteria need to be matched. In our Solar System, early Mars was thought to be habitable with a huge among of liquid water, which was also thought to be the same environment on Venus' surface. It is interesting to point out that Venus and Mars, although being located respectively on the inner and outer edges of the habitable zone, are not habitable because of events that occurred during their geological history. Thus, the location of a planet in the habitable zone is not necessarily a criterion for defining habitability. Contrary to Venus and Mars, other celestial bodies of the solar system such as Europa, Enceladus and Titan are currently investigated for their potential habitable conditions (presence of water in the crust of Europa or clouds of methane on Titan) even though they are located beyond the habitable zone.

1.4.1 Mars

In the case of Mars, based on telescopic observations, spacecrafts data and rover studies, Mars surface shows interesting geological features: indeed, its surface is covered by giant outflow channels and polar ice caps, suggesting that Mars was likely habitable, probably covered by a huge ocean. The large quantity of liquid water was probably removed by blowoff erosion, transforming Mars into an inhospitable present-day planet with its very low surface temperature and pressure in addition to the presence of a very thin atmosphere due to the destruction of a potential past magnetic field. Then, it implies that the large quantity of liquid water was conditioned thanks to a large greenhouse effect in Mars history and was significantly larger than today: indeed, the current surface temperature of Mars is 215 K. However, the understanding of the removal of water is quite complex and probably involves the photodissociation process, defined as the removal of hydrogen by a variety of potential thermal and non-thermal removal mechanisms in addition to the removal of oxygen via non-thermal mechanisms related to the interaction with the solar wind. From a theoretical point of view, it is demonstrated that the early atmosphere of Mars was probably removed hydrodynamically

during its history because of intense solar UV radiation and a powerful solar wind [9]. Regarding Martian magnetic field, based on the Mars Global Surveyor, little evidence of crustal magnetization is found inside the giant impact basins such as Hellas, Utopia and Argyre. The age of these basins, determined from the density of smaller subsequent formed craters, is a key parameter which shows that during the first few hundred million years, Mars was made of a geodynamo, comparable to that of current Earth's. The heat flux between the core and the mantle eventually decreased sharply, leading to the termination of the convection process driving the planetary magnetic field. Therefore, magnetic field dissipated within 50,000 years, between 3.9 and 4.1 billion years ago [9].

1.4.2 Venus

As emphasized by telescopic and orbiter observations, the current extremely hot surface temperature of Venus of 750 K in addition to its 96.5% carbon dioxide-dominated atmosphere genuinely allows researchers to qualify it as an inhospitable planet for the existence of life. To reach a dramatically high surface temperature, Venus must have evolved under a severe greenhouse effect epoch. The investigation of potential past Venus' habitability period remains a primordial question and remains indubitably related to the climate history of Venus.
Currently, two main scenarios can be considered and are focusing on the post-accretion magma ocean with different timescales for its crystallization [10]. If the crystallization of the magma ocean takes 100 million years or more, dissociation and the loss of the primordial water steam atmosphere are likely to occur. The result is the escape of hydrogen, as well as oxygen escape, while leftover oxygen can be absorbed by the magma ocean [10]. After the crystallization and the cooling of the magma ocean, Venus may have been inheriting a carbon dioxide-dominated thick atmosphere as observed today. Interestingly, a possible remnant of the CO_2 + steam H_2O is the D/H ratio measured by Donahue et al in 1982 [10]. Alternatively, if the timescale for crystallization of the magma ocean is taking place over 1 million years, this scenario drastically differs of the first scenario because the loss of the steam atmosphere is avoided [10], which may condense out onto the surface, leading to an undetermined duration for a period of habitability [10]. Overall, the transition from a post-magma ocean to a habitable environment remains an broad question. The DAVINCI (Deep Atmosphere Venus Investigation of Noble Gases Chemistry and Imaging) mission, scheduled for launch in a few years, will study the origin, evolution and present state of Venus from the top clouds to the surface.

1.4.3 Icy satellites

Then, Europa satellite of Jupiter, Enceladus, and Titan, satellites of Saturn, are icy worlds which may contain an ocean under an icy surface layer in the case of Europa and Enceladus. Indeed, in the case of Europa the combination of previous measurements of induced magnetic field and images obtained by remote sensing of surface features by the Galileo spacecraft support the theory that it may harbor liquid water ocean under an icy crust [11].
Similarly, Enceladus has a subsurface of liquid ocean as revealed by the completeness of the Cassini-Huygens mission data. In addition to liquid water underneath its surface, Enceladus presents free energy sources and bioessential elements [12]. All these findings, as well as the promising modeling of the submarine hydrothermal activity that shows viable sites for generating prebiotic chemistry and a possible origin of life, contribute to the characterization of the icy moon as a potentially habitable environment [12]. Interestingly, many theoretical studies and experiments indicate that the internal ocean of Enceladus could host habitable conditions for various species of Earth's microbial organisms like hydrogenotrophic methanogens [12]. Furthermore, Enceladus has a puzzling phenomenon occurring at its surface:

plumes of water are ejected from the interior. The study of such plumes could help us sample its interior and pursue the search for molecular biosignatures [12].
The atmospheres of these icy bodies (although relatively thin for Europa and Enceladus) are primarily composed of hydrogen and helium and nitrogen (for Titan), but also of methane, which acts as a tracer for life since methane can decay into complex hydrocarbons such as cellulose or glucose, especially on Titan where rains of methane are occurring.
However, if there was life on Titan it would be very different from the Earth and would not present an organic chemistry based on water. Liquid water, as a universal solvent, is the most essential ingredient for the development of life, as seen on our planet. Despite its current low average temperature of 100 K, the most promising habitable icy satellite in terms of space exploration mission capability is probably Europa: indeed, it could maintain liquid water ocean composed of sodium chloride on the top of water (like in Earth's oceans) under its relatively thin ice shell with a typical thickness estimated to ten kilometers. Therefore, the tides generated by Jupiter's gravitational interaction are thought to be the source of energy that stabilizes liquid water at such depth [13].

1.5 Thesis plan

We summarize here the structure of the thesis work, with a brief description of the contents of each chapter:

• In Chapter 2, the most fundamental notions of exoplanetology are reviewed to understand the pillar concepts of planetary detections by contrasting the observations between ground-space telescopes and space-based telescopes. Finally, we will present the main exoplanetary populations, including Neptune-like planets, hot Jupiters and super-Earths. A complementary comparison with respect to the planets of the Solar System will be made to better understand the physical characteristics of these exoplanets, especially by constraining their internal structure and atmospheric composition.

• In Chapter 3, we will investigate the potential habitability of super-Earths by first dealing with the notions embedded within the framework of planetary system dynamics, especially by focusing on the tidal effects of exomoon on planetary habitability and presenting current models on the habitable zone, both in terms of local and galactic locations. Then, we will discuss the impact of stellar activity on planet's habitability by providing a brief overview of stellar evolution theory and discussing the effects of long periods of high-stellar activity with a major focus on M-dwarf stars. Finally, we will analyze the Nasa Exoplanet Archive by implementing a python program aimed at determining the number of potentially habitable super-Earths and habitable zone-exoplanets.

• In Chapter 4, we will draw the conclusions on this work and present future developments and future scheduled space missions dedicated to find habitable extrasolar planets.

Chapter 2

Fundamental concepts of exoplanetology

In this chapter, we will review some important concepts of exoplanetology needed to describe thoroughly the use of the main exoplanet's detection methods which aim to accurately characterize them. Then, we will describe the diversity of exoplanets populations, ranging in size from super-Earths to hot Jupiters. An overview of their bulk composition as well as their atmospheric composition will also be performed alongside a statistical overview.

2.1 Detection methods

2.1.1 Planet's equilibrium temperature

First, the direct imaging method, despite its straightforwardness, is quite a relevant method to derive planet's equilibrium temperature T_{equi}. The equilibrium temperature is defined as the temperature for which an isothermal planet is in thermal equilibrium with the stellar host star radiation.

Let us consider a planet located at a distance r to the host star rotating on its inclination axis with a solid angle $d\Omega = \frac{\pi R_p^2}{r^2}$, R_p denotes the planet's radius. It then receives the irradiance energy E^{input} from its star of luminosity L_* and radius R_*. Since we are assuming the planet and the star are in a state of thermal equilibrium, the output energy emitted by the planet E^{output}, also known as the energy loss, transmitted in the form of its intrinsic luminosity L_* , is equivalent to the stellar insolation energy E^{input}:

$$E^{input} = E^{output} \Leftrightarrow \frac{d\Omega}{4\pi}(1-\alpha_B)L_* = 4\pi R_p^2 \sigma_{SB} \epsilon T_{equi}^4 \quad \text{(i.1)}$$

$$\Leftrightarrow \frac{1-\alpha_B}{r^2} L_* = 16\pi R_p \sigma_{SB} T_{equi}^4 \quad \text{(i.2)}$$

$$\Leftrightarrow \boxed{T_{equi} = \left(\frac{(1-\alpha_B)L_*}{16\pi r^2 \sigma_{SB}}\right)^{\frac{1}{4}}} \quad \text{(i.3)}$$

where $\sigma_{SB} = 5.67 \times 10^{-8} Wm^{-2}K^{-4}$ is the Stefan-Boltzmann constant. As we will study habitability in detail in chapter 3, the equilibrium temperature is an important parameter factor for setting habitable conditions but only remains a first order estimate of the planetary temperature. Overall, formula (i.3) is valid for a planet that is considered as a black body, reradiates over 4π steradians, assumes that the atmosphere is fully efficient at redistributing energy from the dayside to the nightside of the planet and does not take greenhouse warming effect into account.

2.1.2 Direct imaging

2.1.2.1 Notions of contrast factor and magnitude

Directly imaging an extrasolar planet remains a significant challenge because of the huge difference of the planet's brightness with respect to that of its host star. Star's luminosity is due to the internal nuclear fusion reaction process while the planet's emission can either be due to reflection of a fraction of the stellar light to space, i.e the Bond albedo, or due to intrinsic thermal emission resulting from the cooling of the young planet after its formation [14]. The contrast factor f is defined as the ratio between planet's flux F_p and the stellar flux F_* and can be computed as:

$$f = \frac{F_p}{F_*} = f_{\oplus,optical}(\frac{R_p}{R_\oplus})^2(\frac{r}{1AU})^2\alpha_B, \quad (1.0)$$

where R_p is planet's radius, r the planet-star distance, $R_\oplus$ denotes the Earth's radius, $f_{\oplus,optical}$ the contrast factor of the Earth in the visible part of the electromagnetic spectrum, and α_B the Bond albedo, which represents the fraction of stellar light scattered out by the planet. The left side of the formula is the general formula for the contrast factor while the right side represents the contrast factor in the case of the solar system observed in the optical. In the case of the Earth, it can be estimated that roughly 30% of Sun's light is reflected and we obtain a contrast factor of the order of $f = 1.4 \times 10^{-10}$. Thus, the (1.0) formula can be rewritten by taking the Earth and the solar system as references and by considering the reflected stellar light emission by the planet:

$$f = 1.4 \times 10^{-10}(\frac{R_p}{R_\oplus})^2(\frac{r}{1AU})^{-2}\frac{\alpha_B}{0.3} \quad (1.1)$$

Overall, the contrast factor being a ratio between the incident flux $F_P = \frac{L_*}{4\pi r^2}$ and irradiance $F_* = \frac{L_*}{4\pi r^2}$, it can be simplified as the ratio between planet's radius R_P and the stellar radius R_*:

$$f = (\frac{R_P}{R_*})^2 \quad (1.1.1)$$

The apparent magnitude m, which quantifies how much a body is brighter to another, is related to the contrast factor f by a logarithmic scale:

$$m = -2.5\, log(f) \quad (1.2)$$

In the optical window of the electromagnetic spectrum, Earth is 24.6 times fainter than the Sun. Given the extremely low value of the contrast factor in the visible spectral band, it is relevant to observe an exoplanet in other windows such as in the mid-infrared (MIR), where the contrast factor is much higher. For instance, the Earth with respect to Sun's flux, in the mid-infrared, has a contrast factor equal to $f_\oplus = 10^{-6}$, which leads to a magnitude difference $\Delta m = 15$, meaning the Earth is only 15 times fainter than the Sun.

We can also express the contrast factor in terms of black body emission: indeed, it is a good approximation which states that a body can absorb all incident radiation, acting as an ideal absorber. The spectrum generated by a black body is characterized as a continuum spectrum, in which the body emits at all wavelengths. Subsequently, the brightness distribution $B_\nu(T)$ of the body can be computed thanks to the application of Planck's law, depending on the frequency ν of the radiation and the effective temperature T:

$$B_\nu(T) = \frac{2h\nu^3}{c^2}\frac{1}{exp[\frac{h\nu}{k_B T-1}]}\ J\,s^{-1}m^{-2}Hz^{-1}steradian^{-1}, \tag{1.3}$$

where h=6.63 × 10^{-34} J.s is the Planck constant and k_B=1.38 × 10^{-23} J K^{-1} the Boltzmann constant.

Besides, the contrast factor can be expressed through the black body approximation by considering equilibrium T_{equi} and surface temperatures T_{eff} of the planet, which is a truly relevant model when dealing with thermal equilibrium of a given body:

$$f = (\frac{R_P}{R_*})^2 \frac{B_\nu(T_{equi})}{B_\nu(T_{eff})} \tag{1.4}$$

Generally, the contrast factor may also be expressed at any wavelength λ as a function of the phase curve $\Phi(\alpha)$, where α is the phase angle:

$$f_\lambda = f_{0,\lambda}\Phi(\alpha) \tag{1.5}$$

Furthermore, it is well established that the planetary emission is either due to the reflection of the incident stellar light or due to intrinsic thermal emission. Consequently, the contrast factor can be re-written in terms of reflection and thermal emission respectively as [14]:

$$f_{0,\lambda,reflection} = A_{g,\lambda}(\frac{R_p}{a})^2 \quad \text{and } f_{0,\lambda,thermal} \simeq (\frac{R_p}{R_*})^2 \frac{T_p}{T_*}, \tag{1.6}$$

where $A_{g,\lambda}$ is the monochromatc geometric albedo, a the semi-major axis, T_p the planetary temperature and T_* the stellar surface temperature. The latter equality assumes observations on the Rayleigh-Jeans tail leading to the largest flux ratio. If we assume thermal equilibrium for the thermal emission, we obtain the following formula:

$$f_{0,\lambda} \simeq (\frac{R_p}{R_*})^2 (\frac{R_*}{a})^{\frac{1}{2}}[f(1-\alpha_B)]^{\frac{1}{4}} \tag{1.7}$$

2.1.2.2 Signal-to-noise ratio

As previously mentioned, disentangling the planetary signal from the stellar signal given the high magnitude difference is certainly a significant challenge, especially when we directly observe an exoplanet. One important notion when detecting photons is the signal-to-noise ratio. First, the signal comprises photon counts coming from astronomical resolved sources and the sky background, including Moon's light and unresolved astronomical sources. Then, the noise is defined as fluctuations due to Poissonian noise, taking Poisson statistics into account, and additional instrumental effects are also considered like detector's noise. The signal-to-noise ratio is expressed as:

$$SNR = \frac{S}{N} = \frac{S}{\sqrt{\sigma_S^2 + \sigma_B^2 + RON^2}} \quad , \tag{1.8}$$

where S is the Poissonian noise of the number of counts (photons on each detector's pixel) of the observed source, N the noise comprising the effects mentioned above, which in relation (1.8) contains the errors due to the counts of the source σ_S, due to the counts of the sky background σ_B and due to the counts on detector's pixel RON acting as an electronics noise. The formula obtained in (1.8) is rather a general formula but in the case of detecting an exoplanet with a sample of N measurements, the signal-to-noise ratio is then linked to the normalized contrast factor defined in (1.7) [14]:

$$\boxed{SNR =\simeq g\sqrt{N}\frac{f_{0,\lambda}}{\sigma_{eff}},} \tag{1.9}$$

where $g = [N^{-1}\sum_k \quad \Phi(\alpha_k)^2]^{\frac{1}{2}}$ is the root-mean-square of the phase function values at the times k of the observations and σ_{eff} the average effective per-measurement photon noise uncertainty normalized to the total stellar flux [14].

2.1.2.3 Targeted exoplanets and limitations

In addition to the paramount importance of the contrast factor, the other parameter needed for assessing the detectability of an exoplanet via direct imaging remains the angular separation between this latter and its star. This angular separation is then defined as:

$$\Delta\Theta = \frac{r_\perp}{d}, \tag{2.0}$$

where $r_\perp$ is the projected separation from the planet to the host star and d the distance between the observer and the stellar system. Given the large distance to stellar systems, the angular separation between the planet and the star turns out to be dramatically small, hence the use of the arcsecond unit if d is in parsecs and $r_\perp$ in AU. In the case of a circular orbit the angular separation becomes [14]:

$$\Delta\Theta = \frac{a(cos^2\beta + sin^2\beta cos^2 i)^{\frac{1}{2}}}{d}, \tag{2.1}$$

with β the angle between the position of the exoplanet along its orbit relative to the ascending node and i the orbital inclination angle, which is the angle between the orbital plane and the plane of the sky.

Therefore, observing exoplanets throughout the direct imaging technique requires to increase the contrast factor and increase the diameter D of any telescope. This leads to the decrease of the inner working angle of the imaging system defined by optics theory as:

$$\Theta_{IWA} \sim \frac{\lambda}{D} \tag{2.2}$$

Any instrumental part of an optical system is affected by the diffraction process and the wave nature of light that limits its angular resolution. Generally, the diffraction-limited angular resolution is expressed as:

$$\boxed{\Theta_{diff,lim} \approx 1.22\frac{\lambda}{D}} \quad (2.3)$$

It is easily shown that young and self-luminous exoplanets (< one billion years old) are the ideal candidates for direct imaging because they are hotter and brighter, leading them to emit significant amount of radiation [14] [15]. The MIR and infrared (IR) windows seem to be appropriate for detecting these planets because the thermal emission is easily detectable. In addition, only nearby young planets (located at $d \leq 100pc$) have been imaged in the last two decades [15].
In order to observe such planets, sophisticated instrumentation is required. This includes large telescopes that must fulfill major criteria that are high angular resolution, the mitigation of stellar light by using coronography technique and applying subtraction using differential imaging techniques [15]. These criteria are typically met by second-generation imagers such as the European Spectro-Polarimetric High-Contrast Exoplanet Research Instrument (SPHERE), the Gemini Planet Imager (GPI) and the Subaru Coronographic Extreme Adaptive Optics (SCExAO) instrument. The adaptive optics technique is necessary to mitigate Earth's atmospheric turbulence for ground-based telescopes. It has the disadvantage of degrading image quality and angular resolution. The functioning of adaptive optics is shown in figure 1.3.

Regarding the direct imaging of habitable planets in thermal equilibrium with their stars, it is shown from models that the signal-to-noise ratio, for respectively reflected light and intrinsic thermal emission, scales as [14]:

$$SNR_{reflection} = R_p^2 M_*^{-4} \quad \text{and} \quad SNR_{thermal} = R_p^2 M_*^{-\frac{5}{2}} \quad (2.4)$$

From equation (2.4), it strongly suggests that low-mass stars are favored. As mentioned earlier, the angular separation between the planet and the parent star is an important parameter for direct detection. Indeed, the angular separation must be larger than the inner working angle of the imaging system as expressed in (2.5) to detect the habitable planet. Thus, at a fixed mass it sets a maximum distance at which a habitable zone planet can still be detected [14]:

$$\boxed{d = 10\ pc\ (\frac{\Theta_{IWA}}{100mas})^{-1}(\frac{M_*}{M_{Sun}})^2} \quad (2.5)$$

Overall, the direct imaging method requires a large angular separation between the planet and the host star, and a high angular resolution typically calibrated with large telescopes, especially in the IR window. By considering planet's light emission, either from reflected starlight or intrinsic heat, direct imaging is statistically biased for distant planets from their host stars, as well as giant and young planets. Since young and massive planets are brighter, they are much more likely to be targeted by this specific detection method with a variety of imagers. In other words, it only samples local exoplanet populations in Sun's neighborhood, which represents distances up to 100 parsecs. Therefore, very few detections are available.

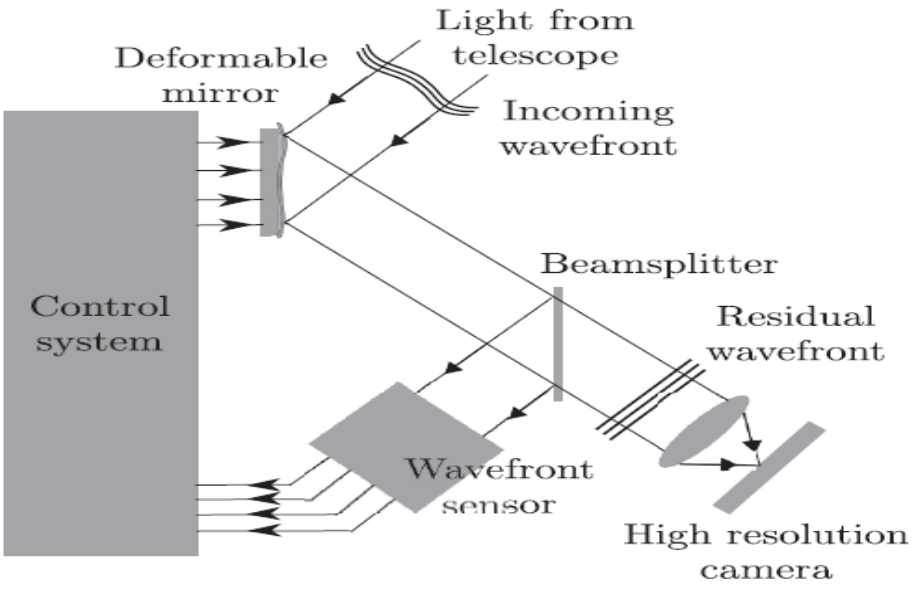

Figure 1.3: Adaptive optics system functioning. Image from [16].

The following table (figure 1.4) reports some of the Hubble Space Telescope (HST), JWST and the SPHERE imager from the Very Large Telescope (VLT), characteristics computed from formula (2.3). We consider the main imager of the JWST, NIRcam and one of the two main imagers of HST, WFC3 by taking the wider spectral channel, NIR. Let us recall 1 rad= 206265 arcseconds, which is denoted "as" or ''.

Telescope/Imager, spectral channel	Wavelength range $\Delta\lambda$ (μm)	Diameter D (m)	Angular resolution range $\Delta\Theta_{diff,lim}$ (as)
HST/WFC3 NIR	[0.85, 1.70]	2.4	[0.09, 0.18]
VLT/SPHERE	[0.95, 2.32]	8.2	[0.03, 0.07]
JWST/NIRcam	[0.6, 5.0]	6.5	[0.02, 0.19]

Figure 1.4: Overview table of some instrumental characteristics of the HST, VLT and JWST in the NIR window. Data taken from [17] and [18].

2.1.3 Gravitational microlensing

2.1.3.1 Description of gravitational lensing

Gravitational lensing refers to the bending of light rays emitted from a background source by a foreground mass called the lens such as stars or galaxies. The deflection of light by a source mass produces a ring of light called Einstein ring around this latter. Historically, the existence of such phenomenon has been conclusively proved by Einstein's computations in 1936 although it was not seen before several decades later. Both a star and a planet behave as lenses, and they can both lens another further away star. For instance, in the case of exoplanets, the stellar light is deflected by the presence of an orbiting planet and produces the so-called magnification effect, as illustrated in figure 1.5. The term gravitational microlensing is relevant in the case of a planet passing in front of a background star because it is smaller and less massive than the star.

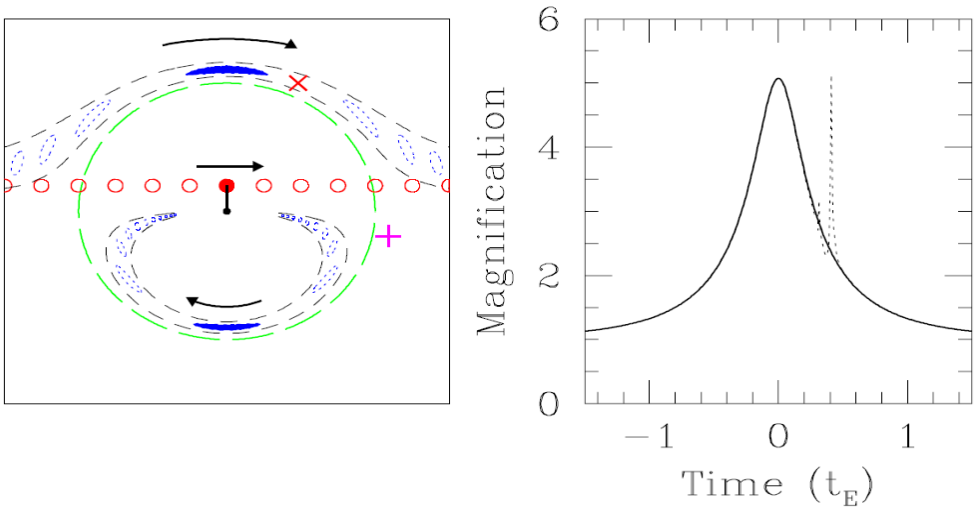

Figure 1.5: Left: The images (blue dotted ovals) are shown for different positions of the source (red solid circles), along with the primary lens (black dot) and Einstein ring (green long dashed circle). If the primary lens has a planet near the path of one of the images, i.e. within the black short-dashed lines, then the planet will perturb the light from the source, creating a deviation to the single lens light curve. Right: The magnification time variation is shown for the case of a single lens (solid) and companion planet (dotted) located at the position of the red X in the left panel. However, if the planet was located at the violet +, there would be no detectable perturbation, and the resulting light curve would be essentially identical to the solid curve. Plots from [19].

Concretely, the planet is passing in front of the star, which generates a variation of the stellar light with respect to time. Magnification, which is the ratio between the image area and the source area, is caused by the bending of the stellar light rays by the planet and presents a peak when the planet is located in front of the star. In the case of figure 1.5, only one peak is seen but, in some configurations, multiple peaks are present because of the presence of several lenses. Thus, the presence of several peaks enables to postulate the presence of a multiplanetary system. However, the alignment between two lenses is extremely peculiar, which makes derivation of statistics truly difficult.

2.1.3.2 Pills on gravitational lensing

As mentioned previously, the lens deflects the light of the background source, inducing the magnification effect. The configuration of gravitational lensing can be summarized in figure 1.6.

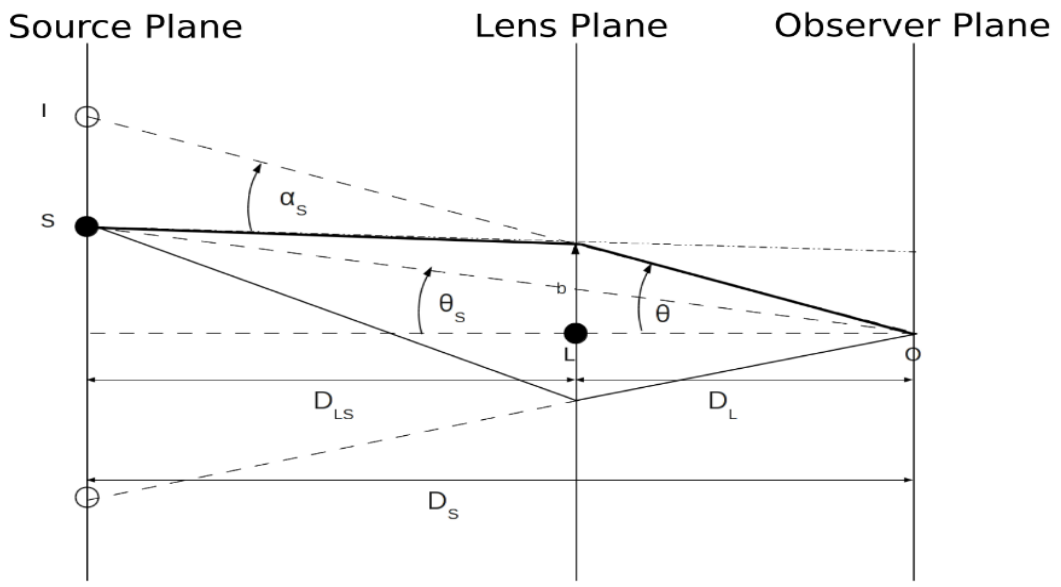

Figure 1.6: Detailed schematic of the gravitational lensing phenomenon. Image from [20].

From figure 1.6, it is possible to determine the angle of deflection caused by lens L on the light source located on point S. Since the distance to any source leads to a drastically small angle of observation, we will assume the Gauss approximation:

$$sin(\theta)\approx\theta\ ,\quad cos(\theta)\approx 1\ ,\quad tan(\theta)\approx\theta \tag{2.6}$$

According to general relativity theory, when a light ray from a bright source S interacts with the gravitational field induced by a massive body L, the light ray is bent by an angle approximately equal to [17]:

$$\alpha_S(b) = \frac{2r_S}{b}, \tag{2.7}$$

where r_S is the radius of the source and b is the light rays' impact parameter.

Let us assume the ideal case where there is a thin lens and noting that $\alpha_S(b)D_{LS} = (\theta - \theta_S)D_S$, it is then possible to derive the lens equation:

$$\theta_S = \theta - \frac{\theta_E^2}{\theta} \tag{2.8}$$

where θ_E is the Einstein ring radius and θ_S the source position.

The Einstein ring radius corresponds to the angular radius of the image when the lens and the source are perfectly aligned ($\theta_S = 0$) and is expressed by starting to consider the gravitational field produced by the lens. The bending angle defined in (2.7) can be re-written in terms of the gravitational potential [20]:

$$\alpha_S^{\wedge} = 2\int_{-\infty}^{+\infty} \nabla_{\perp}\Phi ds, \tag{2.9}$$

where ds is the metric defined such that $ds^2 = -(1+2\Phi)dt + (1-2\Phi)(dx^2+dy^2+dz^2)$

The gravitational potential is conventionally defined as:

$$\Phi(r) = -\frac{GM_L}{r} = -\frac{GM_L}{(b^2+z^2)^{\frac{1}{2}}} \quad , \tag{3.0}$$

where M_L is the mass of the lens.

The divergence of the gravitational potential is then simply equal to $\nabla_\perp \Phi = \frac{\partial \Phi}{\partial b} = \frac{GM_L b}{(b^2+z^2)^{\frac{3}{2}}}$.

By applying the substitution $b^2 + z^2 = 1 + x$ in (3.0), we obtain the following result for the deflection angle:

$$\hat{\alpha_S} = \frac{4GM_L}{c^2 b} \tag{3.1}$$

Besides, it is relevant to link the deflection angle with the angle θ so that the Einstein ring radius can be computed:

$$\alpha_S(\theta) = \frac{D_{LS}\hat{\alpha_S}(\Theta)}{D_S}, \tag{3.2}$$

where D_{LS} and D_S are the lens-source and source-observe distances. (3.2) is then simplified as:

$$\alpha_S(\theta) = \frac{4GM}{c^2}\frac{D_{LS}}{D_S D_L}\frac{\theta}{|\theta|^2}, \tag{3.3}$$

where D_L is the distance between the lens and the observer.
Overall, the Einstein ring radius is:

$$\boxed{\theta_E = \left(\frac{4GM_L}{c^2}\frac{D_{LS}}{D_S D_L}\right)^{\frac{1}{2}}} \tag{3.4}$$

In addition to determining the deflection angle and the Einstein ring radius, an important parameter when observing a gravitational lens is the timescale of such a rare event to efficiently observe an exoplanet. The timescale for microlensing event, ranging from hours to days, is usually defined as [21]:

$$\boxed{t_0 = \frac{D_L \Theta_E}{v_L} = 0.214yr\left(\frac{M}{M_{Sun}}\right)^{\frac{1}{2}}\left(\frac{D_L}{10kpc}\right)^{\frac{1}{2}}\left(\frac{D_{LS}}{D_S}\right)^{\frac{1}{2}}\left(\frac{200kms^{-1}}{v_L}\right),} \tag{3.5}$$

where v_L is the lens velocity.

However, one other important parameter that is required to fully study the lensing event is the duration of the planetary perturbation $\Delta t_P \sim q^{\frac{1}{2}} t_E$ [14], where $q = \frac{M_P}{M_*}$ is the mass ratio and t_E is the timescale of the primary event. In particular, the primary event light curves must be

sampled over a time significantly smaller than Δt_p to detect and characterize planet's perturbation [14]. Besides, the probability of planet's detection is simply computed as [14]:

$$P_{det} = 0.2\ (\frac{M_P}{0.001 \times M_*})^{\frac{5}{8}} \quad (3.6)$$

Relation (3.6) is only valid for planets with projected separation (shown in equation (2.0)) $r_\perp \sim [0.6,1.6]\ d\Theta_E$, which is refered to as the 'lensing zone' [14]. The last condition for the probability detection is that $q_{min} \sim 0.1\rho_*^2$ [14].

2.1.3.3 Limitations

The detection of exoplanets via microlensing remains a useful method despite the fact it is a relativistic rare effect. For instance, in 2012, a group of astrophysicists were able to calculate the average planetary occurrence rate from microlensing observations in wide-field surveys (OGLE and MOA) in the Milky Way [22]. They monitored several stars in order to detect microlensing effects and analyzed their light curves to see short-lived anomalies [22]. They inferred this rate with a detailed statistical analysis of microlensing data and the use of the so-called cool-planet mass function that quantifies the average number of planets for a given mass range and per unit of volume.
Therefore, from the statistical analysis of the given microlensing data obtained between 2002 and 2007, it is noted that the majority of planets detected are low-mass planets and the inferred average planetary occurrence rate per Milky Way stars computed from the planetary mass function is $\Gamma_a^{M_P} = 1.6^{+0.72}_{-0.89}$ planets [22]. This average rate is consistent with the fact that every Milky Way star seems to host on average at least one planet. The microlensing survey was sensitive to the detection of planets of masses between 5 M_{Earth} and 10 M_J located on semi-major axes between 0.5 AU and 10 AU [22]. Based on the NASA exoplanet archive, only 223 exoplanets have been detected so far though the microlensing detection technique given its peculiar nature [5].
Besides, the parameters that enable the detectability, especially for habitable planets, are the mass ratio q and the projected separation s in units of $r_E = \Theta_E D_L \simeq 2.85\ AU\ (\frac{M_*}{0.5M_{Sun}})^{\frac{1}{2}}(\frac{D_S}{8kpc})^{\frac{1}{2}}[\frac{x(1-x)}{0.25}]^{\frac{1}{2}}$ (linear Einstein ring radius) , with $x = \frac{D_L}{D_S}$ [14] expressed as [14]:

$$q \sim 5 \times 10^{-5}(\frac{M_P}{M_\oplus})(\frac{M_*}{0.5M_{Sun}}) \quad (3.7)$$

$$s_{HZ} = \frac{a_{HZ,\perp}}{r_E} \sim 0.1(\frac{M}{0.5M_{Sun}})^{\frac{3}{2}}(\frac{D_S}{8kpc})^{-\frac{1}{2}}[\frac{x(1-x)}{0.25}]^{-\frac{1}{2}}, \quad (3.8)$$

where $a_{HZ} = 1AU(\frac{L_*}{L_{Sun}})^{\frac{1}{2}} \sim 1AU(\frac{M_*}{M_{Sun}})^2$ [14].

2.1.4 Wobble method

2.1.4.1 Pills on Kepler laws

The gravitational force acts between two bodies, like between a star and a planet. As a result, the star and the planet both orbit a common center of mass. This simplified configuration is known as the two-body problem and plays a pivotal role in the study of dynamic motions of two consecutive bodies such as planets, stars or satellites. Derived computations from celestial mechanics such as Kepler laws enable to determine the radial velocity. This latter is essentially defined as the velocity measured along the line-of-sight. One method called the wobble method aims at measuring the stellar radial velocity to infer the presence of a close-in planet and measure its minimum mass. All following calculations will be based on the three Kepler laws that are empirical laws based on the Solar System:

- (1) All planets follow an orbit that describes an ellipse along the path of the Sun at one point called focus. This law enables to express the distance between the planet and the Sun, known as the heliocentric distance $r_{Sun} = \frac{a(1-e^2)}{1+e\ cos\ f}$, where a is the semi-major axis of the elliptical orbit of the planet, expressed in AU and with the Sun at one focus, e the eccentricity of the orbit defined as $e = (1 - \frac{b}{a})^{\frac{1}{2}}$, with b the semi-minor axis of the planetary orbit (still in AU), and f the true anomaly, which is the angle between its instantaneous position and planet's perihelion (closest distance to the Sun).

- (2) The second law stipulates that while interacting with the Sun via a connecting line, the planet sweeps out an area A with a constant rate: $\frac{dA}{dt}$ = constant, which is a consequence of the conservation of the total orbital angular momentum: $\frac{dL}{dt}$=0, where $\vec{L} = \vec{r} \times m\vec{v}$.

- (3) The third last law links planet's orbital period P_P (in years) and its semi-major axis a_P (in AU): $P_P^2 \propto a_P^3$.

If the two-body problem is taken into account in addition to Newton laws of motion, it is possible to re-write the planetary orbital period as a function of the total mass localized on the center of mass of the two-body system, $M = m_1 + m_2$, as $\boxed{P_P^2 = \frac{4\pi^2 a_P^3}{GM}}$, where $G = 4\pi^2 AU^3\ yr^{-2}\ M_{Sun}^{-1}$ is the universal gravitational constant.

2.1.4.2 Stellar radial velocity

As mentioned in 2.1.4.1, the radial velocity detection method allows us to determine the value of the projected stellar velocity along the line-of-sight. To derive the stellar radial velocity, we first need to define the projected distance along the line-of-sight:

$$z(t) = r_*(t)\ sin(\omega + f(t))\ sin(i), \tag{3.9}$$

where $r_*(t)$ is the distance to the star, ω the argument of the periastron, which is the angle between the focus and the periastron (the closest heliocentric distance to the star), $f(t)$ is the true anomaly and i is the inclination angle, defined as the angle between the projected orbit and the true orbit.

The stellar radial velocity is then simply computed as the 1st-order time derivative of $z(t)$:

$$v_*(t) = \frac{dz(t)}{dt} = sin(i)\,[\frac{dr_*(t)}{dt} sin(\omega + f(t)) + r_*(t)]\, cos(\omega + f(t)\frac{df(t)}{dt}) \quad (4.0)$$

However, the final formula for the stellar radial velocity should be expressed in terms of known parameters that characterize the orbit of the planet around the star such as the orbital period, the stellar semi-major axis that appears to be the equal to that of the orbiting exoplanet and the planet's orbital eccentricity. Let us substitute $r*(t) = \frac{a_p(1-e^2)}{1+cos(f(t))}$ from the first Kepler law and we obtain the following value for the first-order time derivative of the stellar radial velocity as seen in (3.9):

$$\frac{dr_*(f)}{dt} = \frac{a_*(1-e^2)esin(f)}{(1+cos(f))^2}\frac{df}{dt}, \quad (4.1)$$

which can also be rewritten as:

$$\frac{dr_*(t)}{dt} = \frac{esin(f)r_*^2}{a_*(1-e^2)}\frac{df}{dt} \quad (4.2)$$

$r_*^2\frac{df}{dt}$ can be then determined from Kepler's second law:

$$r_*^2\frac{df}{dt} = \frac{2\pi ab}{P_P} \Leftrightarrow r_*^2\frac{df}{dt} = \frac{2\pi a^2\sqrt{1-e^2}}{P_P}, \quad (4.3)$$

where P_P is the planetary orbital period (in years) and b the semi-minor axis of the planet. which leads to $\frac{dr_*(t)}{dt} = \frac{2\pi aesin(f)}{b\sqrt{1-e^2}}$ from (4.2).

Eventually $\frac{df}{dt}$ can be calculated as:

$$\frac{df}{dt} = r_*^2\frac{df}{dt}\frac{1}{r} \Leftrightarrow \frac{df}{dt} = \frac{2\pi a^2\sqrt{1-e^2}\,(1+cos(f))}{P_P\,a\,(1-e^2)} \quad (4.4)$$

$$r_*(t)\frac{df(t)}{dt} = \frac{2\pi a(1+ecos(f))}{P_P\sqrt{1-e^2}} \quad (4.5)$$

Therefore, the stellar radial velocity is:

$$\boxed{v_*(t) = \frac{2\pi a_* sin(i)}{P_P\sqrt{1-e^2}}(ecos(\omega) + cos(\omega + f))}, \quad (4.6)$$

where $K = \frac{2\pi a_* sin(i)}{P_P\sqrt{1-e^2}}$ is the radial velocity semi-amplitude (in m/s) as shown in figure 1.7.

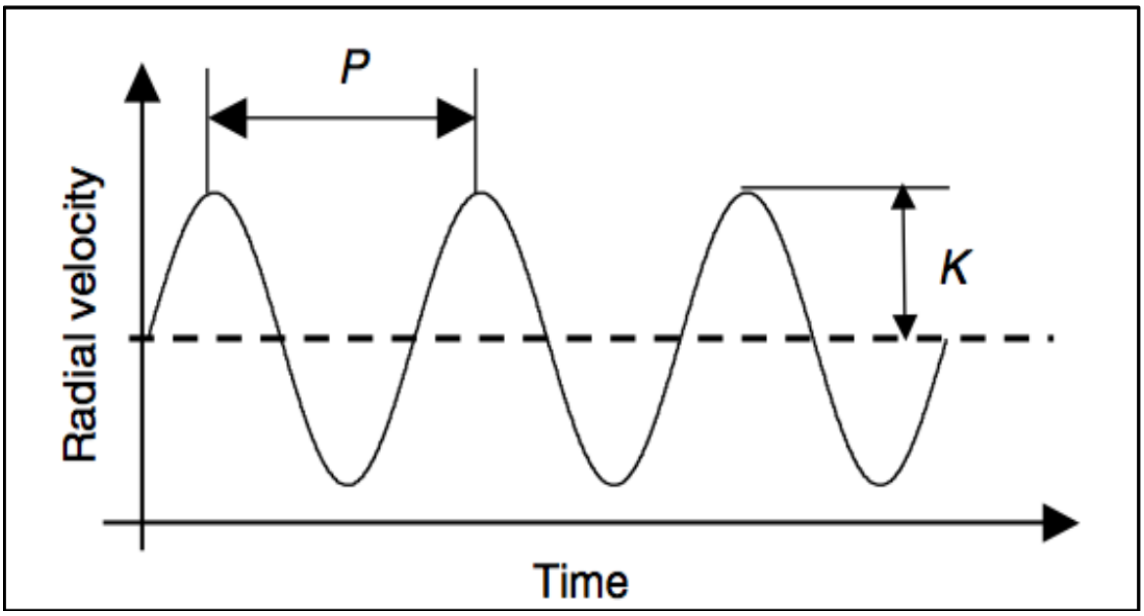

Figure 1.7: Plot showing the sinusoidal variation of radial velocity as a function of time where planet's period P and the radial velocity semi-amplitude K are represented. Image from [23].

2.1.4.3 Planetary mass and limitations

The knowledge of stellar radial velocity is of usefulness because it is possible to infer the value of the planetary mass orbiting the host star. From the radial velocity semi-amplitude expression, the stellar semi-major axis can be simply expressed as:

$$a_* sin(i) = \frac{KP\sqrt{1-e^2}}{2\pi} \tag{4.7}$$

Then, let us remind the following form of the third Kepler law:

$$\frac{P_P^2}{a^3} = \frac{G(m_P+m_*)}{4\pi^2} \tag{4.8}$$

We substitute $a = a_* + a_P$, $M = m_P + m_*$ and $a_P m_P + a_* m_* = aM$. From these substitutions one can find the value of the planet's semi-major axis:

$$a_P = a_* \frac{m_*}{m_P} \tag{4.9}$$

Which in turns enables to define the global semi-major axis set before:

$$a = a_*(1 + \frac{m_*}{m_P}) \tag{5.0}$$

By inserting equation (5.0) in (4.7), one can find:

$$\frac{a\, m_P\, m_* sin(i)}{m_P+m_*} = \frac{KP\sqrt{1-e^2}}{2\pi} \tag{5.1}$$

By expressing the latter equality in terms of the third Kepler law, the following result is found:

$$\frac{a^3(m_P m_*)^3}{(m_P+m_*)^3}(sin(i))^3 = \frac{P_P^3 K^3 (1-e^2)^{\frac{3}{2}}}{8\pi^3} \iff \frac{G P_P^2 (m_P+m_*)(m_P m_*)^3 (sin(i))^3}{(m_P+m_*)^3} = \frac{P_P^3 (1-e^2)^{\frac{3}{2}} K^3}{8\pi^3} \quad (5.2)$$

Which can be simplified as:

$$\frac{(m_P sin(i))^3 m_*^3}{(m_P+m_*)^2} = \frac{P_P (1-e^2)^{\frac{3}{2}} K^3}{2\pi G} \quad (5.3)$$

Therefore, the planetary mass can be calculated as:

$$\boxed{m_P sin(i) \simeq K(\frac{P}{2\pi G})^{\frac{1}{3}} m_*^{\frac{3}{2}} \sqrt{1-e^2}} \quad (5.4)$$

From equation (5.4), it is relevant to demonstrate that the most suitable exoplanetary system candidates to be detected via the radial velocity detection method are certainly short-period and massive planets around small stars so that the planetary signal can be easily disentangled from the stellar signal. In other words, massive and close-in exoplanets around low-mass stars induce much more significant stellar radial velocity oscillations or wobbles. Since the wobble detection method mainly relies on the observation of the host star, several requirements are needed such as high-spectral resolution, high signal-to-noise ratio boosted by using multiple spectral lines and the stability of the star and the spectrograph for a significant timescale, typically for several years. Besides, the stellar activity can mimic the planetary signal such as seen with the production of dark spots causing radial velocity oscillations larger than 10-100 m s^{-1}, especially around young stars [24]. The effect of stellar activity affecting the measurements of radial velocities is known as the jitter parameter.
For instance, 51 Peg b was detected though the radial velocity method and is thought to induce a stellar radial velocity method with the ELODIE spectrograph with an accuracy of 13 m s^{-1}. From an analysis point of view, the radial velocity is computed using a cross-correlation function that produces a mean of all the stellar spectral lines. The typical fit of the spectral lines obtained is a Gaussian function and the position of this specific function gives the value of the radial velocity, as emphasized in the cross-correlation function plotted in figure 1.8. The position of the Gaussian function is a key parameter to measure the Doppler shift in the stellar spectrum.

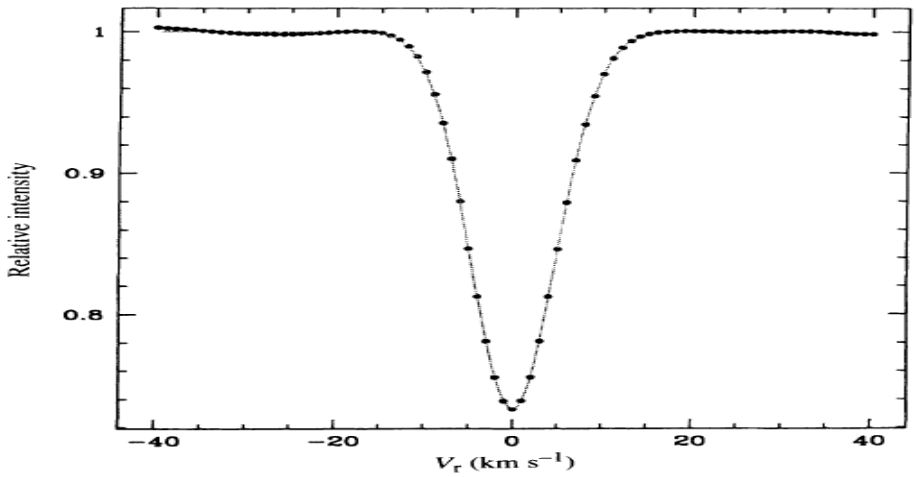

Figure 1.8: Typical cross-correlation function used to measure the radial velocity induced by 51 Peg b. A typical Gaussian function is fitted (solid line) in order to measure the Doppler shift. 5000 spectral lines are concentrated in one mean spectrum. Plot from [4].

Regarding the detection of habitable planets, they are much easier to detect close to low-mass stars. For instance, an Earth-like planet located in the habitable zone up to 0.1 AU would induce a radial velocity signal estimated to 0.9 m s^{-1} [24]. Based on the NASA exoplanet statistics, 1093 extrasolar planets have been detected through the application of the radial velocity method [5].

2.1.5 Transits

2.1.5.1 Description of the transit method

Another method that is genuinely complementary to the radial velocity method for detecting exoplanets is the transit method. It generally occurs when a planet is passing in front of a star. However, transits differ from the microlensing configuration where there is the magnification effect provided by the planet, aligned with the background and foreground light sources. On the other hand, a transit is essentially different because the planet is occulting a given fraction of the stellar surface, which affects the stellar brightness. This modification of the stellar brightness is well demonstrated in the so-called stellar light curve, as shown in figure 1.9.
Indeed, the stellar flux varies with respect to time due to the passing of the planet. It is relevant to notice the depth of the transit, that logically increases with the size of the planet for a given stellar host of radius R_*. The transit depth is the observational evidence of the presence of an exoplanet orbiting the host star. As shown in figure 1.9, the typical transit duration is counted in hours, which is helpful to reduce the monitoring time.

Furthermore, one should point out that when the planet passes behind the star, it is referred to as an occultation, as represented in figure 2.0. Therefore, the orbital plane needs to be nearly aligned with the observer and the planet passing in front of or behind the star and remains a primary condition for the observation of a transit. The last condition is the probability of transit p_{tra}, defined as the ratio between the size of the star R_* and the planet's orbital distance a_P:

$$p_{tra} = \frac{R_*}{a_P} \quad \text{if} \quad a_P|cos(i)| < R_* \tag{5.5}$$

From (5.5), we assume that the space orbit distribution is uniform and integrate the probability of having orbits over the solid angle where a transit is observed by normalizing over half of the sphere. The above expression can also be rewritten by multiplying by the Earth transit probability $p_{tra,\oplus} = 0.005$:

$$p_{tra} = 0.005(\frac{R_*}{R_{Sun}})(\frac{1AU}{a_P}) \tag{5.6}$$

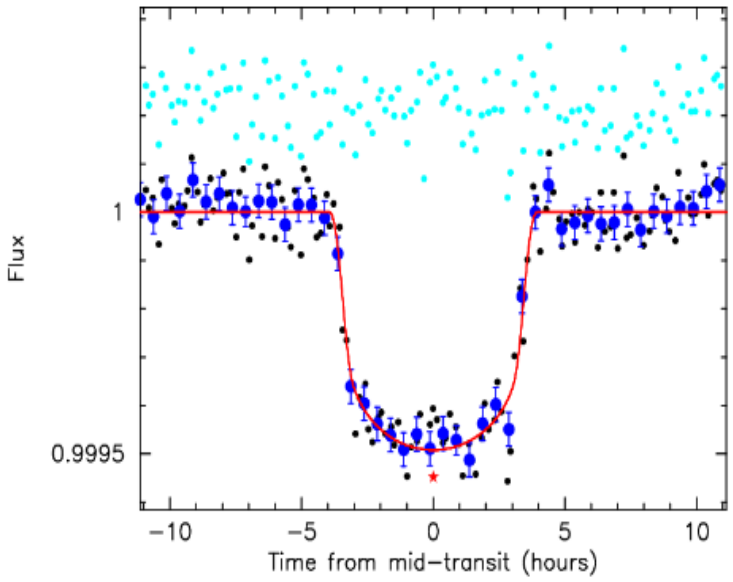

Figure 1.9: Light curve of Kepler-22b. The model considered is fitted with the red curve. The dark dots represent individual observations. Dark blue dots show 30-minute binned data while cyan points are residuals from fitting. Red asterisk represents the mid-transit times based on the model fit with eccentricity value allowed to float. Plot from [25].

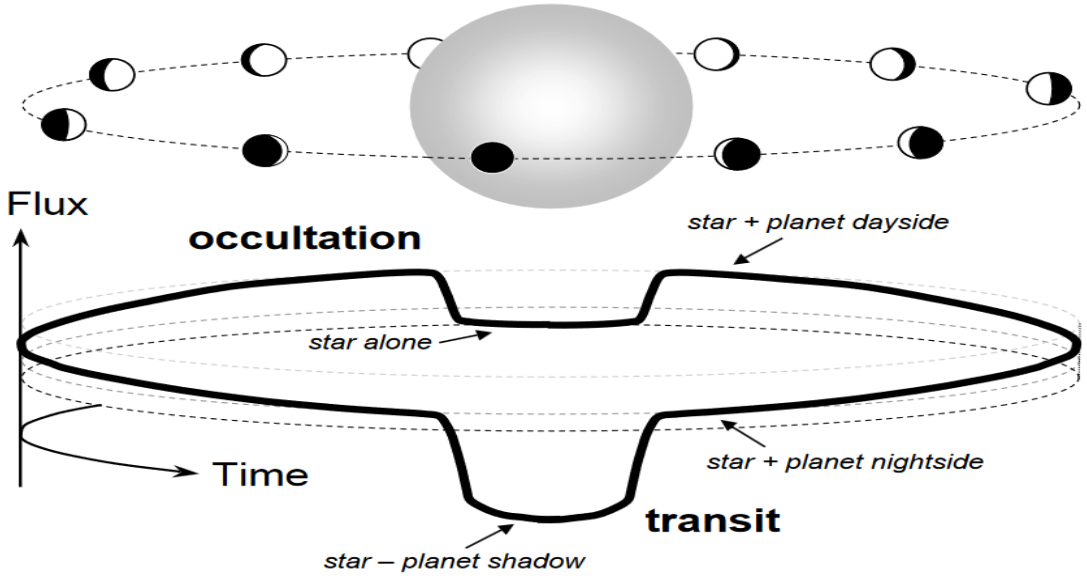

Figure 2.0: Schematic of a transit and an occultation. When the planet is transiting the star a combined dropped stellar and planetary flux is observed whereas during an occultation only the stellar flux is seen but still decreasing. The combined flux only increases when the planet dayside comes into view. Plot from [26].

2.1.5.2 Physical parameters derived from transits

Concretely, several physical quantities can be derived from the observation of a transit such as the depth of the transit, the transit duration, the stellar density or the impact parameter.

The depth transit δ or the fraction of stellar surface occulted by the planet assuming a full transit, is simply computed as the ratio between planet's area A_P and the stellar area A_*:

$$\boxed{\delta = \frac{A_P}{A_*} = (\frac{R_P}{R_*})^2,} \quad (5.7)$$

which can also be expressed in terms of Jupiter radius given its important size R_J:

$$\boxed{\delta = 0.01\ (\frac{R_P}{R_J})^2\ (\frac{R_*}{R_{Sun}})^{-2}} \quad (5.8)$$

Then, one important parameter to consider is the transit duration. It can be inferred from geometrical considerations from figure 2.1 below.

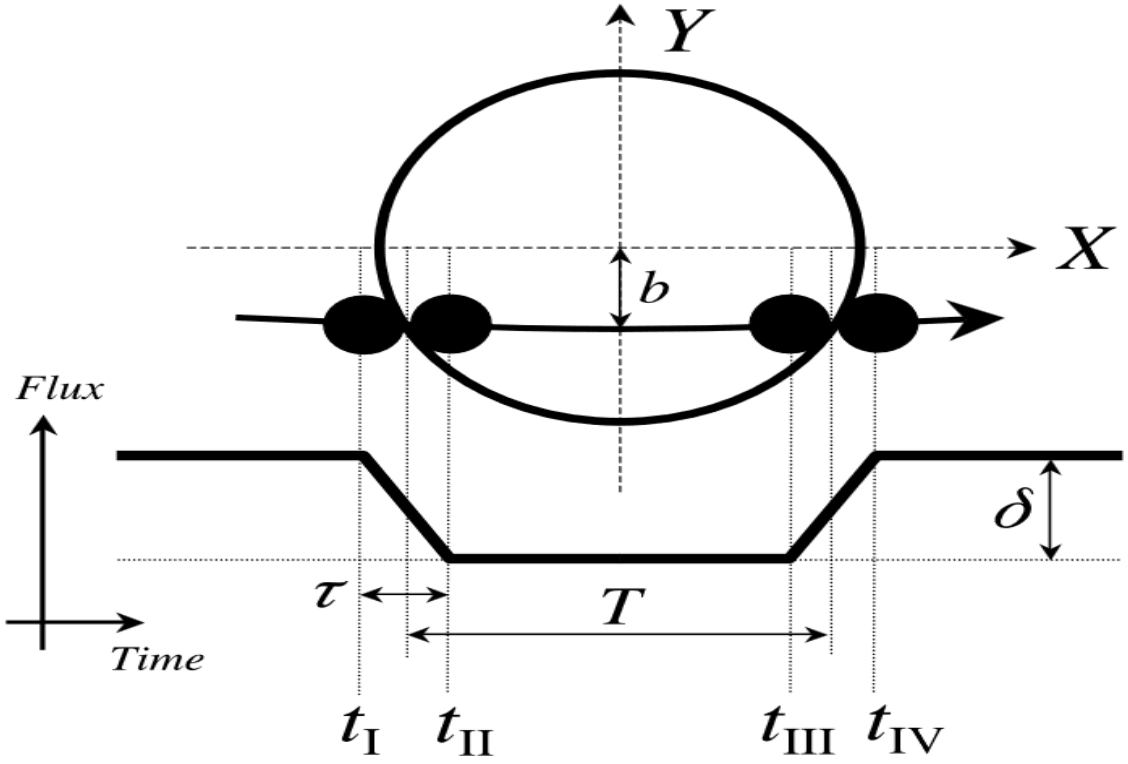

Figure 2.1: Illustration of a transit in Cartesian coordinates system (X,Y,Z) divided in four contact points at specific times. Plot from [26].

From figure 2.1, T is the time during which the planet begins and terminates to hide the stellar disk, $\tau_{in} = t_{II} - t_I$ is the ingress time occurring between phases I and II. A similar conceptual time is then set between phases III and IV and is called the egress time such that $\tau_{egr} = t_{IV} - t_{III}$. The study of transits also requires setting the ratio between the planetary size and the stellar size $F = \frac{R_P}{R_*}$. Besides, the following assumptions must be applied:

$$b < 1 - k \text{ and } e \to 0\ , \quad (5.9)$$

where $b \simeq 1 - \sqrt{F}\frac{T}{\tau}$ is the impact parameter. In addition, $\tau \approx \frac{T_0 F}{\sqrt{1-b^2}}$.

The time T is defined such that $T \approx T_0\sqrt{1-b^2}$, where $T_0 = \frac{R_* P_P}{a_P \pi}$ is the transit duration that can be finally expressed as:

$$T_0 \simeq 13\ hr\ (\frac{P_P}{1yr})^{\frac{1}{3}}\ (\frac{\rho_*}{\rho_{Sun}})^{-\frac{1}{3}} \quad (6.0)$$

2.1.5.3 Transit spectroscopy and limitations

One of the main advantages of detecting extrasolar planets via the transit observation method remains the study of its atmosphere via spectroscopic analysis. In fact, when the planet transits the host star, the atmosphere is efficiently detected thanks to the impact of stellar activity, generating many spectral absorption lines that can reveal the planetary atmospheric composition. Indeed, the transit spectroscopy technique enables to measure the transit depth, set in equations (5.7) and (5.8), as a function of the wavelength of the incident stellar radiation, as shown in figure 2.2. The deeper the transit the stronger the absorption lines. This method is a very efficient tool to study the chemical, dynamical and radiative properties of upper planetary atmosphere.

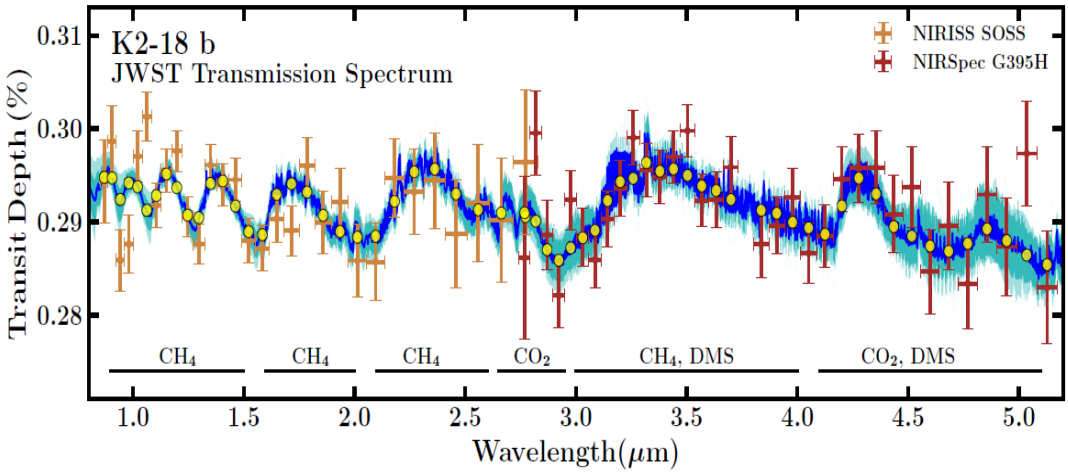

Figure 2.2: Retrieved spectral fit of the transmission spectrum of K2-18b by the JWST with its two spectrographs NIRISS SOSS and NIRSpec G395H using a model with no clouds and hazes. The data in orange shows NIRISS spectrum. Different molecules signatures are displayed for different NIR wavelength intervals. Plot from [27].

In addition, observing efficiently the atmosphere depends on its sustainability. During planet's history, the atmospheric evolution is strongly affected by the amount of incoming stellar radiation, potentially leading to atmospheric escape. Several types of atmospheric escapes can be described such as non-thermal, thermal Jeans escape and hydrodynamical escape. A non-thermal escape can be ruled out in the case of exoplanets since photodissociation is not strong enough to contribute to a global atmospheric escape. Then, Jeans escape likely happens when atmospheric particles velocities $v_{particle}$ are much higher than the escape velocity v_{esc}, which is the threshould velocity value for escaping the planetary surface gravity. On Earth, this velocity is equal to 11.2 km s^{-1}. The escape velocity is simply computed by assuming a conservation of particle's total energy: their kinetic energy is equivalent to their potential energy:

$$E_{kin} = E_{pot} \Leftrightarrow \frac{1}{2} m_{particle} v_{esc}^2 = \frac{G M_P m_{particle}}{r} \quad (6.1)$$

$$\Leftrightarrow \quad v_{esc} = \sqrt{\frac{2GM_P}{R_P + z}}, \quad (6.2)$$

where z is the altitude of the exobase, which is 500 kilometers in the case of Earth's atmosphere.

Besides, let us assume that the particles follow the Maxwellian velocity distribution, expressed from statistical mechanics as:

$$f(v) = (\frac{m}{2\pi kT})^{\frac{3}{2}} 4\pi v^2 \, exp(-\frac{mv^2}{2kT}), \tag{6.3}$$

with T the temperature of the exobase, i.e the boundary between the thermosphere and the exosphere.

Then, it is relevant to derive the particle's velocity, which corresponds to the most probable value of the Maxwellian distribution, representing the average velocity:

$$\boxed{v_0 = \sqrt{\frac{2kT}{m_{particle}}}} \tag{6.4}$$

By applying a 'rule of thumb', one may notice that the probability of particles escape is much more significant if the particles are moving at a mean velocity such that $v_0 > \frac{1}{6} v_{esc}$, as shown on figure 2.3. Therefore, the Jeans escape depends on the mass of the particles, the planetary mass and the temperature of the exobase. Overall, the exobase is part of the atmosphere boundary where particles change from a collisional behavior to a ballistic behavior.

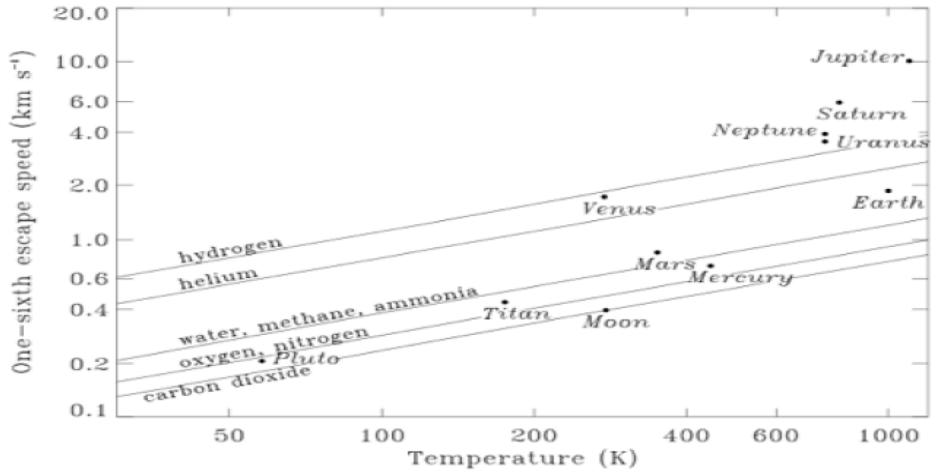

Figure 2.3: Graph showing the relationship between the escape velocity and the atmospheric planetary temperature for several gases (plotting lines) and planets (black dots) of the solar system in the case of the Jeans escape. Plot from [28].

Besides, the examination of the atmospheric properties through transmission spectroscopy also requires the knowledge of the extent of the atmosphere to characterize it as a thin or a thick atmosphere. This can be typically done by calculating the atmospheric scale height parameter, which depends on the atmospheric temperature T, the mean molecular weight μ of the main compositional gas and planet's surface gravity g:

$$\boxed{H = \frac{k_B T}{\mu g}} \tag{6.5}$$

The atmospheric depth can be inferred from the previous equation and is conventionally expressed in parts per million (ppm):

$$\boxed{\delta_{atmos} = \frac{2HR_P}{R_*^2}} \tag{6.6}$$

The dominant process for the global atmospheric escape for many exoplanets, especially hot Jupiters, is thought to be the hydrodynamic escape or blowoff erosion. Particularly highly irradiated exoplanets, especially by the impact of X-rays and UV (XUV) radiation, leading to hydrodynamic escape and decreasing the planetary mass over time. This mass loss rate is quantified as [29]:

$$\boxed{\frac{dM}{dt} = \epsilon \frac{R_P}{GM_P} \pi \, F_{X+UV} \, R_{X+UV}^2,} \tag{6.7}$$

where ϵ is the net X+UV heating efficiency that is the ratio between the net heating rate (i.e the subtraction of stellar-energy absorption by the cooling) and the stellar energy absorption rate, F_{X+UV} is the incident X+UV flux and R_{X+UV} is the effective radius for X+UV absorption.

Overall, the transit is biased towards the detection of massive and close-in planets because they produce stronger transit depths in light curves. Additionally, the effect of high-mass and close-in exoplanets is gravitationally more important on low-mass stars, which tends to facilitate the detection process. Therefore, according to the NASA Exoplanet Archive [5], 4274 exoplanets have been detected via the transit method and remains the most used method to detect extrasolar worlds.

2.2 Exoplanets populations

2.2.1 Neptune-like planets and sub-Neptunes

2.2.1.1 Internal structures

Neptune-like planets are planets having a similar bulk and atmospheric composition to Uranus and Neptune. It is thought that their interiors are decomposed into a mixture of different chemical elements. Regarding their bulk density, Uranus and Neptune possess respective masses of $M_U = 14.5\ M_\oplus$ and $M_N = 17 M_\oplus$ and sizes of $R_U \approx R_N \approx 4R_\oplus$ [30]. More accurate values for their radii are $R_U = 3.98\ R_\oplus$ and $R_N = 3.86\ R_\oplus$ [31], respectively. Other physical parameters of Uranus and Neptune are reported in figure 2.4.
Regarding sub-Neptunes, they represent a misleading planetary type because they are often assimilated to super-Earths that we will study in detail in section 2.2.3 and in chapter 3. In exoplanetary science, sub-Neptunes or mini-Neptunes are planets characterized by sizes between that of the Earth and Neptune such that $1R_\oplus \leq R_P \leq 4R_\oplus$ [32] and masses comprised in the range such that $1M_\oplus \leq M_P \leq 10M_\oplus$ [27]. No planets with such radii and masses are found in the Solar System, thus they represent a relatively unique planetary type. Nevertheless, they are characterized by hydrogen and helium-dominated atmospheres like gas giants. Another definition of sub-Neptunes is extrasolar planets having a radius larger than $1.6 - 1.7R_\oplus$, which enables to retain hydrogen envelopes [33]. On the other hand, planets with radii lower than the previous radii range are referred to as super-Earths and are thought to be predominantly rocky. The $1.7R_\oplus$ acts as a gap or valley that is sculpted by smallest sub-Neptunes subject to

evaporative loss of hydrogen envelope that could be either due to photoevaporation or core-powered mass loss [33]. Observations seem to favor photoevaporation [33], the stellar mass dependence might be the answer to this problem. Concretely, photoevaporation modelling predicts that the amount of incident stellar flux might decrease with decreasing stellar mass as observed while core-powered mass loss is independent of the stellar mass.

parameter	Uranus	Neptune
semi-major axis (AU)	19.201	30.047
mass (10^{24} kg)	86.8127 ± 0.0040^{a}	102.4126 ± 0.0048^{b}
mean radius* (km)	25362 ± 7^{c}	24622 ± 19^{c}
mean density (g cm^{-3})	1.270 ± 0.001^{d}	1.638 ± 0.004^{d}
R_{ref} (km)	$25\,559^{a}$	$25\,225^{b}$
J_2 ($\times 10^6$)	3510.68 ± 0.70^{a}	3408.43 ± 4.50^{b}
J_4 ($\times 10^6$)	-34.17 ± 1.30^{a}	-33.40 ± 2.90^{b}
rotation period* (Voyager)	$17.24\ h^{e}$	$16.11\ h^{f}$
1-bar temperature (K)	76 ± 2^{g}	72 ± 2^{h}
effective temperature (K)	59.1 ± 0.3^{i}	59.3 ± 0.8^{j}
intrinsic flux (J s^{-1} m^{-2})	0.042 ± 0.045^{i}	0.433 ± 0.046^{j}
bond albedo *A*	0.30 ± 0.049^{h}	0.29 ± 0.067^{h}
axis tilt	97.77	28.32

Figure 2.4: Table giving an overview of the different physical properties of Uranus and Neptune. Quantitative data from [31].

Despite the detailed knowledge of the physical parameters listed in table 2.4 of Uranus and Neptune, the investigation of their internal structure remains an ongoing research topic. Most of data available on the two ice giants is based on the Voyager 2 space mission data, limiting the knowledge on their interiors. Besides, understanding their interiors is the key reasoning to constrain their formation and evolution processes. In-situ space probes and orbiters are indubitably necessary to accurately describe the internal structure, like in the case of the Galileo and Juno probes with Jupiter and its moons.
Concretely, the full theoretical modeling of planetary interiors requires the application of a set of fundamental equations derived from hydrodynamics assuming hydrostatic, thermodynamic, mass and energy conservations:

- Hydrostatic equilibrium equation: $\frac{\partial P}{\partial r} = -\rho g$ (6.8)
- Thermodynamic conservation: $\frac{\partial T}{\partial r} = \frac{\partial P}{\partial r}\frac{T_P}{P}\nabla_T$ (6.9)
- Mass continuity equation: $\frac{\partial m}{\partial r} = 4\pi R_P^2 \rho$ (7.0)
- Energy source equation: $\frac{\partial L_P}{\partial r} = 4\pi R_P^2 \rho(\frac{d\epsilon}{dt} - T_P\frac{\partial S}{\partial t})$ (7.1)

In the above equations, r is the planetary radius as measured from the center, P the pressure, ρ the density, $g = -\frac{Gm}{r^2}$ is the planetary surface gravity, m the planet mass in the interior, T the total temperature, L_P the planetary internal luminosity, S the entropy, T_P the planet temperature, ϵ the heating efficiency, R_P the planetary radius, and ∇_T the temperature gradient depending on

the energy process. A hypothetical view of Uranus and Neptune internal structures is given in figure 2.5. Both planets have a gaseous envelope predominantly composed of hydrogen, helium and ices elements given the extremely low surface temperature of nearly 60 K as shown in figure 2.4. The following deeper layer is an icy shell underneath the surface, whose sizes differ drastically between the two planets. Indeed, Uranus has a much thicker icy shell than Neptune. Moreover, this might be a multiple-structured ice layer containing rocks and gases such as hydrogen and helium. Finally, the planetary cores may contain rocks and ices.

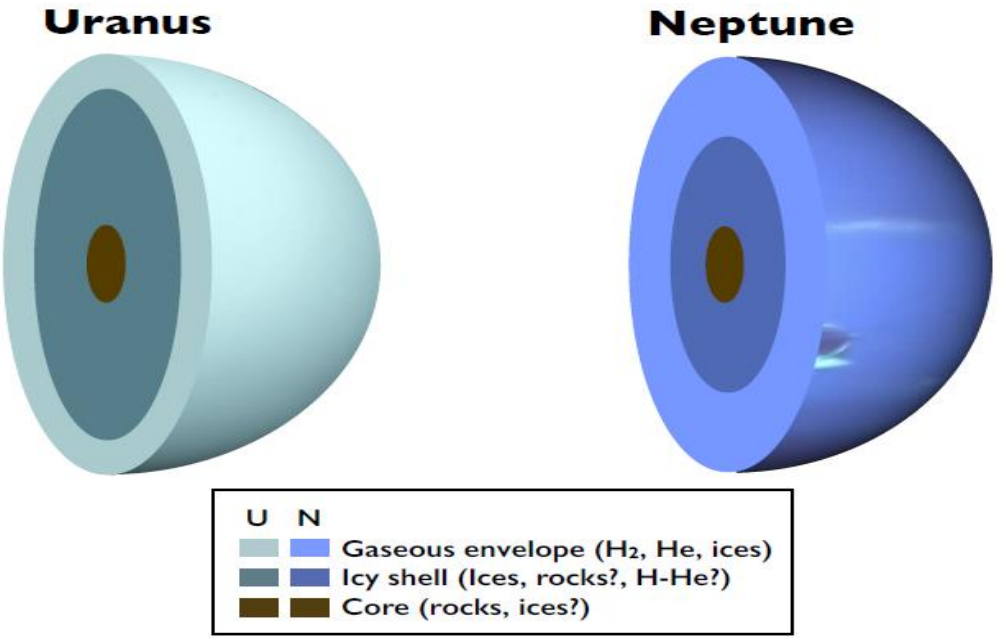

Figure 2.5: Schematic view of the internal structures of Uranus and Neptune. Image from [34].

Interestingly, even though Uranus and Neptune present a cold surface, their interior is subject to an important heating mechanism. This deep heat transport, as in most terrestrial planets, represents a convection motion which generates the intrinsic planetary magnetic field. Despite many similarities between Uranus and Neptune, the intrinsic heat fluxes on the two ice giants are not in the same order of magnitude. The Uranian heat flux is one order of magnitude lower than that of Neptune's [35]: indeed, models predict either a low initial formation temperature or a convective-inhibited mechanism that prevents heat from escaping efficiently from the interior [35]. On the other hand, Neptune would be less or not affected by such mechanism. The Neptunian heat flux would be more probably affected by a fully adiabatic interior condition [35], which raises a global paradox because of the similar magnetic fields generated by the ice giants [35]. Thus, further in-situ and orbital missions are needed to explain the interior composition and validate the origin of the heating mechanism for both ice giants.

Similarly, sub-Neptunes interiors might be a mixture of rocks and ices, where some of them might be water-rich worlds. As in the case of Neptune-like planets, one way to model the internal structure is to apply the *completo21* interior structure modeling code. This model is based on the assumption of a 1D spherically symmetric planetary interior's structure equations [36]. The *completo21* model yields the pressure, enclosed mass, temperature and intrinsic luminosity as a function of the distance to the core. Based on the assumptions of this model, it is hypothesized that sub-Neptunes are structured in three main layers: an iron core, a silicate mantle and a gaseous/fluid envelope, where a 2:1 silicate: iron ratio is assumed in all three layers [32].

The iron core and the silicate mantle are described by a modified polytropic equation of state (PEOS) [37]:

$$\boxed{P = K_p \rho^{1+\frac{1}{m}} \text{ or } \rho = \left(\frac{P}{K_p}\right)^{\frac{m}{m+1}}} \quad (7.2)$$

Where $K_p \approx \left(\frac{\rho_0}{c}\right)^{\frac{1}{n}}$ is the bulk modulus and a constant, m the polytropic index. n is an exponent basically depending on the material stuck into the core and the mantle, using the parameters of perovskite for the silicates [37] such that n=0.541. ρ_0 incorporates the approximate incompressibility of solids and liquids at low pressures. Overall, the previous equation of state is only valid for pressures lower than 16 GPa [37].

Then, the completo21 model assumes that the gaseous/fluid envelope is made of a homogeneous mixture of H/He and H_2O that are respectively described by the following equations of state [38, 39]:

- CMS equation of state for H/He: $\boxed{\frac{1}{\rho(T,P)} = \frac{1-Y}{\rho_H(T,P)} + \frac{Y}{\rho_{He}(T,P)}}$, (7.3)
  where $Y = \frac{M_{He}}{M_H + M_{He}}$ denotes the helium mass fraction, ρ_H the hydrogen density and ρ_{He} the helium density. This equation of state is carried out in the context of the additive volume law. This law is based on the additivity of extensive variables (volume, energy, entropy…) at constant intensive variables (P, T). This method is formally valid for non-interacting, ideal mixtures and excellent in the case of fully ionized systems [38], it is thus not reliable for interacting systems or partially ionized systems, e.g between hydrogen and helium species.

- AQUA equation of state for H20: there are two cases for water, either if the equation gives a functional form for the Gibbs free energy potential or for the Helmholtz free energy potential, discussed in the next paragraph.

Let us remind the Gibbs and Helmholtz free energy thermodynamic potentials, respectively formulated as:

- $g(P,T) = H - T\,S = u(P,T) + \frac{P}{\rho(P,T)} - T\,s(P,T)$, (7.4)
- $F(P,T) = U - T\,S = u(P,T) - T\,s(P,T)$, (7.5)

  where H is the enthalpy, S the total entropy, u the specific internal energy such that $u = \frac{U}{M}$, s the specific entropy such that $s = \frac{S}{M}$, U the total internal energy, T the temperature, ρ the density and P the pressure.

Thus, the Gibbs and Helmholtz potential are conventionally used to derive fundamental thermodynamic quantities such as pressure, temperature or entropy by calculating their first and second derivatives.

In case the EOS is expressed in terms of Gibbs potential, one may obtain [39]:

$$\boxed{\rho(P,T) = V(P,T)^{-1} = \left(\frac{\partial g(P,T)}{\partial P}\right)^{-1}} \quad (7.6)$$

On the other hand, if the EOS is formulated as Helmholtz free energy potential, one may find which density corresponds to a given (P, T) tuple, using a bisection method and obtain the following EOS [39]:

$$\boxed{P(\rho,T) = \rho^2(\frac{\partial f(\rho,T)}{\partial \rho})} \quad (7.7)$$

, equations (7.6) and (7.7) are non-ideal equations to model high densities and high pressures within the interior. Overall, our understanding of the interior of sup-Neptune type planets is very limited due to the inherent degeneracy in their interior structure composition. Further accurate characterization of their interiors is needed to constrain the formation and evolutionary pathways of such planets to postulate if they formed in the inner part of the planetary system or beyond the snowline. Indeed, forming beyond the snowline can lead to the formation of water, which is relevant in assessing the planetary habitability among other parameters that will be detailed in the next chapter. Then, it is possible to infer the composition of the atmospheres of Neptune and sub-Neptune exoplanets via transmission spectroscopy, especially with the powerful JWST.

2.2.1.2 Atmospheric characterization

Understanding the atmospheric dynamics of ice giants like Uranus and Neptune is one methodology to explain their atmospheric composition affected by a variety of chemical processes and the formation of Neptune-like planets. As mentioned in the introduction, ice giants have cold hydrogen and helium-dominated atmospheres. As opposed to other gas giants like Jupiter and Saturn, ice giants appear to contain more chemical elements such as methane that condensate into the upper atmospheres, leading to the formation of clouds and moist convective storms [40]. Some recent observations postulate the formation of deeper clouds of hydrogen sulfide (H_2S) at pressures of a few bars and thermochemical models suggest there could be even deeper clouds of ammonia hydrosulfide (NH_4SH) and water at pressures from tens to hundreds of bars, thus forming deep weather layers [40]. There is some evidence of moist convective storms on Uranus and Neptune. Moist convective storms are defined as clouds formed by vertical ascending motions powered by buoyance differences and vertically transporting heat [40]. All this evidence is found thanks to the observations of clouds activity and the computed abundances of methane above the tropopause in the case of Neptune [40]. Figures 2.6 and 2.7 are images representing several candidate planetary features that would likely be associated with moist convective storms for Uranus and Neptune respectively.

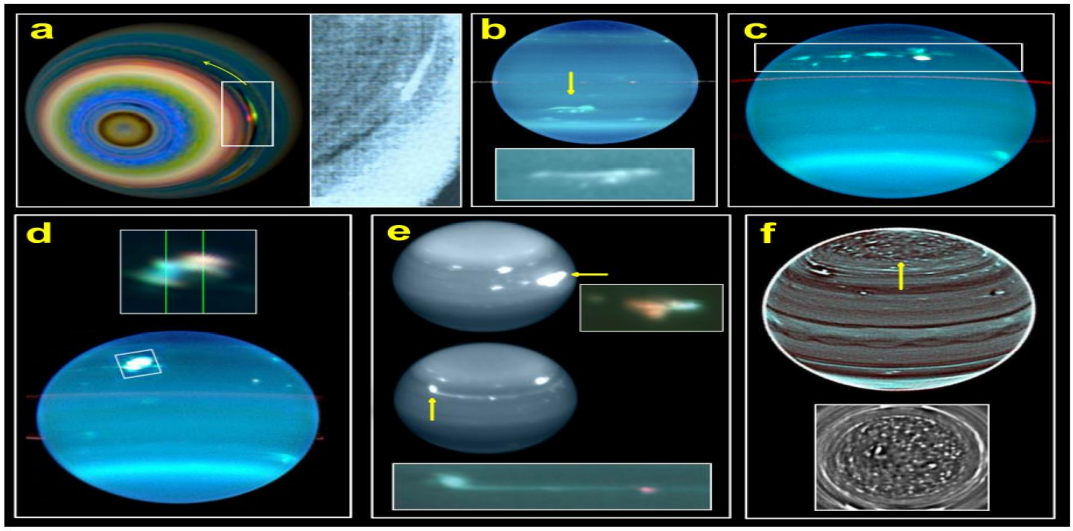

Figure 2.6: Candidate features for moist convection on Uranus: (a) A plume-like feature observed by Voyager 2 in 1986 southern hemisphere. The yellow arrow represents the direction of rotation; (b) The Berg cloud feature observed in 2007 (arrow); (c) The multiple northern bands with several spots observed in 2004; (d) Bright spot observed in 2005; (e) The brightest spot observed in 2014 with an elongated cloud system; (f) Cloud cluster in the North Pole observed in 2012. Panels (a-d) show color composite images based in optical to near infrared wavelengths below $1\mu m$ with bright features in wide methane absorption bands. Panel (e) is images from band H ($1.6\mu m$) with insets using a combination of near infrared images in bands H (blue), a CH_4S filter ($1.53-1.66\mu m$ in green) and K' ($2.2\mu m$ in red) being the latter the most sensitive to high clouds. Panel (f) shows observations in band H. Images from [40].

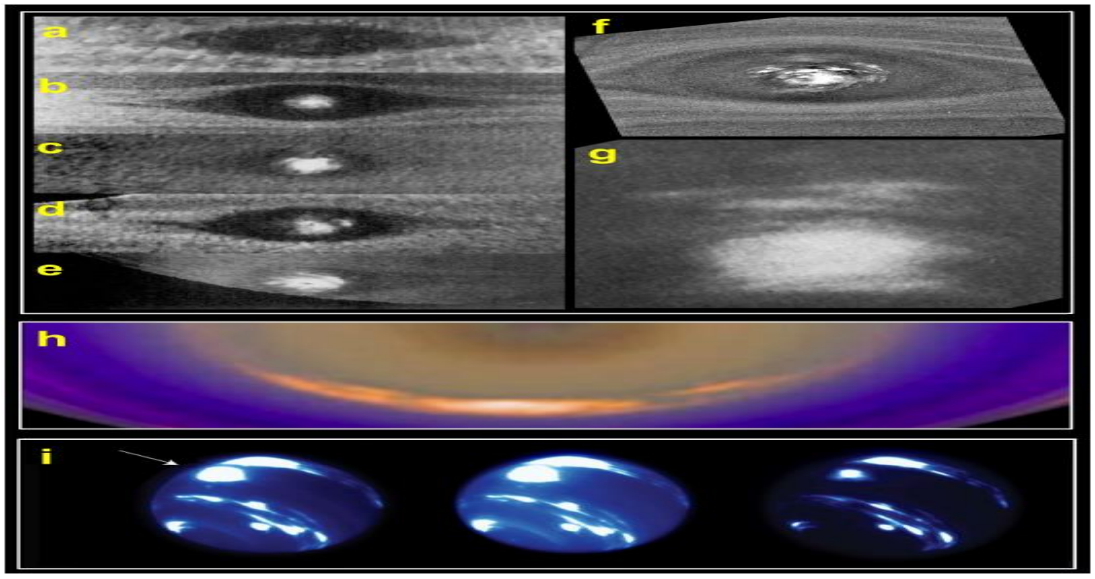

Figure 2.7: Candidate features for moist convection on Neptune: (a-e) Variable activity at the center of the anticyclone DS2 in 1989 from Voyager 2; (f) Details at the center of the DS2; (g) The "scooter" imaged by Voyager 2; (h) Details of the SPF taken by Voyager 2; (i) Bright equatorial cloud complex in 2017 at near infrared wavelengths. Panels (a-g) in Voyager 2 clear filters (a-b), orange (c), violet (d), green (e), blue (f), and green (g). Panel (h) is just a false color composite with red, green and blue from observations in yellow, blue and ultraviolet light respectively. Panel (i) shows images on moderate to strong absorption methane wavelengths in band H ($1.63\mu m$), CH_4 ($1.59\mu m$) and K' ($2.12\mu m$). Images from [40].

Overall, chemistry controls the atmospheric composition of Uranus and Neptune, especially by generating clouds, hazes, thermal structure, atmospheric dynamics and circulation. The atmospheres of the ice giants are broadly similar to that of the Earth in terms of layers space distribution. It can be divided into three major parts: the troposphere, stratosphere and thermosphere. First, the troposphere is the regions where the convection process occurs and where the temperature decreases with the altitude. Then, the stratosphere is the intermediate layer of the atmosphere where radiative processes dominate, which leads to an increase of the temperature with increasing altitude. Ultimately, the thermosphere is the uppermost region where the increase of the temperature is sharper, and the heat conduction is propagating downward from the highly irradiated exosphere. Therefore, the chemical composition of the three layers obviously differs because of the temperature and pressure differences. The detailed composition of each atmospheric part as well as the temperature-profile are represented in figure 2.8.

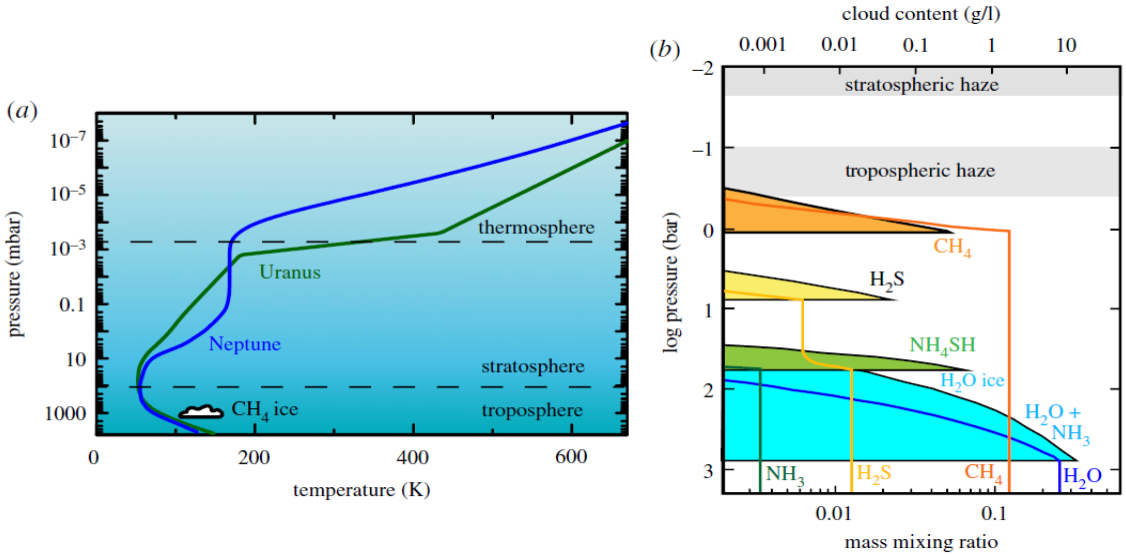

Figure 2.8: (a): Global-average temperature-pressure profile of Uranian and Neptunian atmospheres with major regions of the atmosphere labelled; (b): Thermochemical equilibrium prediction model of the upper-tropospheric cloud structure on Uranus. The results for Neptune are consistently similar. The predicted mass mixing ratios of condensable gases are shown as colored solid lines, and the maximum cloud density as solid black lines with color-shaded regions. Plots from [41].

From figure 2.8, the troposphere seems to contain a variety of molecules ranging from methane (CH_4) at the upper-tropospheric part near the tropospheric haze region to the presence of liquid water at several hundreds of bars. Starting from the bottom of the atmosphere, a solution cloud made of ammonia and water is formed between 100 and 1000 bars until there is a phase transition from this solution cloud to a water-ice cloud near the top of this latter. Then, an ammonium hydrosulfide (NH_4SH) cloud is likely to be formed by the combination of ammonia (NH_3) and hydrogen sulfide (H_2S) at pressures between 10 and 100 bars. The rest of (H_2S) forms an ice cloud at pressures between 1 and 10 bar and methane condensates into an ice cloud at 1 bar-level near the tropospheric haze boundary. These are optically thin hazes resulting from disequilibrium process and photochemical products residing above the methane cloud [41]. From a spectroscopic point of view, only hydrogen, helium, methane and hydrogen sulfide can be detected directly while other elements are thought to be the products of disequilibrium

chemical processes [41]. Figures 2.9 and 3.0 provide an estimate of the amount of the different chemical elements found in the troposphere and the stratosphere, respectively. Overall, it is thought that thermochemical equilibrium is expected to control the composition in the deeper and hotter regions of the atmosphere on both planets while disequilibrium chemical processes such as transport-induced quenching and photochemistry alter the composition in the upper atmospheric regions of Uranus and Neptune [41].

species	Uranus	Neptune
He	15.2%	14.9%
CH_4	1.4–4%	2–5%
NH_3	30–90 ppm	40–200 ppm
H_2O	<5%	27%
PH_3	<2 ppm	<1.1 ppb at 0.7 bar
H_2S	0.4–0.8 ppm	1–3 ppm
	>10–25 ppm	700 ppm

Figure 2.9: Tropospheric composition by volume of Uranus and Neptune (above the water solution-cloud) from recent references. Table from [41].

species	Uranus	Neptune
CH_4	16 ppm at 50 mbar	0.115% at 5 mbar
C_2H_2	0.25 ppm at 0.2 mbar	0.033 ppm at 0.5 mbar
C_2H_4	$<2 \times 10^{-14}$ at 10 mbar	0.8 ppb at 0.2 mbar
C_2H_6	0.13 ppm at 0.2 mbar	0.85 ppm at 0.3 mbar
C_3H_4	0.36 ppb at 0.4 mbar	0.12 ppb at 0.1 mbar
C_4H_2	0.13 ppb at 0.4 mbar	0.003 ppb at 0.1 mbar
CO_2	0.08 ppb at 0.14 mbar	0.78 ppm at 0.1 mbar
CO	6 ppb at 0.5 mbar	1.1 ppm at 0.1 mbar
H_2O	3.8 ppb at 0.03 mbar	2.5 ppm at 0.16 mbar
D/H	4.4×10^{-5}	4.1×10^{-5}

Figure 3.0: Stratospheric composition by volume of Uranus and Neptune from recent references. Table from [41].

On the other hand, atmospheres belonging to the sub-Neptunian regime appear to be more chemically diverse than their gas giant counterparts. For instance, the Solar System represents an interesting mix of atmospheric types that are the primary (gas giants) and secondary

atmospheres (terrestrial planets). Primary atmospheres are the direct imprints of the planetary formation history while secondary atmospheres have an evolving chemistry due to the interaction between the atmosphere and the interior such as transport of chemical elements. Nevertheless, sub-Neptune planets, given their continuum nature between gas/ice giants and rocky exoplanets, seem to possess hybrid atmospheres, which are classified between primary and secondary atmospheres [32]. Theory predicts that low-mass exoplanets have a more significant chemical diversity that could be due to an underabundance of hydrogen and helium, giving high metallicity [32], leading to this chemical diversity. One way to characterize the atmospheres of mini-Neptunes is by applying several models known as *HELIOS* atmosphere model coupled with chemical equilibrium *FastChem* calculator, alongside the *HELIOS-K* opacity calculator that provides absorption cross-sections of atoms and molecules [32]. In the post-process step, the *Helios-O* model is applied to derive the transmission spectra from the computed atmospheric structures [32]. Concretely, *HELIOS* is an open source 1D atmospheric model that aims to determine atmosphere's thermal structure and emission spectrum in radiative-convective equilibrium [32, 42, 43]. Figure 3.1 shows different volume mixing ratios for the atmospheres of sub-Neptunes.

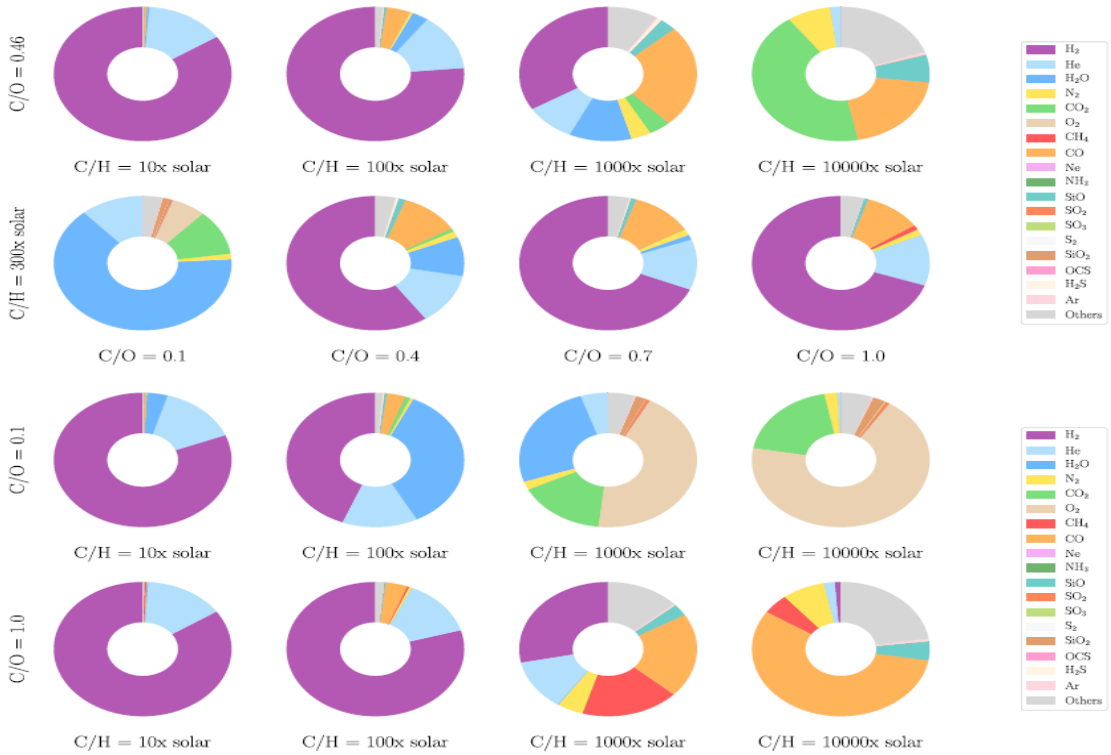

Figure 3.1: Theory predicts chemical diversity in the atmospheres of sub-Neptunes beyond what is expected for gas-giant exoplanets. These 'chemical pie charts' represent the volume mixing ratios of the different atmospheric constituents. They are motivated by the work of Moses et al. (2013) but are derived from self-consistent radiative transfer and equilibrium chemistry models. The carbon-to-oxygen ratio (C/O) and elemental carbon abundance (C/H) of the top two rows are varied according to fig. 4 of Moses et al. (2013). In the two bottom rows, the calculations of the top one are repeated but for C/O = 0.1 and 1. The self-consistent temperature–pressure profiles corresponding to these different scenarios are shown in Fig. A5. The pressures at which these compositions are shown are taken from the peak of the contribution functions at visible wavelengths. Plot from [32].

Overall, our current knowledge of sub-Neptune extrasolar planets remains strictly limited to theoretical considerations. In other words, the combination of interior and atmospheric models are required to fully describe sub-Neptunes, presented in figure 3.2.

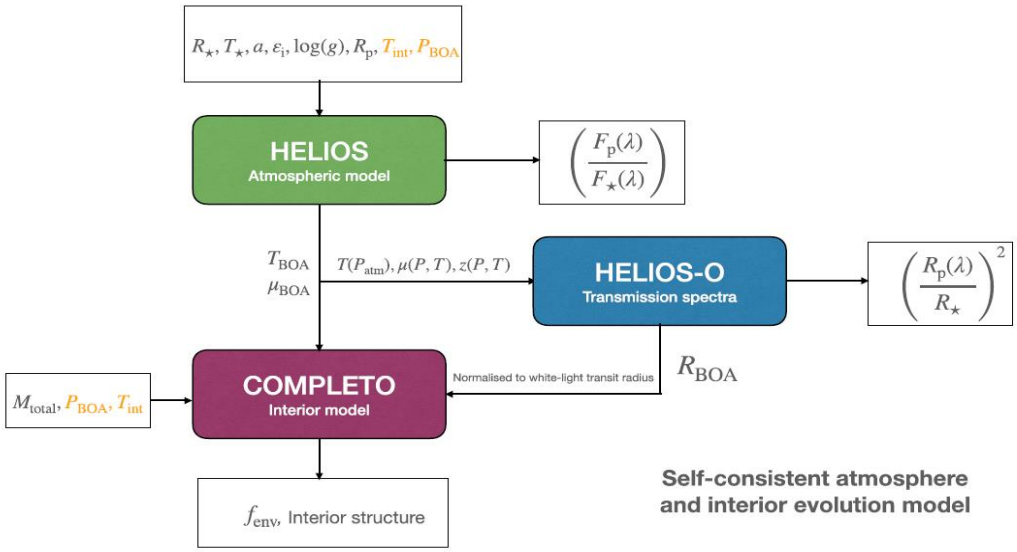

Figure 3.2: Schematic of the logistical flow of *HELIOS* versus *Completo21*. HELIOS takes as an input the radius R_* and temperature T_* of the star, the star–planet separation a, the elemental abundances ϵ_i , the pressure at the bottom of the atmosphere P_{BOA} , the interior temperature of the planet T_{int} , the planet's surface gravity $log\ g$ and the radius of the planet R_p . Some of the outputs of HELIOS for the atmosphere are the P-T structure $T(P_{atm})$, the molecular weight $\mu(P,T)$ and the altitude $z(P,T)$, as well as the emission spectra and secondary eclipse depth $(F_p(\lambda)/F_*(\lambda))$ of the planet. Some of these outcomes are then used in the post-processing stage with *Helios-O* to compute the normalized transmission spectra $(R_p(\lambda)/R_*)^2$ from which the planet radius at the bottom of the atmosphere R_{BOA} is obtained and used as an input in *Completo21*. Completo21 takes as an input the same T_{int} and P_{BOA} (indicated in yellow) used in HELIOS. In addition, it also receives the total mass of the planet M_{total} , the temperature T_{BOA} and the molecular weight μ_{BOA} at the bottom of the atmospheres from the HELIOS outputs. Finally, *Completo21* provides the envelope mass fraction f_{env} and the interior structure of the planet as an outcome. Schematic from [32].

The chemical diversity of their atmospheres has been confirmed by using self-consistent radiative transfer and equilibrium chemistry models [32, 42, 43]. The development of more sophisticated instrumentation alongside the JWST capabilities will be required to provide more accurate spectral features of transmission spectra and enhance our knowledge of sub-Neptunes. It is thus difficult to precisely estimate the exact number of detections of sub-Neptunes since they are often mixed with super-Earths given the quite similar sizes and mass ranges. It is thought that both planetary types differ from constraints on bulk and atmospheric compositions. However, the KST mission genuinely concludes that the vast most exoplanets have masses and radii between the Earth and Neptune, which allows us to postulate that sub-Neptunes and super-Earths would be the dominant exoplanetary types amongst the significant diversity of exoplanetary systems. Overall, sub-Neptune exoplanets are mostly detected throughout transits and radial velocity methods because of their radii and masses.

2.2.1.3 Detection method sensitivity

As defined previously, Neptune-like planets represent planets with similar bulk and atmospheric compositions as Neptune and Uranus. Given their important sizes, masses and semi-major axis, Uranus and Neptune being respectively located at $a_U = 19.2\,AU$ and $a_N = 30.05\,AU$ as indicated in figure 2.4. Thus, these planetary types are much more sensitive to microlensing and transit detection techniques. Detecting via transit method seems particularly relevant for detecting planetary twins of Uranus and Neptune around low-mass stars to look for a low surface temperature.
Based on the data reported within the Nasa Exoplanets Archive, we do not have enough knowledge of the equilibrium temperature of both Neptunian and sub-Neptunian exoplanets, which deeply limits our characterization of ice giants.
Searching for planets like Uranus and Neptune is in fact challenging since many Neptune-like planets and sub-Neptunes discovered up to now are very close to their host stars and are even referred to as hot or warm-Neptunes. If we filter the planets by mass and sizes in the Nasa Exoplanet Archive within the confirmed exoplanets database known as Planetary Systems Composite Data by considering the Neptunian ($14.5\,M_\oplus \leq M \leq 17\,M_\oplus$ and $1\,R_\oplus < R \leq 4R_\oplus$) and sub-Neptunian ($1\,M_\oplus < M \leq 10\,M_\oplus$ and $1.8\,R_\oplus < R < 4\,R_\oplus$) regimes, over 3246 Neptunes and sub-Neptune exoplanets have been reported in the data table [5].

2.2.2 Hot Jupiters

2.2.2.1 Internal structure

Hot Jupiters represent a unique class of planets because not such planets are found in the Solar System given their low semi-major axis (often less than Mercury's orbit) and orbital periods (typically several days). They are defined as gas giant exoplanets physically similar to Jupiter but characterized by an extremely hot effective temperature, hence the "hot" qualificative. Indeed, these planets remain very close to their host star, receiving a high amount of radiation. Besides, hot Jupiters are classified as gas giants although they appear very different from the Solar System gas giants given their proximity with their stars. From a statistical point of view, it is supposed they are orbiting around 1% of solar-type stars, a result based on the Kepler space mission (2009-2018) [44]. However, there is a contradiction between their gaseous nature and extreme temperature conditions, which strongly suggests they formed far beyond their current location. At such high temperatures, the gaseous atmosphere severely escapes. Figure 3.3 depicts possible formation scenarios for hot Jupiters.

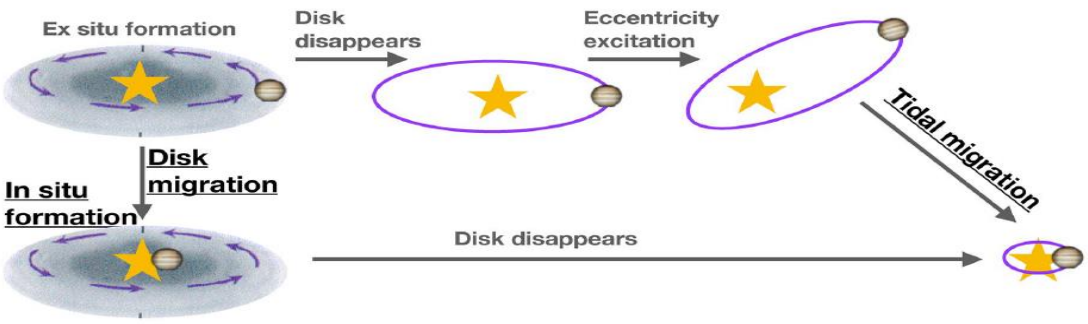

Figure 3.3: Sketch showing possible origins scenarios for hot Jupiters: in-situ formation, disk migration, and high eccentricity tidal migration. Image from [44].

First, hot Jupiters may have their cores and gaseous envelopes formed at their current location, that is the in-situ formation process. Then, another hypothesis suggests that they might have been formed further away and migrated though the initial protoplanetary disk which surrounds a central young star. Alternatively, after the gaseous disk dissipates, hot Jupiters may have formed further out but were perturbed onto a highly eccentric orbit and migrated in the inner part of the planetary system though tidal dissipation. All three scenarios seem viable, but all lead to different properties of these gas giant planets [44]. As taught by planet formation, gas giants are thought to be formed through two main formation mechanisms: either via core accretion in which a rocky planet accretes gas from the protoplanetary disk within the core with a typical mass up to $M_c = 10M_{\oplus}$, or via gravitational instability in which the disk is fragmenting into bound clumps to form the giant planets. The formation of hot Jupiters is still an active ongoing research topic to be solved.

Besides, Hot Jupiters, given their close distance with respect to the host star, are much more likely to evolve differently compared to other gas giants like Jupiter. Indeed, the high amount of stellar irradiation can lead to the heating of the planetary interior, suggesting that the cooling process after planetary formation is not strongly efficient. As a result, the radius of hot Jupiters is expected to increase while they are aging, this is the so-called radius anomaly, as emphasized in figure 3.4.

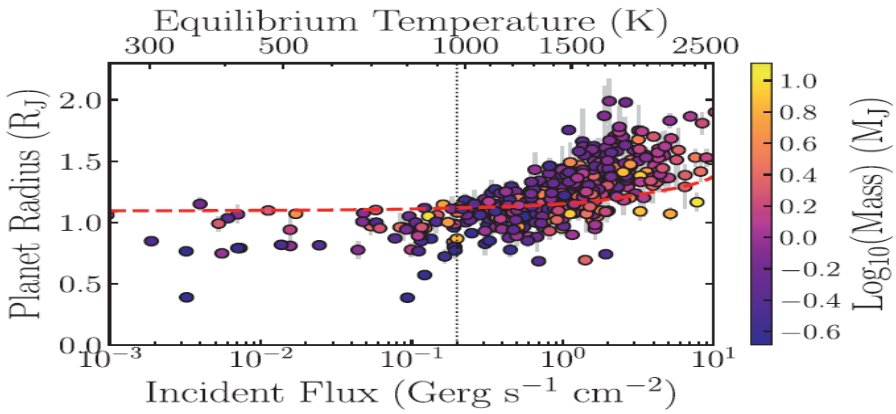

Figure 3.4: The observed radius of extrasolar gas giants (from 0.1 to 13 M_J) plotted as a function of incident stellar flux (and equilibrium temperature) and colored by planetary mass on the log scale. The red dashed line shows an evolutionary model for a Jupiter-mass planet without any additional inflation effects at an age of 4.5 Gyr, and the vertical dashed line displays the flux cutoff (at $T_{P,equi} = 1000K$) below which no radius inflation is found. Plot from [45].

Consequently, the increase of the planetary radius seems to correlate with the level of stellar irradiation, acting as an anomalous power heating the planetary convective interior and driving the radius inflation.
One way to study the interior structure of hot Jupiters is by applying theoretical interior structure models to match the observed mass and radius to constrain the bulk composition, particularly the distribution of heavy elements. However, this remains challenging in the case of hot Jupiters because of the inflated radius problem. This is the reason why we assume the planetary structure *completo21* model presented in Mordasini et al (2012), with several modifications, including photoevaporation and coupling the interior to a non-gray atmospheric model [46]. In order to model the interior of giant planets we apply the following 1D equations

by assuming that the planet is in hydrostatic equilibrium and the planetary luminosity is constant with the radius [46]:

- Conservation of mass: $\frac{dm}{dr} = 4\pi r^2 \rho$ (7.8)
- Hydrostatic equilibrium equation: $\frac{dP}{dr} = -\frac{\rho G m}{r^2}$ (7.9)
- Luminosity conservation: $\frac{dL_P}{dr} = 0$ (8.0)
- Energy transport equation: $\frac{dT}{dr} = \frac{T}{P}\frac{dP}{dr}\nabla$ (8.1)

In all the above equations, all the parameters are identical to the ones considered in equations (7.8)-(8.1) for Neptune-like and sub-Neptune exoplanets. Nevertheless, this model presents some limitations like the distribution of heavy elements that are assumed to be distributed homogeneously in the convective part of the interior and are entirely made up of water [46]. Moreover, this interior model does not include the central core [46].

2.2.2.2 Atmospheres

As emphasized by their close-in orbits with typical orbital periods less than ten days, their mass, generally between, 0.5 M_J and 13 M_J; and their sizes typically between 0.8 R_J and 2 R_J [47], hot Jupiters are relevant exoplanet targets for the transit detection method. Additionally, as discussed in section 2.1.5.3, one way to characterize atmospheres of giant extrasolar planets is to apply the transit spectroscopy technique. Analyzing the atmospheres of hot Jupiters can offer insights on where they formed in the natal protoplanetary disk and the eventual migration pathway into the disk. Furthermore, if hot Jupiters formed beyond the so-called snowline, some volatile elements transitioned from the gas phase to the solid phase. As hot Jupiters are close to their stars, they are strongly tidally locked and receive intense instellation only on their permanent dayside. The extreme contrast between the dayside and the nightside induces a vigorous atmospheric circulation between the two sides [47]. Concretely, the atmospheric circulation is observed through the propagation of a strong super-rotating equatorial jet whose speed reaches a few km/s. [47]. This latter is thought to be associated with waves in hot Jupiters and transports heat from the irradiated dayside to the dark nightside [47].

Moreover, the presence of clouds has a major impact on the shape of the planetary transmission spectrum. Clouds can also mask some molecular features and affect the accuracy of the determination of the abundance of molecules [47]. One way to characterize atmospheric dynamics, especially the presence of such clouds, is by analyzing the phase curve. After the transit, the planet reflects a certain fraction of the stellar light but when this latter arrives at a phase known as secondary eclipse, no stellar light is reflected by the planet, as illustrated in figure 3.5. In addition, the change in stellar light reflected provides insights about the physical processes that drive the heat transport from the dayside to the nightside. Besides, as previously mentioned, the location of hot Jupiters in the protoplanetary disk, beyond or not the snowline, is primordial for constraining the atmospheric evolution, impacting the chemical composition.

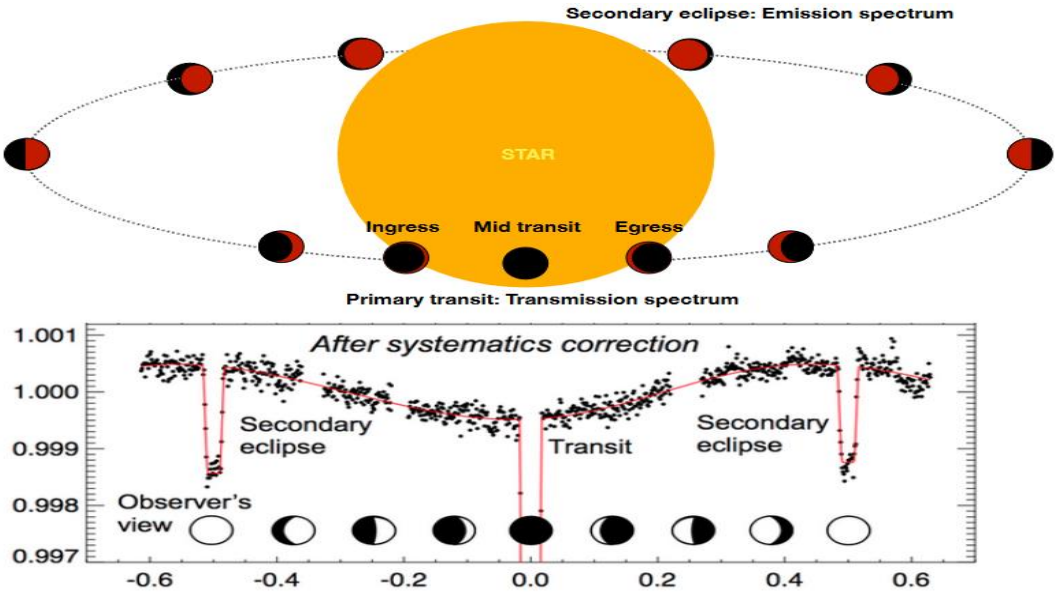

Figure 3.5: Top: An example of the transiting phase curve of the hot Jupiter HD189733 b observed at 4.5 micron with IRAC/Spitzer. During the primary transit, the limbs of the atmosphere are probed just before the secondary eclipse on the day side of the planet is seen. Bottom: Scheme of a transiting exoplanet around its star. The color bar of the planet highlights the day side of the planet (red) and its nightside (black). Plot from [48].

Then, since the discovery of numerous exoplanets, several simple molecules have been detected in the hot Jupiter atmospheres in the recent years such as H_2O, CO, CH_4 and hydrogen cyanide, HCN [49]. However, the error bars related to molecular abundances are too large and do not allow us to constrain the related characteristics to the formation of hot Jupiters. An example of pressure-temperature profile is shown in figure 3.6 for two hot Jupiters with respective semi-major axes of 0.05 AU and 0.1 AU. The plot is created based on the expression for atmospheric temperature as derived in Guillot (2010) paper in which it is assumed that the planet is in radiative equilibrium and that the atmosphere can be described as a plane-parallel gray atmosphere [49, 50]:

$$T_{atm}^4 = \frac{3T_{int}^4}{4}\left(\frac{2}{3}+\tau\right) + \frac{3T_{irr}^4}{4}\mu_*\left[\frac{2}{3} + \frac{\mu_*}{\gamma} + \left(\frac{\gamma}{3\mu_*} - \frac{\mu_*}{\gamma}\right)exp\left(-\frac{\gamma\tau}{\mu_*}\right)\right], \qquad (8.2)$$

where $T_{irr} = T_*\left(\frac{R_*}{D}\right)^{\frac{1}{2}}$ is the irradiation temperature, with D the planet semi-major axis, $T_* = 5778\,K = T_{Sun}$ and $R_* = R_{Sun}$, $T_{int} = 100\,K$ the internal temperature into the core, $\tau = \kappa_{ir} m_{atm}$ the optical depth of the atmosphere, with κ_{ir} the absorption coefficient in the infrared and m_{atm} the column from the top of the atmosphere downwards such that $dm = \rho dz$ where ρ is the atmospheric mass density and z the depth into the atmosphere, $\gamma = \frac{\kappa_{vis}}{\kappa_{ir}}$ the ratio between the optical depths for absorbed and reradiated energy [51] such that $\kappa_{vis} = 4.0 \times 10^{-3} cm^2 g^{-1}$ and $\kappa_{ir} = 1.0 \times 10^{-2} cm^2 g^{-1}$, that best reproduces detailed temperature profiles of well-studied hot Jupiters or defined as the ratio between the absorption coefficients in the visible and infrared wavelengths, $\mu_* = cos(\theta_*)$ with θ_* the angle between the direction of incidence of the stellar irradiation and the local vertical that is set $\theta_* = 0$.

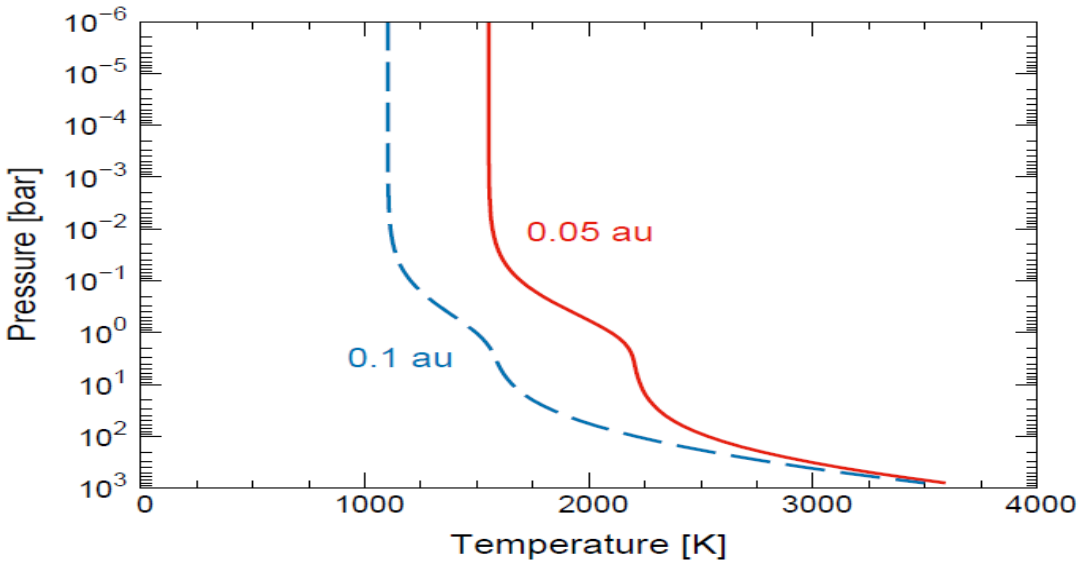

Figure 3.6: The temperature-pressure profiles of two hot Jupiter atmospheres at orbital distances of 0.05 au (red solid curve) and 0.1 au (blue dashed curve). Both profiles are calculated using the analytical formula presented in (8.2) from Guillot (2010). Plot from [49].

Therefore, hot Jupiters are mostly sensitive to the radial velocity and transit detection methods because of their large bulk density. They present strong transit depth and relatively high transit probability. Currently, 409 hot Jupiters have been detected since 1995 if we filter in the Planetary Systems Composite Data of the Nasa Exoplanet Archive [5] by considering equilibrium temperatures between 1000K and 4000K, radii between 0.8 R_J and 2 R_J, masses between 0.5 M_J and 13 M_J and typical orbital periods less than ten days.

2.2.3 Super-Earths

2.2.3.1 Internal structure

As emphasized by the results of the Kepler space mission, the vast majority of exoplanets detected have radii and masses between that of the Earth and Neptune. The sub-Neptunes are found among these planets, whose internal structures are continuously investigated. However, there is another planetary type that appears to be the most promising for the search of habitable conditions and are referred to as super-Earths. These planets are typically characterized by masses such that $1M_\oplus < M_p \leq 10M_\oplus$ and effective radii definition range is subject to evolution. We choose to adopt the conventional range of the 'radius valley', relative to the radius distribution of small planets, which enables to differentiate super-Earths from sub-Neptunes within the radius valley $1.5R_\oplus < R_p \leq 2R_\oplus$ [52]. Although the terms "super-Earths" and "sub-Neptunes" are sometimes used interchangeably in literature, the conventional value of 1.8 $R_\oplus$ is adopted to distinguish the two planetary types, as shown in figure 3.7. The radius distribution of small planets presents two peaks at ~ 1.3 and ~ 2.4 $R_\oplus$, with the corresponding two peaks that are the super-Earths and sub-Neptunes. The bimodality of the radius distribution with the two peaks was first observationally confirmed by the California-Kepler survey [53].
The origin of this radius valley is still actively debated but current two main scenarios are proposed to explain it. On one hand, it is thought that the gap radius is due to planets being stripped of their H/He envelopes through an atmospheric mass loss mechanism and remain as bare rocky cores, with photoevaporation induced by high-energy stellar irradiation [54, 55] and

core-powered mass loss [56, 57] presented as prevalent scenarios. On the other hand, the second scenario is based on planet formation and predicts that water-rich planets migrate inwards from beyond the snowline [58]. Moreover, there is an inconsistency with the fact that sub-Neptunes would be water-poor worlds and feature only pure H/He gaseous envelopes. [59] Therefore, it is proposed that the second peak ($\sim 2.4\,R_{\oplus}$) is rather populated by the presence of mostly water-rich planets [60].

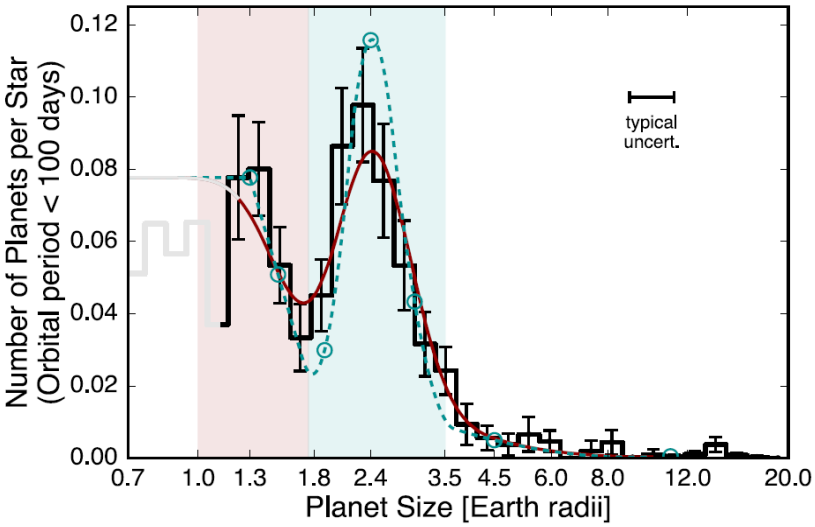

Figure 3.7: Top: completeness-corrected histogram of planetary radii for planets with orbital periods shorter than 100 days. Uncertainties in the bin amplitudes are calculated using a suite of simulated surveys. The light gray region of the histogram for radii smaller than $1.14R_{\oplus}$ suffers from low completeness. The histogram plotted in the dotted gray line is the same distribution of planet radii uncorrected for completeness. The median radius uncertainty is plotted in the upper right portion of the plot. Bottom: same as the top panel with the best-fit spline model over-plotted in the solid dark red line. The region of the histogram plotted in light gray is not included in the fit due to low completeness. Lightly shaded regions encompass definitions of "super-Earths" (light red) and "sub-Neptunes" (light cyan). The dashed cyan line is a plausible model for the underlying occurrence distribution after removing the smearing caused by uncertainties on the planet radii measurements. The cyan circles on the dashed cyan line mark the node positions and values from a spline fit. Plot from [53].

Besides, as mentioned in section 2.2.3, planets with radii larger than 1.6 $R_{\oplus}$ (e.g mini-Neptunes) are much likely to retain their atmospheres, mainly made of gases such as hydrogen and helium. Nevertheless, planets with sizes smaller than $1.6\,R_{\oplus}$ are more probably characterized by a rocky interior composition.

Then, investigating the internal structure of super-Earths, as for other exoplanet categories, seems quite challenging because of the lack of in-situ data. Indeed, geophysical techniques are conventionally used to break the degeneracy between the internal layers of the planetary bodies. One way to infer directly the structure of a planet is by applying the seismic refraction technique. This technique is designed to detail the deep layers of the planetary interior by studying the propagation of seismic waves throughout different media. From an experimental point of view, the seismic-refraction method measures the time a seismic-energy pulse takes to travel from a source point to several receivers after being redirected by one or more subsurface interfaces. From the time measurements of these seismic waves, divided into two categories that are the compressional (P-waves) and shear (S-waves) waves, it is possible to infer the depth of each layer and the compositional geological materials of the internal layers. Thus, it is

experimentally impossible to obtain super-Earths in-situ data given the highly far distances. This is the reason why we must model the internal structure by taking the model previously considered for other exoplanetary populations. Let us model the interiors of super-Earths as spherically symmetric, hydrostatic and differentiated planetary bodies into an MgS_iO_3 mantle and Fe core [60]. We apply the following differential equations to describe the distribution of mass (m), gravity (g), pressure (P), density (ρ) and temperature (T) with respect to the planet radius r. The equations are typically solved within a spherical shell of thickness $dr = 1\ km$ and integrated over the total planetary radius R with a total mass M [60]:

- $\frac{dm(r)}{dr} = 4\pi r^2 \rho(r)$ (8.3)
- $\frac{dg(r)}{dr} = 4\pi G\rho(r) - \frac{2Gm(r)}{r^3}$ (8.4)
- $\frac{dP(r)}{dr} = -\rho(r)g(r)$ (8.5)
- $\frac{d\rho(r)}{dr} = -\frac{\rho^2(r)g(r)}{K_s(r)}$, (8.6)

where $K_s(r)$ is the isentropic bulk modulus calculated as a function of the isothermal bulk modulus $K_T(r)$, which is related to the density ρ applying the third order Vinet EOS [61, 62]:

$$K_s(r) = K_T(r)[1 + \alpha(r)\gamma(r)T(r)] \quad (8.7)$$

$$K_T(r) = K_0 x^{-\frac{2}{3}}[1 + (1 + \theta x^{\frac{1}{3}})(1 - x^{\frac{1}{3}})]\ exp[\theta(1 - x^{\frac{1}{3}})], \quad (8.8)$$

with α, γ and T the thermal expansivity, the Gruneisen parameter and the temperature, respectively. Equation (8.8) accounts for the effect of the thermal expansion on the bulk modulus. x is the ratio between the uncompressed density ρ_0 and the density $\rho(r)$ such that $x = \frac{\rho_0}{\rho(r)}$ and $\theta = \frac{3}{2}(K_0{}' - 1)$. All physical parameters with 0 in subscript refer to values for which these parameters are found at $P = 0$. For instance, K_0, ρ_0 and K_0' are the zero pressure values of the isothermal bulk modulus, density and K_T first-order derivative, respectively.

The Gruneisen parameter γ variation with depth and thermal expansivity α can be parameterized as power laws:

$$\gamma(r) = \gamma_0(x(r))^{\gamma_1},\ \alpha(r) = \alpha_0(x(r))^3\ , \quad (8.9)$$

where γ_0, γ_1 and α_0 are constants given inside each compositional layer in figure 3.8.

The core and mantle are assumed to form two convective layers with a temperature profile described by an adiabatic temperature gradient:

$$\frac{dT_{ad}(r)}{dr} = -\frac{\rho(r)\gamma(r)g(r)T(r)}{K_s(r)} \quad (9.0)$$

Additionally, the table represented in figure 3.8 provides also reference material properties of the different layers, where we assume the surface conditions $P_0 = 1atm\ \rho_0 = 3226\ kg\ m^{-3}$. Surface gravity is straightforwardly expressed as $g_0 = \frac{GM}{R^2}$ and the internal structure model

equations (8.3- 9.0) are integrated from the surface inward, over $\frac{R}{dr}$ spherical shells until m and r at the center are close to 0, taking an accuracy for r of at least dr (1 km).

Constant	Peridotite	Perovskite	Post-perovskite (ppv)	Post-ppv1	Post-ppv2	Liquid Fe	Solid Fe
ρ_0 (kg m^{-3})	3,226	4,109	4,260	4,417	4,579	7,700	8,160
K_0 (GPa)	128	261	324	402	499	125	165
K_0' (n.d.)	4.2	4	3.3	2.7	2.2	5.5	4.9
γ_0 (n.d.)	0.99	1	1.48	1.5	1.5	1.6	1.6
γ_1 (n.d.)	2.1	1.4	1.4	1.4	1.4	0.92	0.92
α_0 ($*10^{-6}$ K^{-1})	20	20	20	20	20	40	40

Figure 3.8: Material thermodynamic constants for each layer considered in the model. Parameters are derived from Stixrude and Lithgow-Bertelloni (2005) for peridotite, Dorfman et al. (2013) and Lundin et al. (2008) for perovskite, Sakai et al. (2016) for post-perovskite, and Smith et al. (2018) for solid Fe. For liquid Fe, recent shock data on Fe-7Si alloy from Wicks et al. (2018) are considered. For post-ppv1 and post-ppv2, to calculate their $\rho_{0,}$, K_0 and $K_0{}'$, the same percentage variation then that observed for perovskite to post-perovskite transition are used. Table from [60].

In the present super-Earth interior model, given the material for each layer given in table from figure 3.8, the mantle can be divided into up to five layers: a peridotitic upper mantle (pd), perovskite (pv), post-perovskite (ppv) and potentially ultrahigh pressure phases called post-post -perovskites (ppv1 and ppv2). These last two layers are thought to be a combination of silicates such as $Mg_2SiO_4, Mg_2SiO_5, MgO$ and SiO_2 [60]. Figure 3.9 shows several density and pressures profiles by assuming core mass fractions (CMF) of Solar System terrestrial planets that are Mercury, Earth and Mars with respective values of 0.68, 0.32 and 0.2.

The radii and masses of super-Earths can be linked by the following power law :

$$\frac{R}{R_\oplus} = \alpha\left(\frac{M}{M_\oplus}\right)^\beta, \tag{9.1}$$

where α and β are coefficients given in table from figure 4.0.

Another important process to consider for the investigation of super-Earth interiors remains the solidification of the inner core, which is of notorious importance for generating a dynamo, creating the planetary magnetic field by convective motions. However, the core crystallization does not guarantee core convection because of the supercritical buoyancy if the core in thermally stratified [63]. The temperature of the core-mantle boundary (CMB) T_{CMB} is thus determinant to investigate the structure and thermal state of the core. Indeed, the coexistence of solidus and liquidus states of the core depends on the size of the super-Earth, the temperature of the CMB and the CMF [63]. Figure 4.1 gives an overview of the different states of the core

assuming CMF of the three mentioned terrestrial planets and shows that the core state is dependent on the planet mass and CMB temperatures, at start and ending of the crystallization core process. The CMB temperatures are fitted using polynomial interpolation [60]:

$$T_{CMB}^{start} = a(\frac{M}{M_{\oplus}})^2 + b(\frac{M}{M_{\oplus}}) + c \tag{9.2}$$

$$T_{CMB}^{end} = d(\frac{M}{M_{\oplus}})^2 + e(\frac{M}{M_{\oplus}}) + f \ , \tag{9.3}$$

where a, b, c, d, e and f are constants given in the table of figure 4.0.

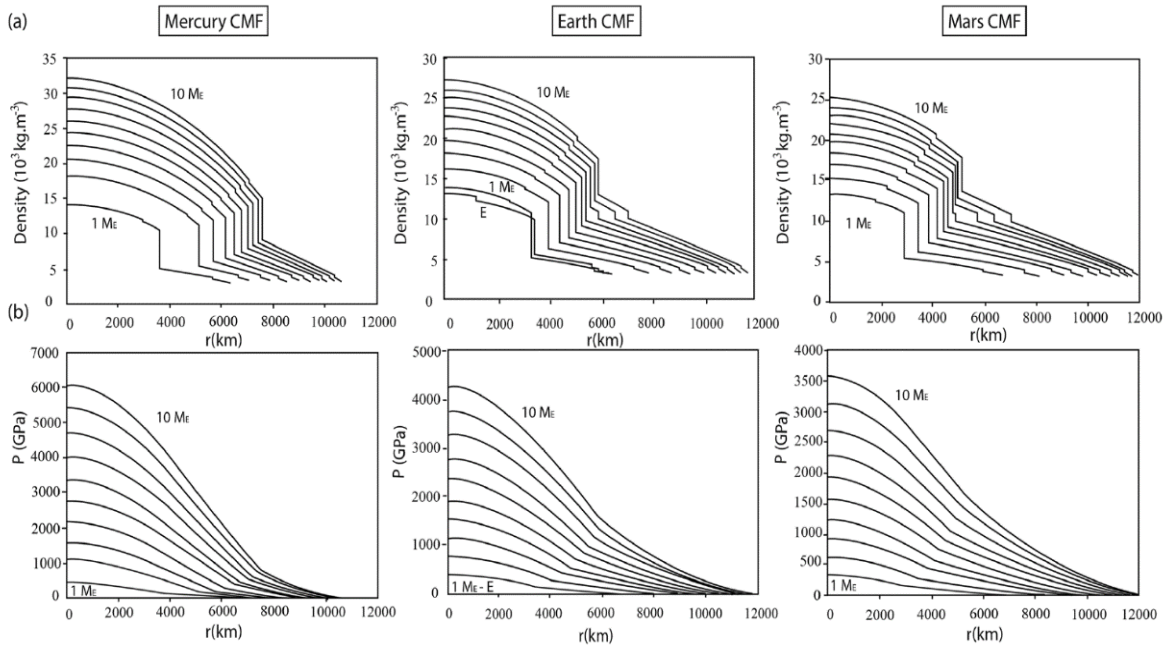

Figure 3.9: Density (a) and pressure (b) profiles in super-Earths of masses ranging within $[1 - 10M_{\oplus}]$. Left, center, and right panels consider core mantle fractions of 0.68 (Mercury like), 0.32 (Earth like), and 0.2 (Mars like), respectively. Here the temperature at the bottom of the core is considered similar to the solidus of $MgSiO_3$ (see Stixrude, 2014). Plots from [60].

CMF	α	β	a	b	c	d	e	f
0.32 (Earth like)	1.03	0.2579	24.6	1695	6041	−30.4	1555	3298
0.68 (Mercury like)	0.97	0.2356	50.8	782	8942	−12.5	946	3277
0.2 (Mars like)	1.07	0.256	14.1	1674	6040	−23.4	1581	3472

Figure 4.0: Coefficients of the power laws relating planetary radii with planetary masses (α and β, Equation (9.1)) and polynomial laws relating the temperature at the core-mantle boundary for which the core starts (a, b, and c, Equation (9.2)) or finishes crystallizing (d, e, and f, Equation (9.3)), for different core mass fraction (CMF). Table from [60].

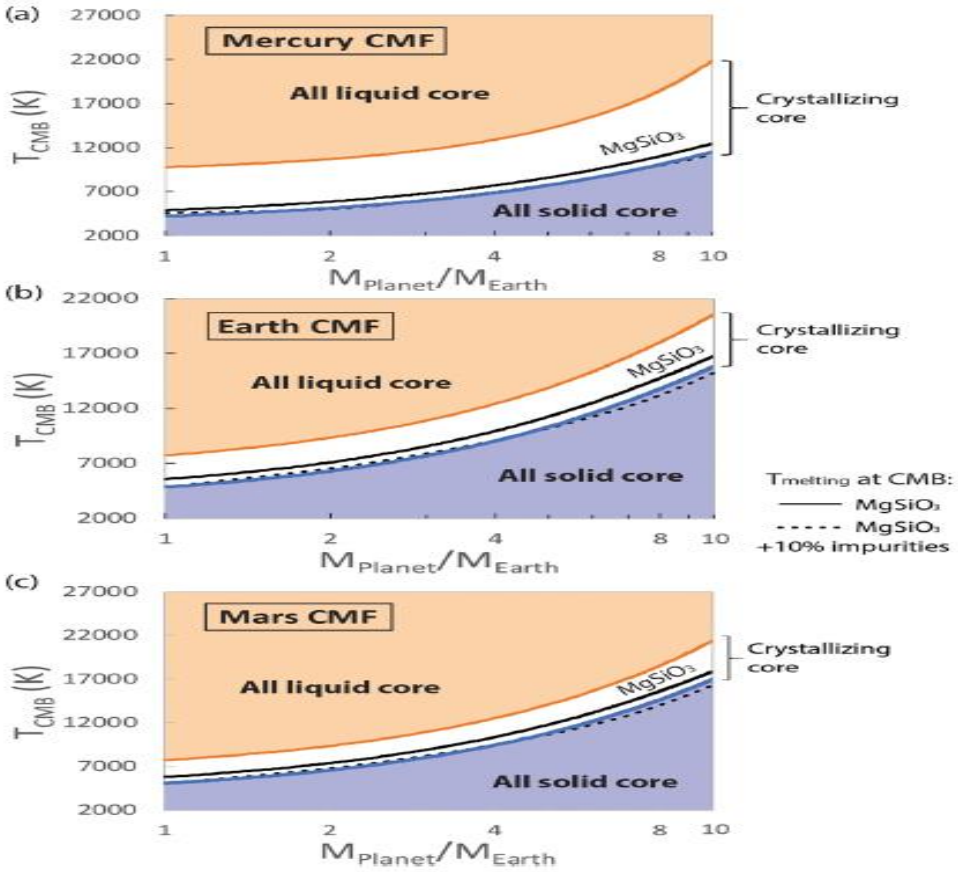

Figure 4.1: Temperature at the core mantle boundary, at which the Fe core is fully liquid (orange areas), starts crystallizing (below orange curve) and is fully solid (blue areas). The white area denotes the regime where both a solid inner core and liquid outer are present. Panels correspond to core mass fractions similar to that of Mercury (a), Earth (b), and Mars (c). Solid black and dotted black curves indicate the temperature at the CMB where the top of the core is at melting temperatures of $MgSiO_3$, and $MgSiO_3$ with additional 10% impurities, respectively (Stixrude, 2014). Plots from [60].

Moreover, it is relevant to note that the range of T_{CMB} for which the core can exist in both solidus and liquidus states is larger when the CMF is large, which is twice larger in a Mercury-like CMF than that of the Earth and of Mars. Similarly, the range of T_{CMB} favoring a partially liquid core increases with the planet mass. It is thought that this effect is due to the larger difference in pressure between the bottom and the top of the core for larger planets and due to the slower increase of the core temperature relative to the Fe melting curve [60]. Overall, super-Earth exoplanets present a larger temperature range over which an inner core grows and provide compositional buoyancy to generate a core dynamo [60], necessary to the existence of the planetary magnetic field, a paramount factor that increases habitability for a planet because of the protection against intense stellar irradiation and cosmic rays.

Then, studying the internal structure of super-Earths is critical to determine whether plate tectonics process is occurring or not. In geology, tectonic activity refers to any crustal deformation caused by motions of the planetary surface, including those induced by compression or extension of the crust. For instance, plate tectonics occurs on Earth and is due

to the convection in the mantle. This is the key factor that drives continental drifts across its surface. All the 15 Earth tectonic plates together form the lithosphere. Several puzzling questions can be raised about super-Earths geological activity: Is there active plate tectonics on super-Earths, like is the case of Earth? Are super-Earths environments with plate tectonics in stagnant lid mode tectonics such as on present-day Mars or Venus?

Several efforts regarding the modelling of convective regime within terrestrial planets regimes have been made over the years [64]. Some models conclude that the likelihood of having plate tectonics increases with increasing size and predict a decrease of plate thickness, as well as an increase of shear stresses with increasing planet size. Thus, the process is probably inevitable in the case of super-Earths [64]. One general model to evaluate the likelihood of terrestrial planets is by setting the Boussinesq approximation, which teaches us that all material properties can be considered constant in space and time, with the exception viscosity, depending on temperature and stress through plastic yielding [64]. Additionally, the Boussinesq approximation is an approximation of the Navier-Stokes equations and enables to solve the flow of non-isothermal fluids, especially in natural convection problems. We consider two modes of convection: internally heated and basally-heated convections.

First, we consider the following conservation equations [64]:

- $\nabla . \vec{v} = 0$, (9.4)
- $\nabla . \sigma_{ij} - \nabla p = RaT\hat{z}$, (9.5)
- $\frac{\partial T}{\partial t} = \nabla^2 T - v . \nabla T + H$, (9.6)

where $\vec{v}$ is the velocity field, $\sigma_{ij} = \eta(v_{ij} + v_{ji})$ the deviatoric stress tensor with η the viscosity that depends on the temperature and the stress, p the pressure, T the temperature, $\hat{z}$ the vertical unit vector, t the time, H the internal heating rate, $Ra = \frac{\rho g \alpha \Delta T D^3}{\eta_0 \kappa}$ the Rayleigh number with ρ the density, g the gravitational acceleration, α the thermal diffusivity, ΔT the temperature scale, D the depth of the mantle, η_0 the reference viscosity and κ the thermal conductivity, respectively. Under the assumptions of constant core-mantle radius and incompressibility, both $D \infty S$ and g (the only varying parameters in the Rayleigh number expression) scale proportionally to the planetary radii ratio $S = \frac{R_p}{R_\oplus}$ as [64]:

$$\tilde{\sigma}_{convective} \propto \eta_i \tilde{v} \propto Ra^{\frac{2}{3}} \propto S^{\frac{8}{3}} , \quad (9.7)$$

where η_i is the interior viscosity and v the velocity.

Since the nondimensional internal heating rate is nondimensionalized via D^2 and thus scale as S^2 [64]. The stresses are non-dimensionalized via D^2 [64] and by combining the expression for the yield stress $\sigma^{\sim} = \sigma_y \frac{D^2}{\kappa \eta_0} \infty S^2$ [64] and equation (9.7), we obtain the following result:

$$\frac{\tilde{\sigma}_{convective}}{\tilde{\sigma}_{yield}} \propto S^{\frac{2}{3}} \tag{9.8}$$

, showing that for constant dimensional yield stress, the nondimensional convective stresses increase more rapidly with planet size than the nondimensional yield stress does. This proves that the mobile regime is more likely for larger planets than for smaller planets. Besides, for the depth-dependent yield stress, the appropriate yield stress to take is that at the base of the lithosphere, which is given by the thickness of the thermal boundary layer δ. Under the mentioned assumptions, this thickness will scale with planet size ratio S as [64]:

$$\tilde{\delta} \propto Nu^{-1} \propto Ra^{-\frac{1}{3}} \propto \tilde{S}^{-\frac{4}{3}} \tag{9.9}$$

The effective yield stress (yield stress located at the base of the lithosphere) for basally-heated convection will scale as [64]:

$$\tilde{\sigma}_{yield-effective} = \tilde{\delta}\frac{d\tilde{\sigma}}{d\tilde{z}} \propto \tilde{S}^{-\frac{4}{3}}\tilde{S}^{4} \propto \tilde{S}^{\frac{8}{3}} \tag{10.0}$$

Therefore, by dividing equations (9.7) and (10.0) one may obtain:

$$\frac{\tilde{\sigma}_{convective}}{\tilde{\sigma}_{yield-effective}} \propto S^{0} \propto 1 \tag{10.1}$$

Thus, by accounting for basally-heated convection and a depth dependent yield stress (i.e friction coefficient), the transition from mobile to stagnant lid regime is independent of the planet size [64].

On the other hand, in the case of internally-heated convection, assumptions are slightly different. Indeed, the surface heat flux must be determined from the internal heating rate. The internal viscosity adjusts to temperature variations, especially with heat loss. The entire temperature in the mantle can be assumed to be constant. The steps to derive the ratio between the nondimensional stress and the effective stress are similar to what was done for the basally-heated convection. The temperature-based Rayleigh number is still used but the result would be the same if a heating-based Rayleigh number was applied to the reasoning.

Therefore, putting all calculations aside, the result for the ratio between the nondimensional convective stresses acting on the lithosphere and the effective yield stress is similar to the one obtained in equation (10.1). As a result, the internal-heated convection the transition from mobile to stagnant lid is expected to happen at the same yield stress or friction coefficient for each value of S, both for the constant and depth-dependent yield stresses [64].

In conclusion, in the case of basally-heated convection for super-Earths is much more likely to happen on their interiors compared to Earth-sized planets. In other words, plate tectonics is indubitably inevitable for super-Earths in this convection regime compared to Earth-sized planets [64, 65]. On the other hand, the likelihood of plate tectonics in internal-heating convection mode is equally likely on super-Earths than on Earth-sized planets [64]. In addition to the importance of the convection process driving plate tectonics, other factors might influence plate tectonics such as the presence of liquid water [63, 64]. Super-Earths present active plate tectonics and may be important for the sustainability of any potential lifeform

because of its key role in shaping the planetary surface, raising the question of habitability on such planets.

Overall, the mass of super-Earths being greater than Earth's leads to higher internal pressures and temperatures, which in turn leads to different states of materials in each layer and mineral phases within their interiors. Thus, the internal structure of super-Earths could be similar to the bulk composition of terrestrial planets but with deeper layers composed of a Fe core and a mantle with a silicate-rich composition.

2.2.3.2 Atmosphere

Investigating the atmospheric composition of super-Earth extrasolar planets presents significant importance since we want to assess their habitability, especially by detecting biosignatures even though some molecular species behaving as biosignatures might represent a false positive for detections in biosignatures. Super-Earths have no analogs in the Solar System in terms of their masses, sizes and atmospheric type. Indeed, the Solar System comprises the gas/ice giants and terrestrial planets. Gaseous and icy giants are characterized by primary hydrogen/helium dominated atmospheres which reflect the chemistry of the initial protoplanetary disk. On the other hand, terrestrial planetary bodies possess secondary atmospheres whose composition is influenced by outgassing process driven by their mantles and geological cycles, enabling the circulation of volatiles between the atmosphere and the surface. Super-Earths would have an intermediate type of atmosphere that could be characterized as hybrid, representing a combination of geochemical outgassing and primordial leftover gases [66], as emphasized in figure 4.2. However, the full description of atmospheric chemistry lying in super-Earth atmospheres is still unknown and future observations by JWST and other scheduled telescopes will be needed to accurately constrain their composition. Thus, a unified theoretical model of outgassing chemistry needs to be developed to study the chemistry of both secondary and hybrid atmospheres because the true nature of super-Earth atmospheres is partly unclear.

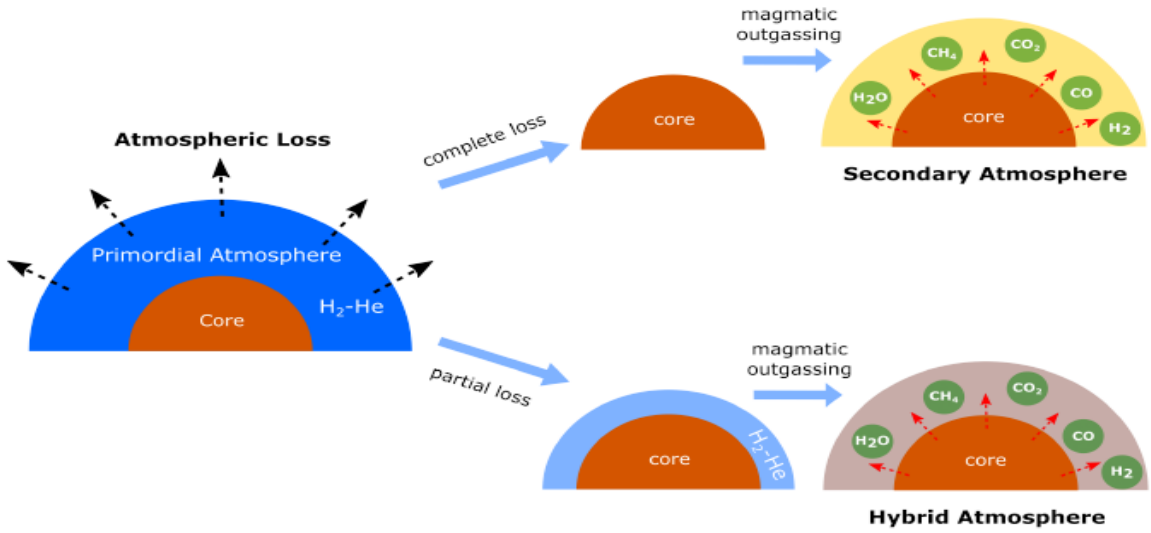

Figure 4.2: Schematic comparing secondary and hybrid atmospheres. Secondary atmospheres are fully sourced by geochemical outgassing, while hybrid atmospheres derive from outgassing into a primordial hydrogen-helium envelope left over from the process of formation and evolution. Image from [66].

Since we cannot directly break the interior degeneracy, the only way to study super-Earths is by examining their atmosphere via transmission spectroscopy. Some studies suggest that the examination of atmospheric properties such as metallicities or mean molecular weight could break the degeneracy of the interior structure and constrain the bulk composition [67, 68, 69].

An interesting example of super-Earth transmission spectroscopy is TOI-836b, with a radius $R_{TOI-836b} = [1.704 \pm 0.067]\, R_{\oplus}$, an equilibrium temperature $T_{equi,TOI-836b} = [871 \pm 36]\, K$, a minimum mass of $M_{TOI-836b} = 4.5^{+0.92}_{-0.86}\, M_{\oplus}$, and orbits the K-dwarf star TOI-836 [70,71]. This planet atmosphere was observed through two transits via the JWST NIR-Spec using the high-resolution (resolving power $R \sim 2700$) G395H mode, resulting in the $[2.8, 5.2]\ \mu m$ wavelength range for the transmission spectrum [70]. Data reduction was applied using two independent pipelines that are *Exo-TiC-JEDI* [72] (Exoplanet Timeseries Characterization – JWST Extraction and Diagnostic Investigator) and *Eureka!* [73]. *Exo-TiC-JEDI* is a package that performs end-to-end extraction, reduction, and analysis of JWST time-series data from *uncal* files through to light curve fitting to produce planetary spectra [72]. *Eureka!* aims to provide an end-to-end pipeline taking raw, uncalibrated FITS files, yielding precise exoplanet transmission and/or emission spectra [73]. The transmission spectrum of TOI-836b is shown in figure 4.3. Given the size of TOI-836b, it is unlikely that it is made of a hydrogen/helium dominated gaseous envelope.

Besides, the JWST capability to operate in a broad coverage of the IR window enables to detect a variety of molecular species, where the presence of aerosols such as clouds and hazes can affect the width of the molecular lines as well as the atmospheric scale height (see equation 6.5) of the transmitted planetary spectrum, where one suitable proxy of the average molecular weight can be the metallicity, expressed in terms of solar metallicity. Figure 4.4 computes respectively the average molecular weight as a function of metallicity and the transit depth with respect to the wavelength. Overall, no precise conclusion can be drawn regarding the atmospheric composition of TOI-836b except the strong evidence from figure 4.3 that the atmosphere is not likely to be characterized as hydrogen/helium dominated atmosphere.

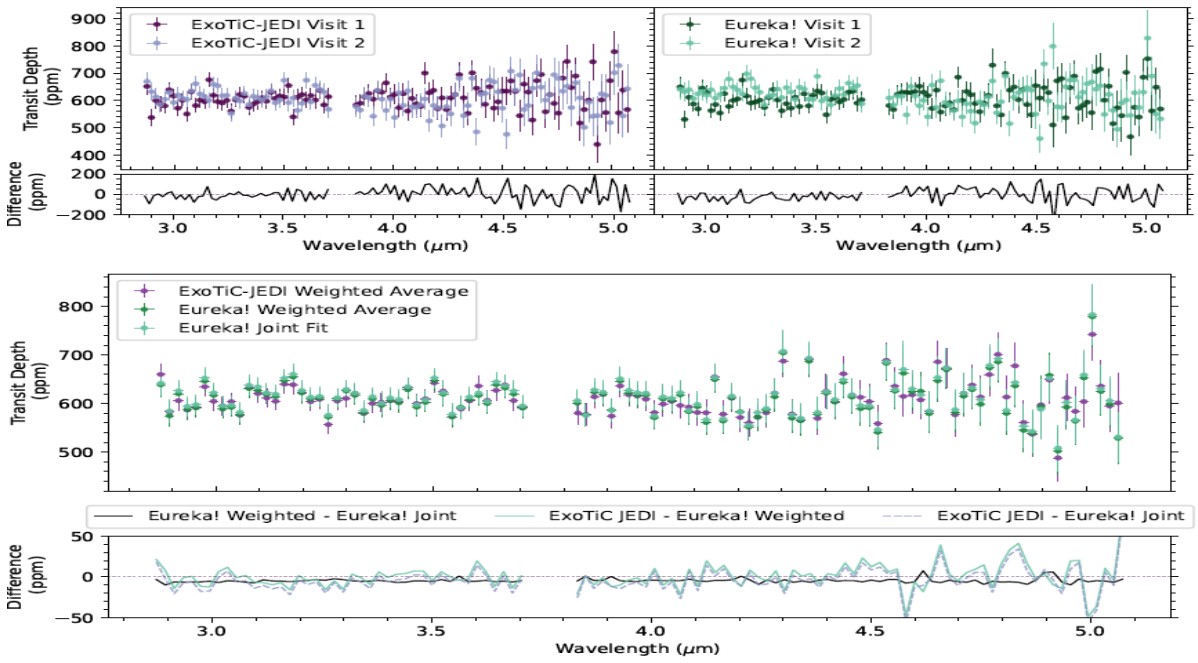

Figure 4.3: Top, Upper Panels: Individual visit transmission spectra *for ExoTiC-JEDI* (left, purples) and *Eureka!* (right, greens). Lower Panel: Difference between individual visit

transmission spectra for *ExoTiC-JEDI* (left) and *Eureka!* (right). On average, the *ExoTiC-JEDI* reductions for visit 1 and visit 2 are consistent to within 39 ppm, while the *Eureka!* reductions agree to within 48 ppm. The *ExoTiC-JEDI* and *Eureka!* reductions are consistent with each other to within the median transit depth uncertainty for both visit 1 and visit 2. Bottom, Upper Panel: Weighted average transmission spectrum from the two visits from the *ExoTiC-JEDI* (purple) and *Eureka!* (light green) reductions and joint fit transmission spectrum from the *Eureka!* reduction (dark green). Lower Panel: Difference between each of the combined *ExoTiC-JEDI* and *Eureka!* transmission spectra in ppm. As the difference between the two *Eureka!* methods is less the 5 ppm (black line), the two *ExoTiC-JEDI– Eureka!* lines are difficult to distinguish (coloured lines). On average, the combined visit *Eureka!* and *ExoTiC-JEDI* spectra are consistent to within 10 ppm. Plots from [70].

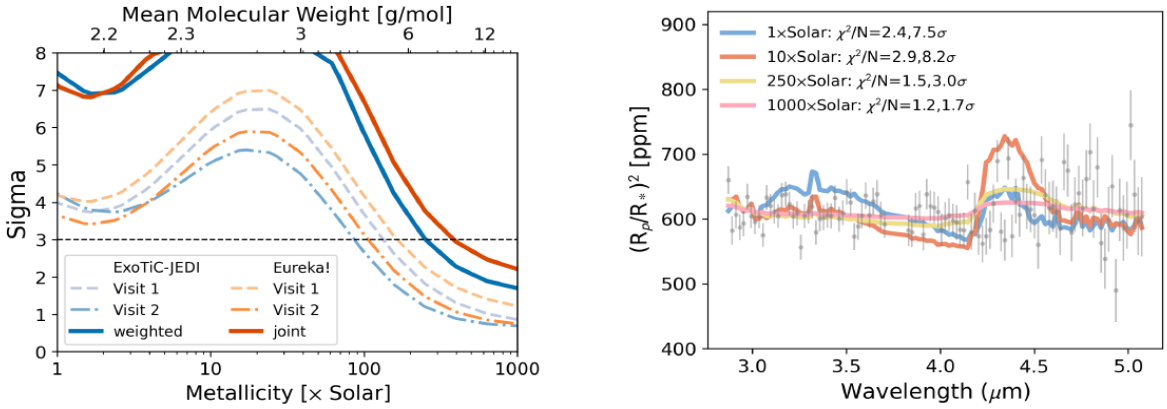

(a) (b)

Figure 4.4: (a) For a single choice in opaque pressure level (0.1 bar) we show the parameter space that can be ruled out in metallicity. Blue lines show the reductions for ExoTiC-JEDI (Visit 1, 2, and weighted) and orange lines show the reductions for Eureka! (Visit 1, 2, and joint). The black-dashed line indicates the 3σ level, below which we are unable to confidently rule out models. Ultimately our data rules out metallicities < 250×Solar, corresponding to a mean molecular weight of ∼ 6 g mol−1. (b) For four of the metallicity cases shown in (a), we show the spectra relative to the weighted data from ExoTiC-JEDI. We also indicate the χ2/N and σ for reference. Plots from [70].

Overall, the atmospheric composition of super-Earths remains unknown but probably chemically richer because of their hybrid nature. Those planets are much more likely to have plate tectonics, driven by convection in the mantle and leading to potential outgassing. The outgassing process thus generates a diverse atmospheric composition. As a result, the atmosphere could be made of volatile gases such as methane, carbon dioxide, water vapor, carbon monoxide or even leftover hydrogen, as shown in figure 4.2 for the case of hybrid atmospheres.

By filtering super-Earths with the mentioned radii (1 $R_{Earth} < R_p < 1.8\ R_{Earth}$) and mass (1 $M_{Earth} < M_p < 10\ M_{Earth}$) ranges from other exoplanetary populations in the Planetary Systems Composite Data, we find that at least 1201 super-Earths have been detected [5]. This number is not a definitive number since the database does not provide the atmospheric composition of super-Earths and these latter can be mixed with sub-Neptunes given their relatively close bulk density.

Chapter 3

Investigation of super-Earths habitability

In this chapter, we will study the different sets of parameters required to assess the habitability of super-Earths in addition to planetary properties as discussed in section 2.2.3. First and foremost, we will study how the planetary orbit influences the environmental conditions such as effective temperature and atmospheric pressure, especially if the planet is within the habitable zone. Then, we will discuss the stellar activity impact on the detection of the planet and the atmosphere, resulting in a change of the surface conditions, especially the stability of liquid water. Finally, we will analyze the Nasa Exoplanet Archive, the benchmark for exoplanets database, by implementing a Python program aimed at assessing the habitability of exoplanets, especially super-Earths.

3.1 Planetary system properties

3.1.1 Orbital dynamics

Another relevant factor for assessing the habitability of super-Earths is the orbital configuration of the planetary system in which they lie, where we assume Keplerian orbits. Indeed, the planetary system architecture plays a key role in habitability, especially in setting the orbital evolution, as well as the amount of stellar flux the planet receives, ultimately affecting the climate evolution of super-Earths. It thus sets the surface conditions, especially the equilibrium temperature. Planetary dynamics is then crucial for investigating the long-term habitability (depending on the global surface energy balance) of the extrasolar planet for two main reasons. First, the full description of the orientation (obliquity) and spin-state (intrinsic rotation) of the planet is necessary to compute the time-dependent host stellar flux, primarily impacting the uppermost layer of planet's atmosphere. Then, the interaction between the exoplanet and other celestial bodies in the planetary system induces gravitational tidal effects that may affect habitability such as with the presence of nearby moons, like in the case of the Earth alongside the Moon. Indeed, the Moon helps to the sustainability of life with diverse effects ranging from the control of oceans' tides, stabilization of the wobble of the axial tilt and the moderation of the climate.

Let us derive the tidal force between the host star and the surrounding planet and identify the effects on this latter.

We first consider the gravitational force, denoted F_g, exerted co-jointly between the star and the planet:

$$F_g = \frac{GM_* M_p}{r^2}\,, \tag{10.2}$$

where M_* is the stellar mass, M_p the planetary mass and r the distance between the star and the planet.

Then, the distance between the near and far sides Δr of the planet needs to be considered for the calculation of the tidal force. The gravitational forces exerted by the star at the near side F_{g1} and the far side F_{g2} of the planet at respective distances $r - \frac{\Delta r}{2}$ and $r + \frac{\Delta r}{2}$ are formulated as:

$$F_{g1} = \frac{GM_*M_p}{(r-\frac{\Delta r}{2})^2} \text{ and } F_{g2} = \frac{GM_*M_p}{(r+\frac{\Delta r}{2})^2} \tag{10.3}$$

The tidal force is thus simply defined as the gravitational force difference between the two bodies:

$$F_{tidal} = F_{g1} - F_{g2} \tag{10.4}$$

Equation (10.4) can be further simplified by applying the polynomial approximation $(1-x)^{-1} \approx 1 + nx,\ for\ |x| < 1$.

Following calculation in equation (10.4), one may obtain:

$$F_{tidal} = \frac{GM_*M_p}{r^2}\left[\frac{1}{(1-\frac{\Delta r}{2r})^2} - \frac{1}{(1+\frac{\Delta r}{2r})^2}\right] \tag{10.5}$$

By applying the binomial approximation mentioned above, the expression for the tidal force is:

$$F_{tidal} = \frac{GM_*M_p}{r^2}\left[\frac{1}{(1+\frac{\Delta r}{r})} - \frac{1}{(1-\frac{\Delta r}{r})}\right] \tag{10.6}$$

After simplification of equation (10.6) the final expression for the tidal force between the star and the planet is given by:

$$\boxed{F_{tidal} = \frac{2GM_*M_p}{r^3}\Delta r} \tag{10.7}$$

While we mainly account for tides generated by the host star on the planet, additional tides can be induced by other bodies in the planetary system such as other planets and moons. As shown by the $\sim \frac{1}{r^3}$ dependence in equation (10.7), the tidal force is much stronger for moons than the tidal force exerted by the host star, as emphasized between the Earth and the Moon. One paramount condition for the moon is to remain located at a minimum distance so that this latter avoids being torn apart by the planetary gravity. This is the definition of the so-called Hill's sphere, i.e the gravitational sphere of influence of a major body onto a minor body and is expressed as:

$$\boxed{R_H = a_p\left(\frac{M_p}{3M_*}\right)^{\frac{1}{3}}} \tag{10.8}$$

Additional factors such as rotational rate and obliquity, i.e the angle between the rotational axis and the orbital axis, can also affect the long-term habitability, especially climate evolution because these parameters determine the amount of instellation distributed over the spherical

geometry of the planet. Moreover, the amount of the stellar flux $F_p = \frac{L_*}{4\pi r(t)^2}$,with $r(t)$ derived from Kepler first law, acting as the main energy contributor to the planet and thus contributes to the energy balance on the planet, is indubitably varying because of the varying distance between the host star and the planet, shaping the planetary orbit. The planetary orbit shape is expressed by the eccentricity e such that $0 \leq e \leq 1$, ranging from circular to hyperbolic orbits. It straightforwardly implies that highly eccentric planets receive less stellar flux than those that are closer to the star.

Therefore, since the rotational rate is defined as the rate at which energy is delivered on a particular planetary location, it can substantially bring changes to the energy balance, as well as condensation cycles, silicate weathering [74] and globally affects the atmospheric circulation. Figure 4.5 represents some simulations that show the effect of the rotational rate on atmospheric dynamics in the case of the Earth but can be extrapolated to super-Earths because of their terrestrial nature. The increased albedo due to a fast rotator behavior appears to be detrimental to habitability because the planet reflects more stellar light to the interstellar medium and thus has a cooling effect on the planet.

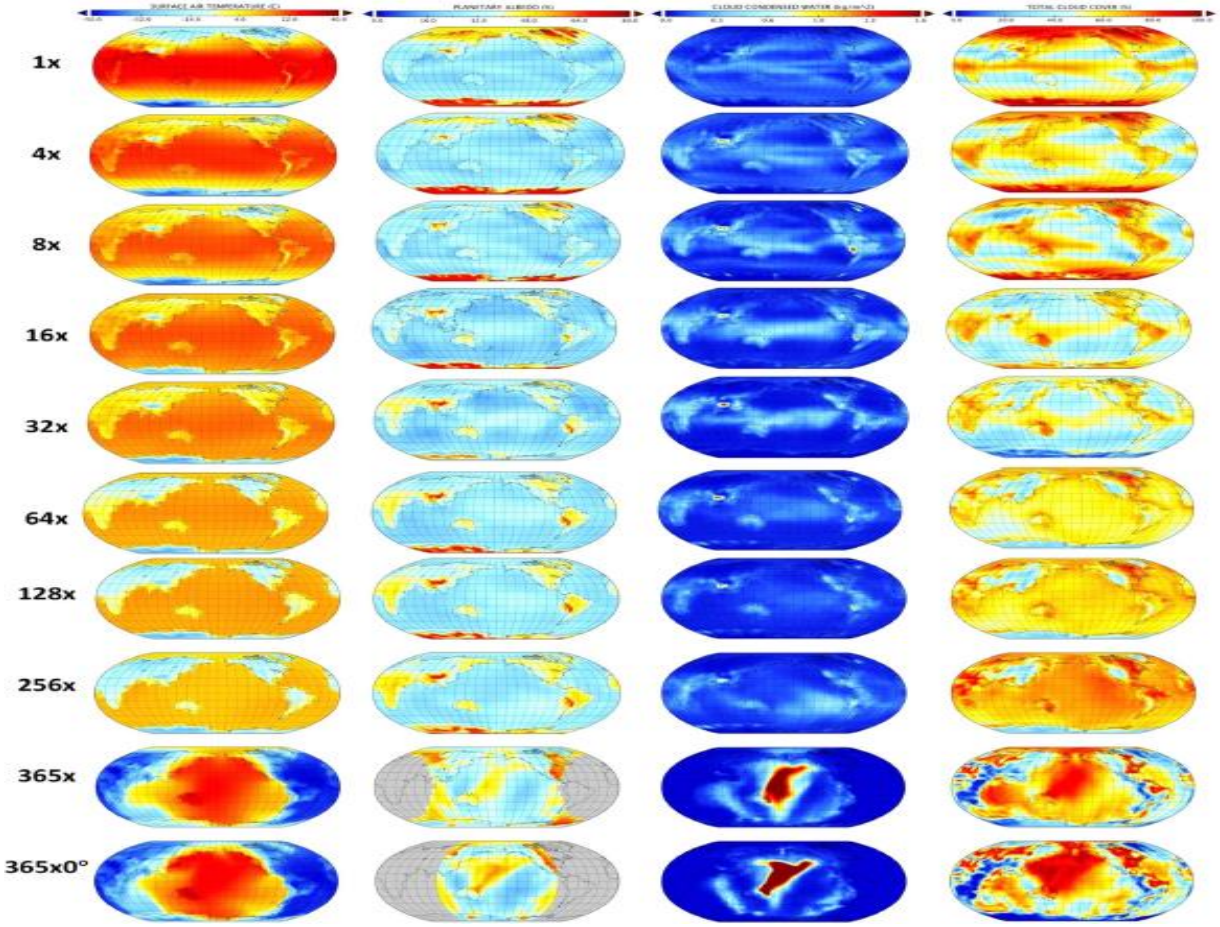

Figure 4.5: The effect of rotation rate on atmospheric dynamics, showing a multiplier of Earth's present rotational rate on (from left to right) surface air temperature (in °C), planetary albedo, column-integrated water cloud-condensed water, and total cloud cover. Plot from [75].

Regarding obliquity, it can be noticed that it has effects on long-term habitability, especially obliquity oscillations. The oscillations of a planet rotational axis may undergo various timescales and are driven by the presence of other planetary bodies in the planetary system [76].

The main effect of obliquity variations is well observed within climate evolution during planet's history. Obliquity regulates the intensity of seasons while the axial tilt controls the amount of stellar flux for a given latitude, especially for eccentric planets where drastic stellar flux variations can occur. One planetary hemisphere pointing to the star receives a greater amount of incoming stellar radiation when the planet is located at the periastron during the summer compared to the other hemisphere [77]. These hemispheric differences in the stellar flux arise essentially from precession. Thus, the maximum stellar flux a planet receives can be quantified from the definitional formula $F_p = \frac{L_*}{4\pi r^2}$ and re-expressed in terms of latitude β [78]:

$$\boxed{F_p = \frac{L_*(sin\delta sin\beta + cos\delta cos\beta)}{4\pi r^2} = \frac{L_* cos|\beta - \delta|}{4\pi r^2}}, \quad (10.9)$$

where δ is the solar declination such that $\delta = \theta cos\,[2\pi(\phi - \Delta\phi)]$, with ϕ the orbital phase and $\Delta\phi$ the offset in orbital phase between periastron highest solar declination in the northern hemisphere, and θ is the obliquity. In the case of the Earth, $\Delta\phi = 0.46$ and $\theta = 23.5°$.

Overall, obliquity is decisive to maintain climate conditions as well as slight astronomical variations with respect to the planetary system architecture, especially the orbital evolution which drives global climate variability such as glaciation periods as emphasized by Earth's history. Thus, assessing potential long-term habitability for any planetary population requires the tandem of eccentricity variations with obliquity and precession cycles.

3.1.2 Habitable zone

As mentioned in the introduction, the habitable zone is an astronomical region, for a given stellar system, in which liquid water can sustain on the surface of a planet, assuming there is sufficient planetary atmospheric pressure. Indeed, the habitable zone can comprise several planets that define inner and outer boundaries of this astronomical region.
In our Solar System, the habitable zone can be computed between the orbits of Venus and Mars but as emphasized by their evolutionary histories, these two latter are not currently habitable. Venus is impacted by a severe greenhouse effect (nearly a mean surface temperature of 740 K), making it extremely hot and characterized by a carbon-dioxide dominated atmosphere, as well as the presence of sulfur-acid rains. On the other hand, Mars remains extremely cold ($T_{surf} = 208K$) and is thought to have lost its primordial atmosphere hydrodynamically, probably due to intense solar radiation. Thus, planets located in the habitable zone are not necessarily habitable.

However, other factors than the star-planet distance also affect planetary atmospheric and surface conditions such as the amount of stellar radiation, which represents the primary source of energy for the planet. As stellar evolution models taught us, the amount of stellar flux received by a planet primarily depends on the mass of the star. High-mass stars are much more luminous than low-mass stars, where luminosity is an intrinsic property that is driven by the fusion reaction process occurring into the core.
For the calculation of the width of the habitable zone, we assume the general model assumed by Kasting et al (1993) [79], which is a one-dimensional climate model for Earth-like planets with $CO_2/H_2O/N_2$ atmospheres, postulating that habitability primarily requires the presence of liquid water on the planetary surface [79]. The inner boundary of the habitable zone is determined from the loss of water via photolysis and hydrogen escape while the outer edge of the habitable zone is set by the formation of CO_2 clouds, leading to a cooling effect on the

planet because of an increasing albedo [78]. This very specific model is known as Conservative Habitable Zone (CHZ) model.

A general method to compute the distances at which the two respective inner and outer boundaries of the habitable zone are located is by initially considering stellar absolute and apparent magnitudes.

For a given star at distance d from Earth, the apparent magnitude is given by Pogson's law:

$$m_v = -2.5log(F) + C = -2.5log(\frac{L_*}{4\pi d^2}) + C, \quad (11.0)$$

where F is the stellar irradiance, L the bolometric stellar luminosity as expressed by Stefan-Boltzmann law, $L = 4\pi R_*^2 \sigma_{SB} T_{surf}^4$, C is a constant set to match observational magnitude measurements with standard magnitude values of stars reported in catalogs.

The absolute magnitude, defined as the magnitude equivalent to the apparent magnitude at distance of 10 parsecs, is given by:

$$M_v = m_v - 5log(\frac{d}{10pc}) \quad (11.1)$$

Thus, the stellar bolometric luminosity $M_{bol,*}$ can be expressed thanks to equations (11.1) and (11.2):

$$M_{bol,*} = M_v + BC, \quad (11.2)$$

where BC is the bolometric correction constant, which depends on the spectral class of the star, with different values of the bolometric correction constant are given in figure 4.6.

Spectral class	BC
B	-2.0
A	-0.3
F	-0.15
G	-0.4
K	-0.8
M	-2.0

Figure 4.6: table showing different values for the bolometric correction constant for various spectral stellar types. Values taken from [80].

The final step is to compute the stellar absolute luminosity L_* by substituting equation (11.2) into equation (11.0) and combining them to obtain the following result:

$$\frac{L_*}{L_{sun}} = 10^{\frac{M_{bol,*} - M_{bol,sun}}{-2.5}}, \quad (11.3)$$

where L_{sun} and $M_{bol,sun}$=4.72 are the solar absolute luminosity and solar bolometric magnitude, respectively.

The location of the inner $r_i(t)$ and outer $r_o(t)$ edges of the habitable zone are thus computed by considering the time-dependent stellar luminosity $L_*(t)$ and by applying a specific choice of critical fluxes $S_{1*}(t)$ and $S_{2*}(t)$ at these edges location [82]:

$$r_i(t) = \sqrt{\frac{L_*(t)}{S_{1*}(t)}}, \tag{11.4}$$

$$r_o(t) = \sqrt{\frac{L_*}{S_{2*}}}, \tag{11.5}$$

where $S_{1*} = 1.1$ $S_{2*} = 0.53$ [81, 82] and $L_*(t)$ is expressed in units of L_{sun}.

In the case of our Solar System, we obtain r_i=0.95 AU and r_o=1.37 AU, which are consistent with the conservative estimates of Kasting et al (1993) [79]. These values belong to the CHZ model values that are defined hereafter and imply that Mars and Venus are not located in the habitable zone.

Nevertheless, a more recent and updated one-dimensional climate model for the calculation of the habitable zone has been proposed and includes radiative transfer analysis that relies on the accurate understanding of the absorption and emission properties of molecules in the atmosphere [82]. These properties are provided by the high-resolution transmission molecular absorption database *HITRAN* and the high-temperature molecular spectroscopic database *HITEMP*. The compilation of *HITRAN* and *HITEMP* is a set of spectroscopic parameters that are used to predict and simulate transmission and absorption mechanisms within the atmosphere. Additionally, the model includes Rayleigh scattering by water vapor.

Regarding the calculation of the habitable zone, the two boundaries are computed with the following method: the inner boundary of the habitable zone requires the use of the effective solar flux $S_{eff} = \frac{F_{IR}}{F_{sun}}$, which is the ratio between F_{sun}, the net incoming solar flux, and F_{IR}, the net outgoing IR flux at the top of Earth's atmosphere. At the top of Earth's atmosphere, the flux received is $F_{sun} \sim 1361\ Wm^{-2}$ and is referred to as the solar constant. However, this incoming flux value corresponds to a flux reached by the area of a circle of area $\pi R_{\oplus}^2$. Instead, we assume the flux to reach the surface of the spherical shape $4\pi R_{\oplus}^2$ and obtain a net incoming flux four times smaller $\sim 340\ W\ m^{-2}$.
On the other hand, the outer habitable zone boundary is calculated by taking the atmospheric partial pressure of carbon dioxide p_{CO_2},, which is set under the assumption that it is fluctuating in the atmosphere because of temperature variations and carbonate-silicate cycle [82]. Besides, a maximum greenhouse limit is revealed by the model and occurs at S_{eff} =0.325, showing that further decreases of the net incoming solar flux would not sustain surface temperatures preventing freezing of liquid water [78]. It is important to mention that the calculations for the outer boundary do not include radiative warming by CO_2 clouds and should be qualified as conservative [82].
Figure 4.7 represents the computations for the inner habitable zone boundary with regards to surface temperature and water mixing ratio. The four results encompass four major habitable zone boundaries: two inner and two outer boundaries. On one hand, the inner edge comprises the runaway greenhouse limit (0.99 AU) [83] and the 'recent Venus' limit (0.75 AU) [83], based on the postulation that Venus surface hosted liquid water during its geological history [83]. On the other hand, the outer edge encapsulates the maximum greenhouse limit (1.7 AU) [83] and the 'early Mars' limit (1.8 AU) [83], also based on in-situ data that genuinely hypothesizes the

existence of a large volume of liquid water on Mars surface 3.8 billion years ago when the solar luminosity was 25% lower [84]. The runaway greenhouse and maximum greenhouse effects limits (at 0.99 AU and at 1.7 A, respectively) [83, 84] encompass the CHZ model (0.99-1.7 AU) [83] while the 'recent Venus' and 'early Mars' limits comprise the Optimistic Habitable Zone (OHZ) (0.75-1.8 AU) [83]. This set of habitable zone boundaries evolving through time is called the continuous habitable zone.

The formula for determining the distance of the habitable zone is given by [84]:

$$d_{HZ} = \sqrt{\frac{\frac{L_*}{L_{sun}}}{S_{eff}}}\, AU, \tag{11.6}$$

where S_{eff}=$S_{eff,sun} + c_1 T_* + c_2 T_*^2 + c_3 T_*^3 + c_4 T_*^4$ is the effective stellar flux, with T_*= T_{eff} − 5780 K. The polynomial coefficients c_1 though c_4 for the CHZ and OHZ boundaries depend on updates of the HITEMP database [84]. This formula is only valid for stars with effective temperatures such that 2600 K ≤ $T_{eff,*}$ ≤ 7200 K [84]. Figure 4.8 displays the four boundaries for the CHZ and OHZ as a function of the stellar types.

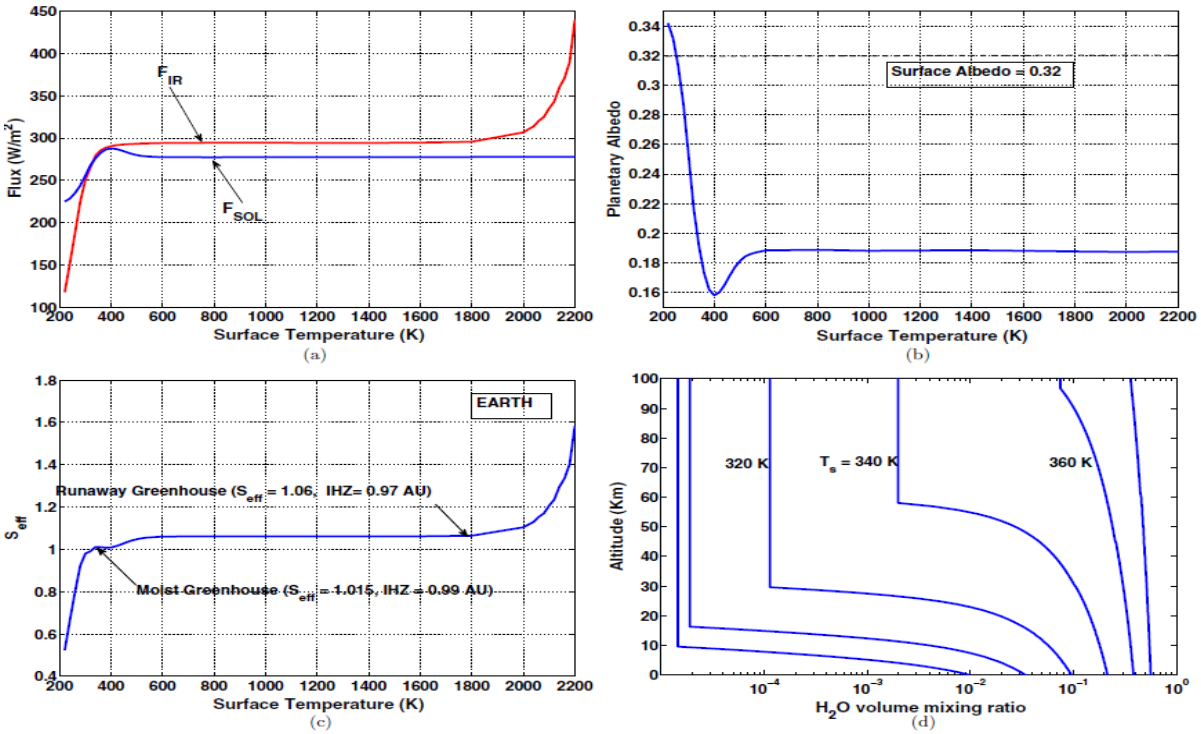

Figure 4.7: Various parameters are shown as a function of surface temperature: (a) net outgoing IR flux and net incident solar flux; (b) planetary albedo; (c) effective solar flux $S_{eff} = \frac{F_{IR}}{F_{sun}}$; and (d) water vapor profile. These calculations were performed with the HITEMP 2010 database. The water-loss (moist-greenhouse) limit, which is most relevant to habitability, is at 0.99 AU, and runaway greenhouse is at 0.97 AU. The corresponding estimates from the Kasting et al (1993) [79] climate model are 0.95 AU for the moist greenhouse and 0.84 AU for the runaway greenhouse. Plots from [82].

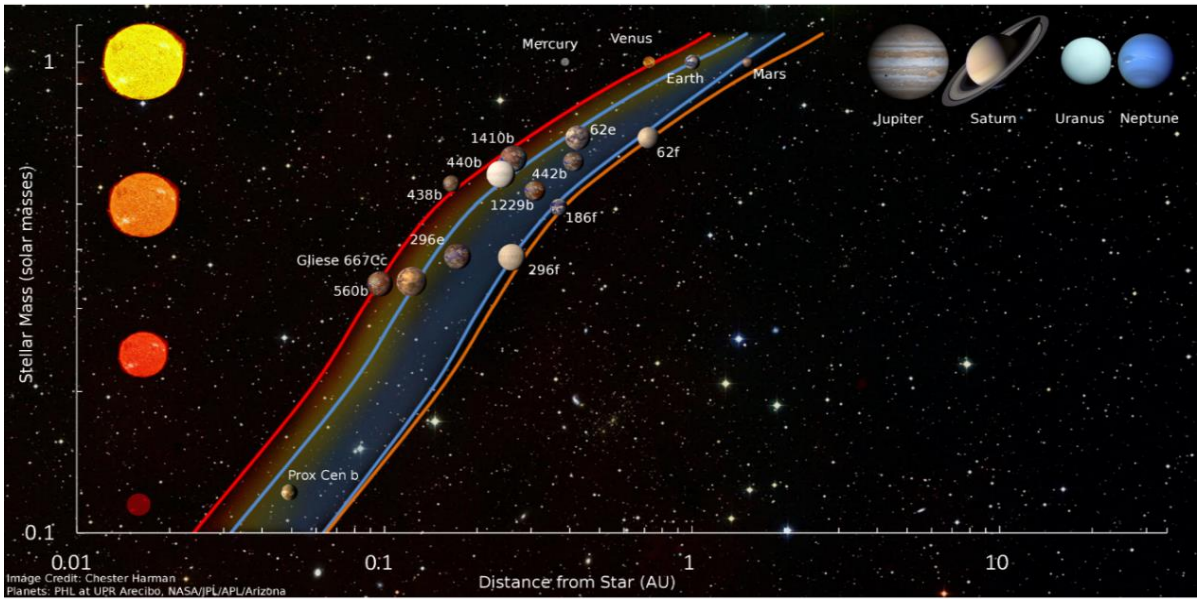

Figure 4.8: Schematic diagram of the traditional orbital distance boundaries of the habitable zone (HZ) for stars of different masses (M, K, G and F stars). The red and orange lines denote the optimistic “recent Venus" (inner) and “early Mars" (outer) edges of the HZ. The blue lines bound the conservative “runaway greenhouse" (inner) and “maximum CO_2 greenhouse" (outer) HZ limits. The Solar System planets, as well as several habitable-zone exoplanets are plotted here for reference. Image credit: Chester Harman. Image from [85].

Then, after discussing general considerations for planets located within the habitable zone orbiting main-sequence stars, let us briefly talk about the Galactic Habitable Zone (GHZ). As emphasized before, the habitable zone remains a very local astronomical configuration, i.e each planetary system has specific boundaries for its habitable zone. Moreover, the location of habitable zone strongly depends on the spectral stellar type because of the amount of irradiation affecting the top of exoplanet’s atmospheres, which in turn may affect surface conditions. However, it is thought that specific regions of the Milky Way may favor conditions for the existence of long-term habitability. According to a galactic evolution model published in 2004 by Lineweaver et al, the GHZ is defined as an annular region lying on the planet of the Galactic disk that possesses heavy elements to form terrestrial planets and offers suitable conditions for biological evolution for the development of complex multicellular life [86]. The model consists in simulating the evolution of four prerequisites for the emergence of complex life: the presence of a host star, enough heavy elements necessary for terrestrial planets formation, sufficient time for biological evolution and an environment free of life-extinguishing supernovae [86].

A probabilistic approach is applied to compute the likelihood of finding the GHZ [86]:

$$P_{GHZ} = SFR \times P_{metals} \times P_{evol} \times P_{SN}, \tag{11.7}$$

where SFR is the star formation rate with $SFR = 1.9 \pm 0.4\ M_{sun}\ yr^{-1}$ [87], P_{metals} the metallicity-dependent probability of harboring terrestrial planets (displayed in figure 4.9), P_{evol} the cumulative integral of a normal distribution of mean 4 Gyr and 1 Gyr dispersion (biological evolution into complex life took nearly 4 billion years on Earth and is assumed to be typical timescale for this evolution), and P_{SN} the probability that life survives once supernovae are blasted. Additionally, P_{SN} is dependent on the supernova danger factor $\xi(r,t)$, at Galactocentric distance r and time of star formation t. This factor is defined as the supernova rate integrated

over the interval $[t;\ t + 4Gyr]$ and is normalized relative to Earth [86], as emphasized by figure 5.0. However, this last probability remains imprecise because of the lack of knowledge on the vulnerability of life to supernovae [86]. Therefore, from the theoretical probability of the GHZ, figure 5.1 is obtained and displays the location of the GHZ.

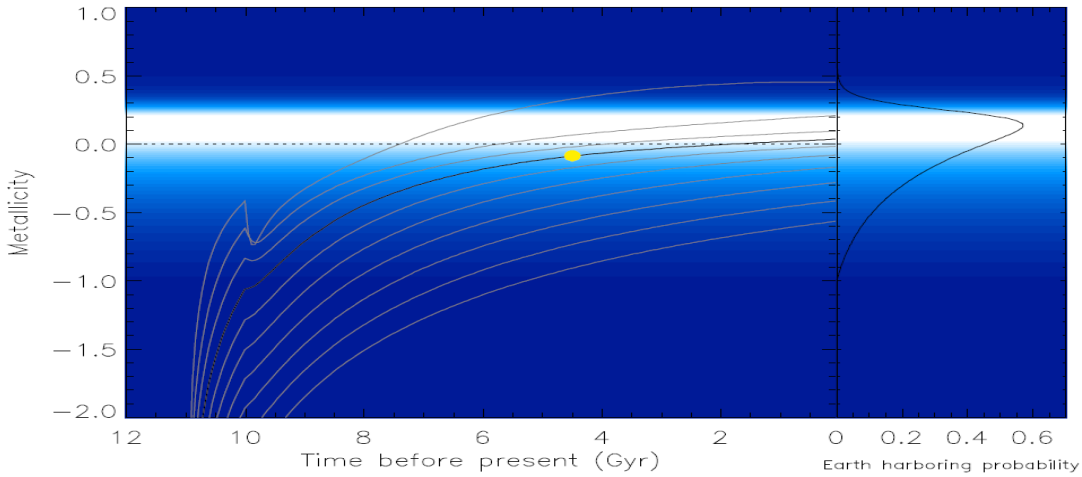

Figure 4.9: The buildup of metals in our Galaxy as a function of time predicted by our simulations. Metallicities at different Galactocentric distances can be compared with the probability of harboring terrestrial planets as a function of the metallicity of the host star [**right**]. Galactocentric distances from 2.5 kpc (upper curve) to 20.5 kpc (lower curve) are shown in 2 kpc increments. The yellow dot indicates the Sun's time of formation and Galactocentric distance of 8.5 kpc. The inner Galaxy accrues metals early and rapidly because of a high rate of star formation, whereas the most distant regions remain deficient in the metals needed to form terrestrial planets. Metallicity is the log of the ratio of the amount of iron to hydrogen in the stars relative to the Sun. Plot from [86].

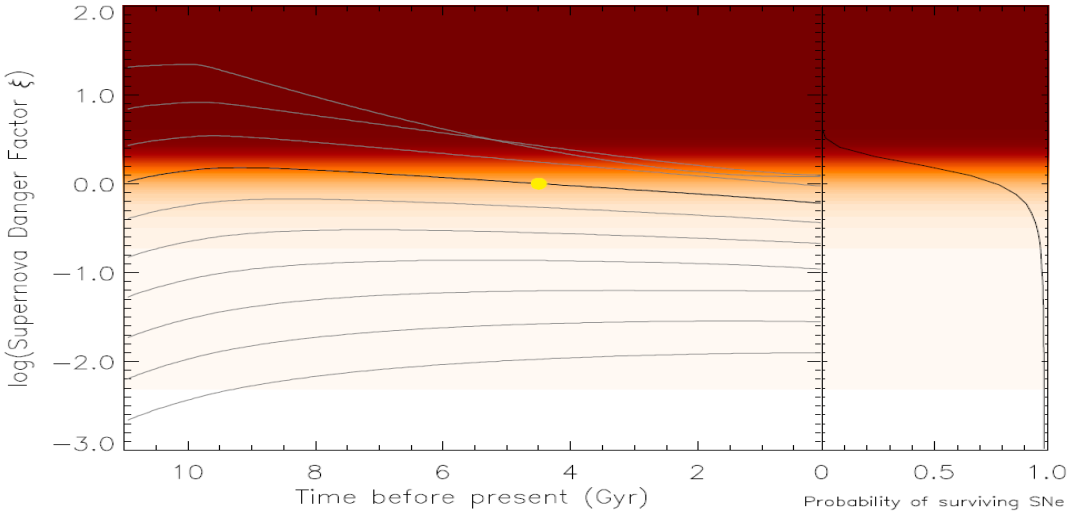

Figure 5.0: The supernova danger factor, ξ, defined as the integral of the supernova rate from t to t + 4 billion years, in units of the Earth's ξ and plotted as a function of time for the same set of Galactocentric distances shown in figure 4.8. In the inner disk, the threat from supernovae (SNe) was once 20 times greater than that faced by the Earth. The inner disk began to run out of fuel for making stars within several billion years, causing both the star formation and supernova rates to decline. Plot from [86].

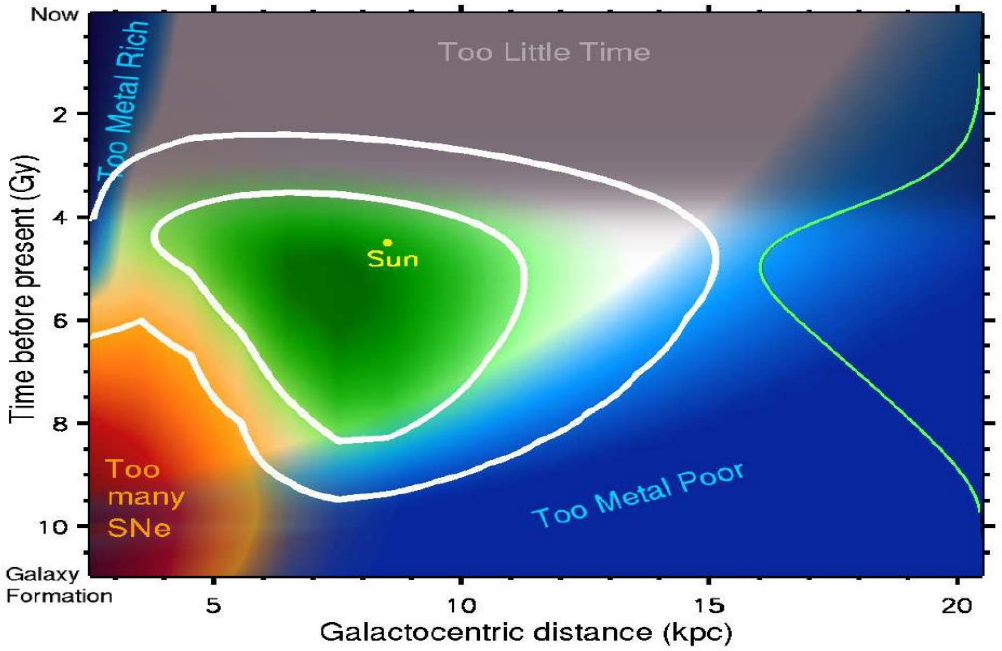

Figure 5.1: The GHZ in the disk of the Milky Way based on the star formation rate, metallicity (blue), sufficient time for evolution (gray), and freedom from life-extinguishing supernova explosions (red). The white contours encompass 68% (inner) and 95% (outer) of the origins of stars with the highest potential to be harboring complex life today. The green line on the right is the age distribution of complex life and is obtained by integrating $\boldsymbol{P_{GHZ}(r,t)}$ over $\boldsymbol{r}$. Plot from [86].

Overall, based on the space and time distributions of the mentioned probabilities, the chemical evolution of our Galaxy suggests that the GHZ is found in an annular region delimited between 7 and 9 kiloparsecs from the Galactic center that expands with time and encompasses stellar populations formed between 8 and 4 billion years ago [86]. In terms of our Galaxy regions, it is unlikely that this GHZ is found neither within the halo, thick disk and inner bulge because of low-metallicity stars populating them and increasing probability of stellar encounters, increasing the impact of the radiation field [86]. Thus, it strongly suggests that these regions may not exhibit terrestrial planets where complex life could exist.

3.2 Stellar astrophysics

3.2.1 Pills on stellar evolution

The evolution of a star remains truly important for the potential long-term habitability on a given orbiting planet. As mentioned in chapter 2, star's luminosity provides stellar flux, indispensable for the planet energy balance and is due to the internal thermonuclear reactions whose requirements are an extremely hot temperature, a significant confinement time and a high number density of particles. For instance, Sun's core hosts a temperature $T_{sun,core} = 1.5 \times 10^7\ K$ and a surface temperature $T_{eff,sun} = 5780\ K$.

According to Vogt-Russel theorem, assuming the stellar structure is in hydrostatic and thermal equilibrium, the mass and metallicity are the predominant parameters that set the stellar lifetime, as emphasized by the Hertzsprung-Russel diagram. Initially, the star, thought to be

formed through the gravitational collapse of a giant molecular gas cloud, which is known hereafter as a protostar, evolves sufficiently with time to enter the so-called main-sequence time. This time is defined as the moment where the thermonuclear fusion reaction occurs during most of the stellar lifespan, which in turn stabilizes the star. However, not all stars manage to evolve to the main sequence because of their extremely low mass. Some parameters called Jeans parameters (mass, density, radius and temperature) are fundamental requirements to activate the collapse of the gaseous cloud and protostar and ignite thermonuclear fusion along the main sequence.

For a gas cloud of radius R, temperature T, and mass M the condition for the gas cloud to start the contraction is expressed as:

$$\frac{GMm_H}{R} \geq kT, \tag{11.8}$$

where $m_H = 1.6 \times 10^{-24} g$ is the mass of a particle located at the periphery of the gas cloud because hydrogen is the main gas component of the cloud, G the universal gravitational constant and k the Boltzmann constant.

The condition expressed in (11.8) can also be re-expressed in terms of the temperature and the density of the gas cloud by taking $M = \frac{4\pi}{3} R^3 \rho$, which leads to $R = \frac{M^{\frac{1}{3}}}{(\frac{4\pi}{3})^{\frac{1}{3}} \rho^{\frac{1}{3}}}$.

Bu substituting into condition (11.8), one may obtain:

$$\frac{Gm_H M \rho^{\frac{1}{3}} (\frac{4\pi}{3})^{\frac{1}{3}}}{M^{\frac{1}{3}}} \geq kT \Leftrightarrow M^{\frac{2}{3}} \geq \frac{k}{(\frac{4\pi}{3})^{\frac{1}{3}} G m_H} \times \frac{T}{\rho^{\frac{1}{3}}} \tag{11.9}$$

$$\Leftrightarrow M^{\frac{2}{3}} \geq \frac{aT}{\rho^{\frac{1}{3}}} \tag{12.0}$$

$$\Leftrightarrow M \geq a^{\frac{3}{2}} \frac{T^{\frac{3}{2}}}{\rho^{\frac{1}{2}}} \tag{12.1}$$

$$\boxed{\Leftrightarrow M_J \geq 10^{23}\, T^{\frac{3}{2}} \rho^{-\frac{1}{2}}\, g\,,} \tag{12.2}$$

where M_J is the Jeans mass and $a = 10^{15}\, g\, K^{-1}\, cm^{-1}$ is the radial acceleration of the gas cloud.

Therefore, equation (12.2) tells us that the ideal place for star formation is a cold and dense environment. Moreover, the gas cloud and the protostars contract during different three timescales: dynamical, thermos-dynamical and thermonuclear timescales, respectively. The contraction regime ends when the newly formed star reaches the thermonuclear timescale.

The dynamical timescale is expressed by considering the equation of an accelerated motion due to gravity as:

$$r = \frac{1}{2} g\, t_d^2, \tag{12.3}$$

where $g = \frac{GM}{r^2}$ is the gravitational acceleration.

In the context of the gas cloud, the dynamical contraction time can be expressed in terms of its density $\rho = \frac{3M}{4\pi r^3}$:

$$\boxed{t_d = \sqrt{\frac{2r^3}{GM}} \Leftrightarrow t_d = \frac{2600}{\sqrt{\rho}} s} \tag{12.4}$$

By assuming a typical density of the interstellar medium, $\rho = 10^{-23} g cm^{-3} = \rho_{ISM}$, equation (12.4) yields for the gas cloud a dynamical contraction time $t_d \approx 10^7 yr$.

Then, the thermodynamic timescale can be derived by first applying the Virial theorem:

$$2K + \Omega = 0, \tag{12.5}$$

where $K = \frac{1}{2} M v^2$ represents the kinetic energy of the gas cloud (pressure) and $\Omega = -\frac{K}{2}$ is the potential energy (gravity). The theorem states that the contraction of the pre-stellar structure leads to half of the energy emitted by the gas structure while the structure is heating up, which yields a decrease of the total internal energy $U = K + \Omega$ or $dU = -\frac{\Omega}{2}$ and an increase of the kinetic energy K. The emission of energy provides the luminosity L that can be expressed as a function of the time derivative of the total internal energy:

$$L = \frac{dU}{dt} \Leftrightarrow L = \frac{1}{2} \left| \frac{d\Omega}{dt} \right| \tag{12.6}$$

$$\Leftrightarrow L = \int_0^t L dt \tag{12.7}$$

$$\Leftrightarrow L = \frac{1}{2} \Omega \tag{12.8}$$

Thus, the thermo-dynamical timescale is formulated as:

$$\boxed{L \times t_{thermodyn} = \frac{1}{2} \frac{GM^2}{R} \Leftrightarrow t_{thermodyn} = \frac{1}{2} \frac{GM^2}{LR}} \tag{12.9}$$

In the case of the Sun, it would take 15 million years for gravitational energy to supply luminosity, which remains a very long timescale.
As a result, the protostar reaches the thermonuclear timescale and can perform the hydrogen-burning process during the main sequence time.

Then, as the star releases energy from the thermonuclear reaction, the generation of the stellar luminosity occurs and scales with star's mass via the following power-law [88]:

$$\boxed{\left(\frac{L_*}{L_{sun}}\right) = \left(\frac{M_*}{M_{sun}}\right)^{3.5}}, \tag{13.0}$$

where L_* and M_* are the stellar luminosity and mass, respectively.

Besides, since the stellar mass is the main determinant for setting luminosity, radius and effective temperature, as emphasized by Stefan-Boltzmann law, mass is also the key factor that enables to compute the main-sequence lifetime (expressed in years) [89]:

$$\tau_{MS} = 10^{10}\left(\frac{M_*}{M_{sun}}\right)^{2.5} \tag{13.1}$$

For a solar-type star, equation (13.1) yields a main-sequence lifetime of 10 billion years while cooler and low-mass stars such as M-dwarfs have a main-sequence lifetime significantly longer than high-mass stars, which is even more than the actual age of the Universe. This is the reason why we have not detected post main-sequence M-dwarfs yet. The Hertzsprung-Russel diagram, shown in figure 5.2 displays the current framework of stellar evolution by plotting the relationship between stellar luminosity and effective temperature or equivalently the absolute magnitude as a function of the spectral type (color). Stellar evolution theory sets two cut-off mass limits for which a star reaches and evolves along the main sequence: stars with a mass lower than 0.08 M_{sun} (brown dwarfs) and higher than 90 M_{sun} do not evolve along the main sequence because such stars are not enough massive to ignite the H-burning process and are too massive to ensure structural stability, respectively. Spectral types are divided into seven classes based on the Morgan-Keenan classification, ranging from the cool M-dwarfs to the extremely hot O-stars [90]. Each letter-class is sub-divided with numbers going from 0 to 9, in order of decreasing temperature [90].

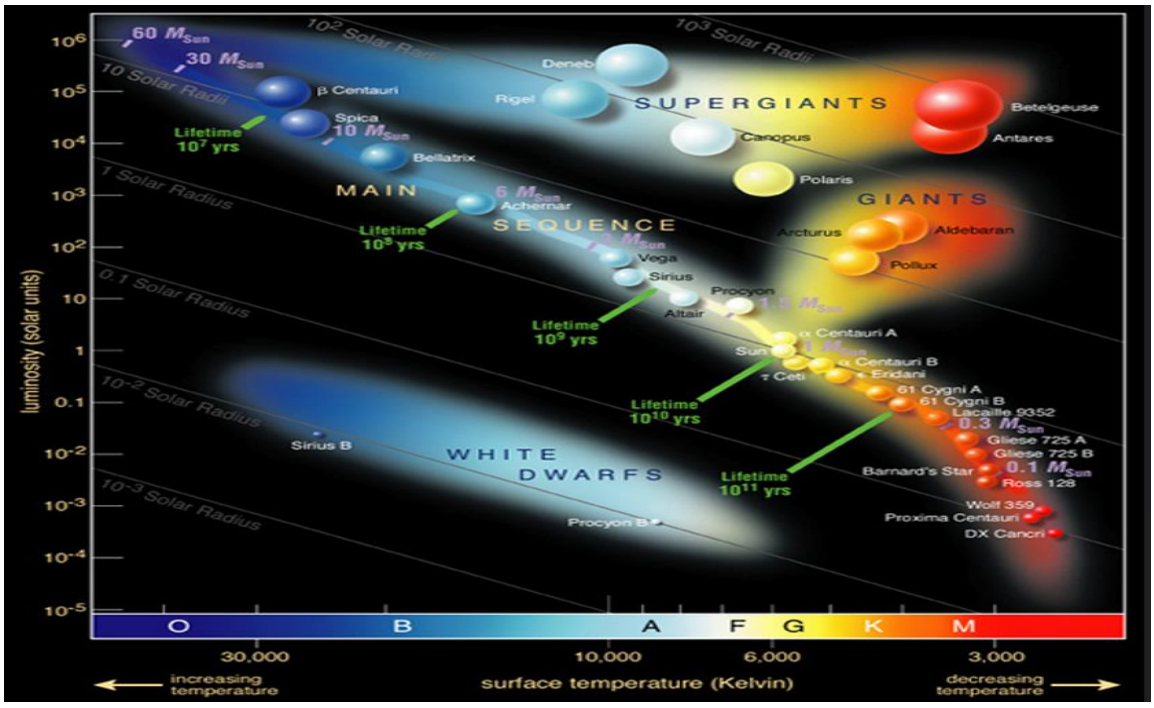

Figure 5.2: Hertzsprung-Russell diagram: the temperatures of stars are plotted against their luminosities. The position of a star in the diagram provides information about its present stage and its mass. Stars that burn hydrogen into helium lie on the diagonal branch, the so-called main sequence. Red dwarfs like AB Doradus C lie in the cool and faint corner. AB Dor C has itself a temperature of about 3,000 degrees and a luminosity which is 0.2% that of the Sun. When a star exhausts all the hydrogen, it leaves the main sequence and becomes a red giant or a supergiant, depending on its mass (AB Doradus C will never leave the main sequence since it burns so little hydrogen). Stars with the mass of the Sun which have burnt all their fuel evolve finally into a white dwarf (left low corner). Image from [91].

As emphasized by the Hertzsprung-Russel diagram, the final evolutionary stage of a star strongly depends on its initial mass: main-sequence high-mass stars ($M_* > 7\ M_{Sun}$) evolve into supergiants, supernovae and neutron stars or black holes; while low-mass stars either evolve within the red giants branch and end up as white dwarfs. The lowest massive stars simply become rapidly white dwarfs without evolving in the red giants branch, like in the case of M-dwarfs. Therefore, the final evolutionary stages have an impact on the long-term habitability of exoplanets, especially super-Earths. It is estimated that red dwarfs, also known as M-dwarfs, represent at least 70% of the global stellar population in the Milky Way [92]. As a result, the search for potentially habitable super-Earths implies detecting these planets around such stars, assuming super-Earths are sufficiently close to M-dwarfs to receive enough stellar flux to regulate surface conditions. These stars appear to be the most promising targets because of their significant main-sequence lifetime, i.e more than the current age of the Universe, thus potentially inducing long-term habitable conditions for nearby orbiting exoplanets, especially super-Earths.

3.2.2 Stellar activity

3.2.2.1 Stellar activity impact on detection methods

3.2.2.1.1 Radial velocity data

The detection of a super-Earth around M-dwarfs via both Doppler spectroscopy and transit methods offers the advantage of obtaining a significant planetary signal, mitigating the stellar activity signal. Stellar activity is a generic term that encompasses numerous stellar phenomena such as flares, feculae or dark spots. For any star, the magnetic field is driven by the internal convection. When the stellar magnetic field interacts with the photosphere, stellar activity is generated. For instance, star's activity can trigger dark spots and/or bright plages that rotate with the star in the photosphere. Such homogeneities on the surface induce radial velocity shifts due to changes in the spectral lines shape and perturbs the Doppler-reflex motion due to the presence of a planetary companion [93].

As mentioned in the section on radial velocity method, stellar activity compromises the detection of the planetary signal. In fact, stellar pulsations have the tendency to mimic the planetary signal in addition to stellar jitter adding a non-periodic signal component to the noise floor of the radial velocity data. An example of stellar activity impact on the planetary signal detection is shown in figure 5.3. Retrieving this perturbation remains an important challenge since terrestrial planets' signatures often lie beneath the noise floor of radial velocity data [93]. One straightforward way of disentangling stellar activity signal and planetary signal in the case of Doppler spectroscopy method is by interpolating radial velocity data via polynomial fitting to subtract the fitted curve to the original data to isolate the jitter from the actual stellar signal. Additional methods exist such as data smoothing (Gaussian filters and other filters) that reduce noise to preserve the main signal or Fourier transform analysis that filters the high-frequency noise, transforming the data into a frequency domain and selectively removing the frequency corresponding to the jitter.

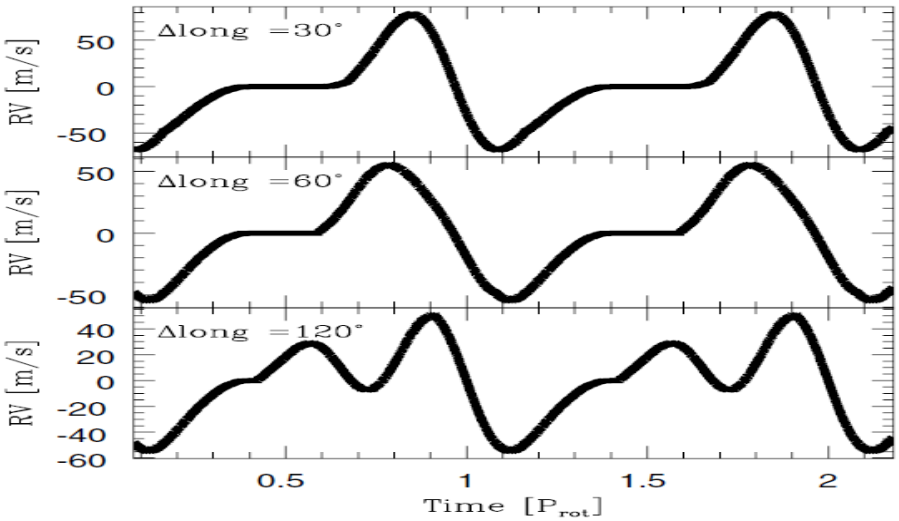

Figure 5.3: RV as a function of time induced by two spots on the stellar surface of GJ674, a moderately active M2.5 dwarf hosting a planet with a 4.69-day period. One spot is at latitude +30◦, the other at the equator. *From top to bottom*: the shape of the variation varies with the difference in longitude between the two spots, labelled in the top left of each panel. Plot from [93].

3.2.2.1.2 Transit surveys

Similarly, stellar activity affects the accuracy of transit surveys with photometric effects such as star spots, eclipsing binaries and other effects [94] and may affect the derivation of the planetary parameters [95]. For instance, as the Kepler mission provided numerous stellar light curves, the main difficulty resides in the mitigation of stellar activity as well as other perturbing noises with regards to planetary signals such as instrumental noise and stellar variability. Likewise, applying machine learning techniques to transit surveys data offers the opportunity to obtain a more accurate light curve, enhancing the planetary signature. Figure 5.4 depicts an example of stellar activity impact, including spots and plages on stellar light curves through chromatic Rossiter-McLaughlin (RM) observations [96].

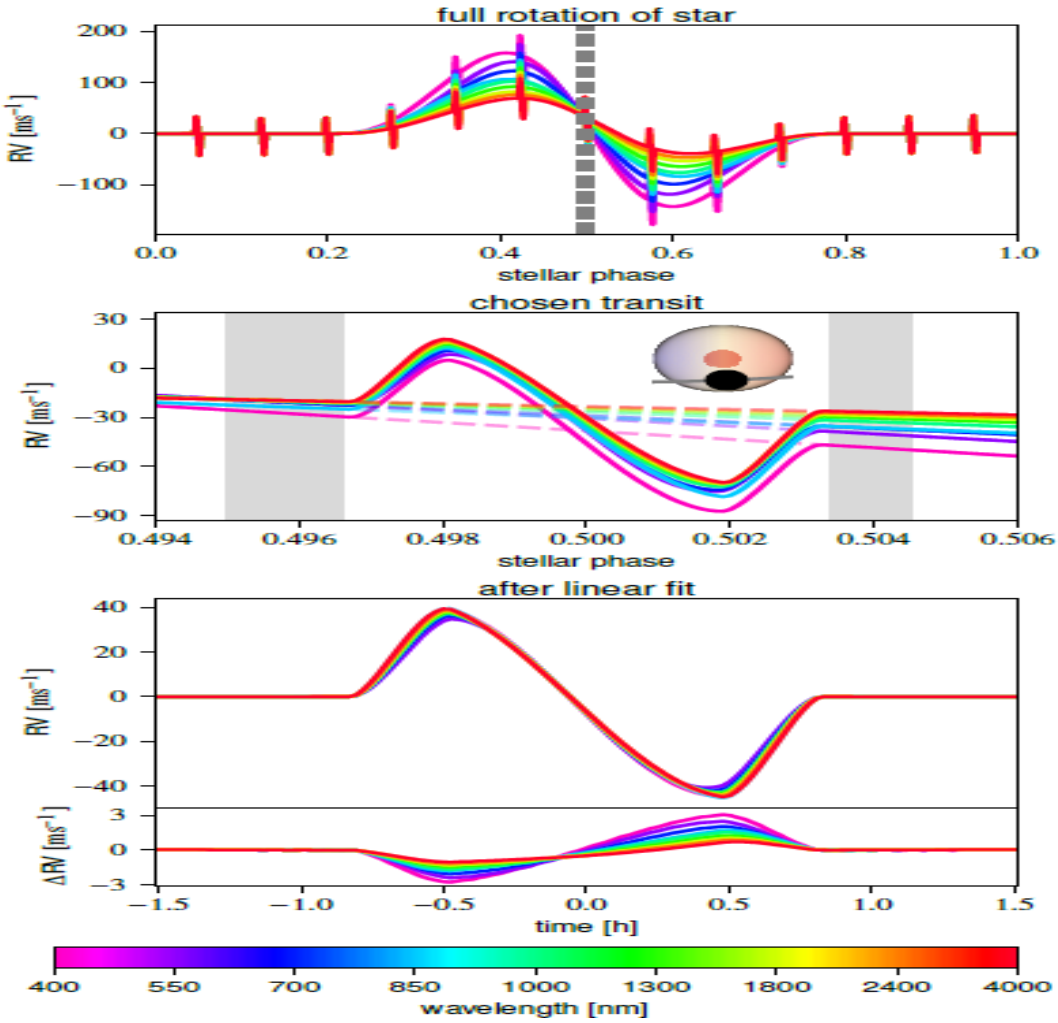

Figure 5.4: Top: RV variation of the star during one stellar rotation, which exhibits a modulation caused by the presence of a stellar spot. On top of that, the planetary RM signals appear every 0.8 days. An ephemeris of the transiting planet is taken in such a way that one of the transit occurs when the stellar spot is at the center of the visible stellar disk (this transit is indicated between two vertical dashed lines). Different colors correspond to different wavelengths as shown in the color-bar. Middle: zoom on the central RM (between two dashed lines in the top panel), and the variation in the out-of-transit RV slope is visible as a function of the wavelength. The gray area shows the regions that are used to remove the out-of-transit slope. Inside this panel, a schematic view of the system is displayed, showing the transit chord and position of the active region on the stellar surface. Bottom: RM curves after the underlying slope is removed by performing a linear fit for each individual wavelength. The lower subplot shows the residual between each RM curve with the RM of a planet that transits a quiet star (without any active region). Plots from [96].

3.2.2.2 Stellar activity impact on planetary habitability

3.2.2.2.1 Atmospheric erosion

As emphasized by their significant main-sequence lifetime, M-dwarfs sustain longer periods of high-stellar activity on the orbiting planets contrary to more massive stars and can affect the potential long-term planetary habitability. Stellar activity includes stellar winds, i.e a mix of

charged particles such as protons and electrons triggered by flares, as well as high-energy radiation such as extreme ultraviolet radiation (XUV). For example, the closest star to the Sun, Proxima Centauri, is a prime target because its radiative activity affects the habitability of Proxima b, characterized as a likely rocky Earth-like exoplanet located from Proxima Centauri with an estimated semi-major axis of 0.0485 AU [97], having a minimum mass of nearly 1.3 $M_{\oplus}$ [97], a radius $R_{pro-b} = 1.4^{+0.3}_{-0.2}\, R_{\oplus}$ [98] and receives a stellar flux $S_p = 0.65\, S_{\oplus}$ [97]. Proxima b is thus classified as a super-Earth. Several observations of Proxima Centauri have been performed regarding the flaring activity, especially the detection of the first naked-eye brightness superflare event [99]. Figure 5.5 shows the time variation of Proxima Centauri brightness. This type of event strongly leads to the desiccation of Proxima Centauri b atmosphere, thus reducing the likelihood of sustaining habitable conditions. It is estimated that this rocky world receives 60 times more XUV flux than the present-day Earth and ten times more far-UV flux [100].

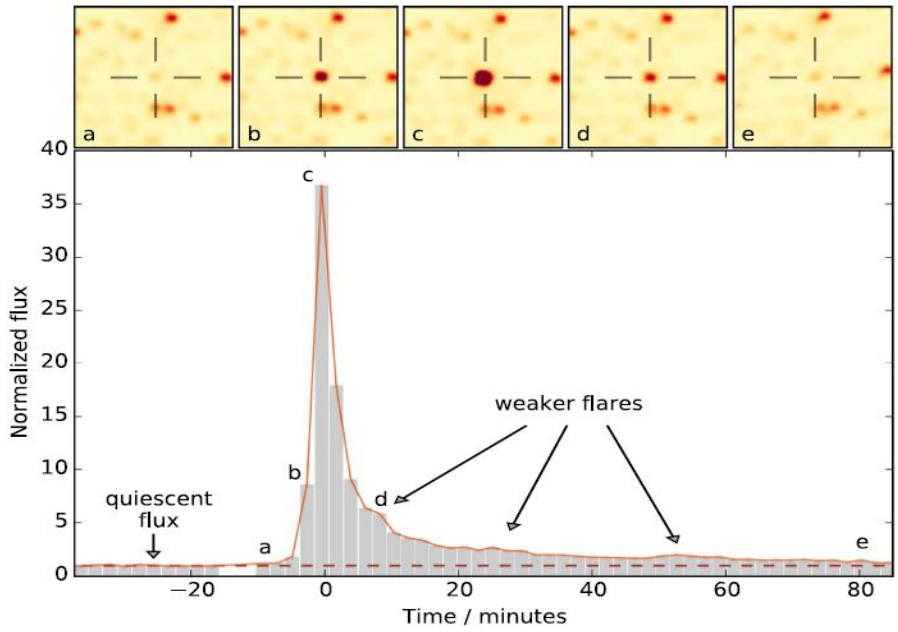

Figure 5.5: Evryscope discovery of a naked-eye-brightness superflare from Proxima. The y-axis is the flux increase over Proxima's median g′-band flux from the previous hour. Bars show the integration time of each individual flux measurement. Insets display cutout images over the course of the flare. For clarity, only one camera's light curve is shown; another Evryscope camera simultaneously observing the event showed a very similar light curve offset by 2.2 s. Plot from [99].

Overall, the addition of stellar wind and XUV radiation leads to atmospheric escape of exoplanets, which induces planetary mass loss. As shown by figure 2.3 in the case of the thermal Jeans escape, lightest chemical species such as hydrogen or helium escape very rapidly, especially around K and M stars with massive hydrogen escape [101]. Besides, non-thermal models predict that the atmospheres of a significant fraction of Earth-like exoplanets orbiting M dwarfs and active K stars and exposed to high XUV fluxes, present a significant atmospheric loss rate of oxygen and nitrogen, which will make them uninhabitable within from a few tens to hundreds of million years because of the low replenishment rate from volcanism or cometary bombardment [102]. In the case of Earth's atmosphere, oxygen has a mean velocity of 0.6 km/s while nitrogen is 2.3 km s^{-1}.

In the next paragraph, as atmospheric escape leads to atmospheric erosion, we study the impact of this atmospheric erosion on the stability of liquid water since water is a molecular mix of hydrogen and oxygen.

3.3.2.2.2 Stability of liquid water

A major consequence of atmospheric erosion due to stellar activity, including XUV flux and stellar wind, remains the loss of water via water vapor photolysis and hydrogen/oxygen escape [103]. The XUV flux and the hydrodynamic stellar winds, both driven by stellar magnetic activity, disrupt the stability of potential surface liquid water on a given super-Earth orbiting a M-dwarf star. As mentioned in the previous section, M-dwarfs, despite their low-mass [0.08 M_{sun} , 0.6 M_{sun}] [103], exhibit long periods of high XUV radiation activity and can significantly desiccate the atmospheres of nearby super-Earths. In addition, the XUV radiation can trigger a runaway greenhouse effect on the surface of a super-Earth, especially on the inner edge and center of the HZ [103], which deeply accelerates the water loss. The location of the super-Earth into the habitable zone set by M-dwarf radiative activity remains also a key factor in the stability of liquid water, as emphasized in figure 5.6 for the case of energy-limited escape of oxygen. This case assumes that the rate of oxygen absorption by surface sinks is much larger than the rate at which it is photolytically produced [103]. It can be encountered on planets with vigorous resurfacing processes or convecting magma oceans [103]. As a result, the oxygen content of the atmospheres of these planets is always low, the upper atmosphere is rich in water vapor, and hydrogen and oxygen escape at the energy-limited rate [103].

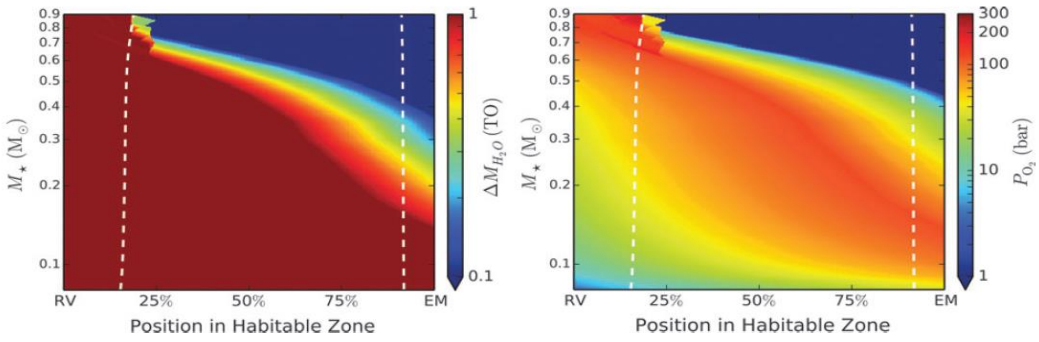

Figure 5.6: Energy-Limited Escape: Total amount of water lost, and amount of oxygen absorbed at the surface for a 1 $M_\oplus$ planet formed at 10 Myr with 1 TO (Terrestrial Ocean) of surface water, assuming the planet is in a runaway interior to the RG (runaway greenhouse) limit, the oxygen is instantaneously absorbed by the surface, and the escape is energy-limited. An expanded view of the HZ is shown in both panels. The solid lines are the empirical HZ bounds; the dashed lines are the theoretical HZ bounds. The axes correspond to the stellar mass (vertical) and the position of the planet within the HZ at 5 Gyr (horizontal). The ‘‘position in habitable zone’’ is the fractional distance between the RV (recent Venus) limit and the EM (Early Mars) limit (the empirical HZ). The dashed lines represent the RG and MG (maximum greenhouse) limits. Left: Total water lost in TO after 5 Gyr. Dark blue corresponds to less than 0.1 TO; dark red corresponds to complete desiccation. Most planets in the HZ of M dwarfs are completely desiccated; conversely, those close to the outer edge of high-mass M dwarfs and throughout most of the HZ of K dwarfs lose little or no water. Interior to the RG (runaway greenhouse) limit, planets around stars of all masses are completely desiccated. Right: Total amount of oxygen absorbed by the surface in bar. Dark blue corresponds to insignificant O_2 buildup; dark red corresponds to 200 bars of oxygen. Planets that lose significant amounts of water also undergo extreme surface oxidation. Plots from [103].

From figure 5.6, planets throughout most of the HZ of M dwarfs are completely desiccated (left panel). For stellar masses larger than $\sim 0.2\ M_{sun}$, planets close to the outer edge of the HZ retain some of their water due to the shorter runaway phase; however, even planets in the center of the HZ of high-mass M dwarfs ($M \gtrsim 0.4\ M_{sun}$) are completely desiccated [103].

Another example of water loss occurring on an Earth-similar planet with assumed Earth-atmospheric type, still in the energy-limited escape paradigm as in figure 5.6, is displayed in figure 5.7. The figure is plotted for an Earth-like planet orbiting a M-dwarf star (AD Leo) and the Sun as a function of their orbital eccentricity and incident flux from their host star, respectively.

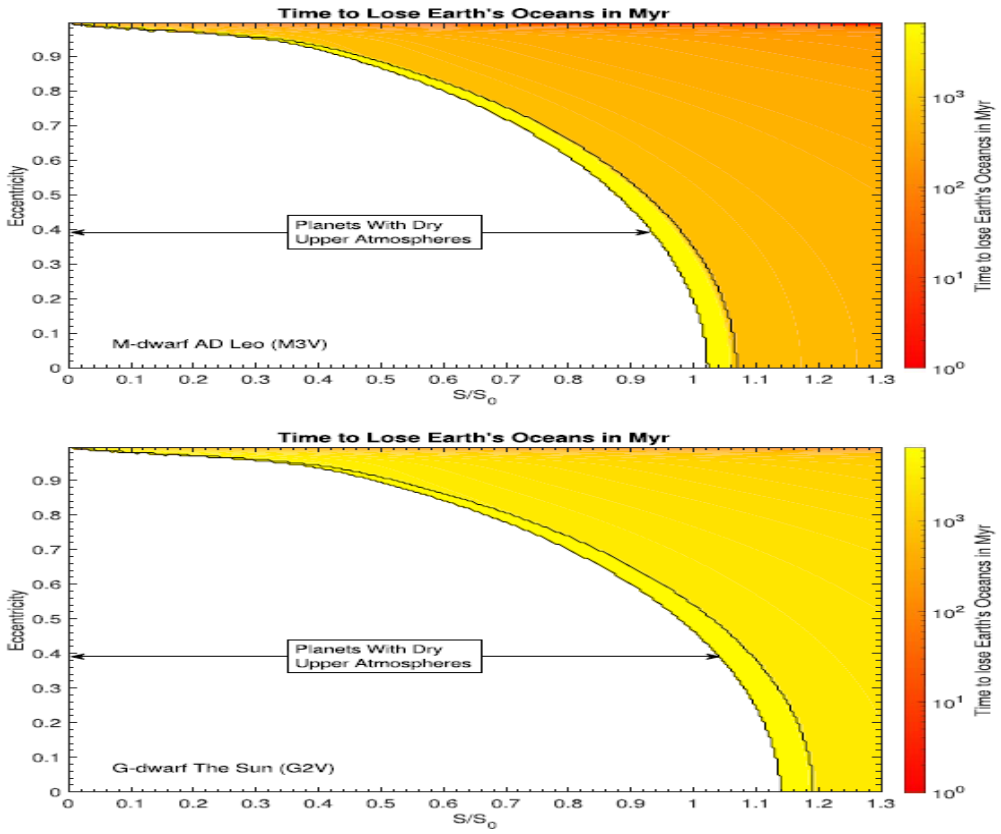

Figure 5.7: Time to lose Earth's entire surface water inventory on aqua planets orbiting M-dwarf AD Leo and G-dwarf star the Sun in Myr. The M-dwarf planet is exposed to ~6×more XUV flux than the G-dwarf planet with an equivalent climate, leading to a ~6×higher mass loss rate. The black contour outlines the boundaries of the moist greenhouse. Plots from [103].

From figure 5.7, it can be concluded that such planet with circular orbit ($e = 0$) lose nearly the equivalent of Earth's entire surface water inventory in less than 1 Gyr that is primarily due to XUV flux six times higher than for an Earth-like planet around a G-type star [104]. This last result is consistent with other results which have shown that similar planets orbiting stars less massive than the Sun lose at least one Earth water surface content will likely have been lost after 5 Gyr for most locations in the HZ due to atmospheric erosion [103].

3.3 Analysis of the Nasa Exoplanet Archive

3.3.1 Purposes and description of the database

In this sub-part, we aim to implement a Python program called *Habitabilita24*, presented in appendix A, to determine which super-Earths could be considered as habitable throughout the analysis of the exoplanets database benchmark known as the Nasa Exoplanet Archive. Additionally, several plots are presented such as the distribution of planetary masses with semi-major and the consistency between computed equilibrium temperatures with formula (i.3) and the values given within the table. However, we ultimately display and derive the number of exoplanets potentially located in their habitable zone by considering their eccentricity, which leads to equilibrium temperature variations.

The database comprises planetary and stellar properties, including mass, radius, planetary equilibrium temperature, stellar effective temperature and other parameters. Furthermore, general information is given such as planet names, publications name, number of planets and host stars per planetary system, stellar host name, as well as the year of discovery, the applied detection method and so on. As of September 17th, 2024, 5759 exoplanet detections have been confirmed [5]. All data are based on Kepler, TESS, CoRot and other space mission observational data.

The Python program has the purpose of establishing a primary analysis of the habitability of super-Earths based on the planetary equilibrium temperature range that allows the stability of liquid water on their surface, i.e between 273 K and 373 K. Indeed, no information is provided about the atmospheric composition of exoplanets although it is a paramount parameter to establish habitability, especially ensuring sufficient atmospheric pressure. A part of the Nasa Exoplanet Archive is shown in figure 5.8.

Planet Name	Host Name	Default Parameter Set	Number of Stars	Number of Planets	Discovery Method	Discovery Year	Discovery Facility	Solution Type	Controversial Flag	Planetary Paramet
11 Com b	11 Com	0	2	1	Radial Velocity	2007	Xinglong Station	Published Confirmed	0	Kunitomo et al. 2011
11 Com b	11 Com	0	2	1	Radial Velocity	2007	Xinglong Station	Published Confirmed	0	Liu et al. 2008
11 Com b	11 Com	1	2	1	Radial Velocity	2007	Xinglong Station	Published Confirmed	0	Teng et al. 2023
11 UMi b	11 UMi	1	1	1	Radial Velocity	2009	Thueringer Lande	Published Confirmed	0	Stassun et al. 2017
11 UMi b	11 UMi	0	1	1	Radial Velocity	2009	Thueringer Lande	Published Confirmed	0	Kunitomo et al. 2011
11 UMi b	11 UMi	0	1	1	Radial Velocity	2009	Thueringer Lande	Published Confirmed	0	Dollinger et al. 2009
14 And b	14 And	1	1	1	Radial Velocity	2008	Okayama Astroph	Published Confirmed	0	Teng et al. 2023
14 And b	14 And	0	1	1	Radial Velocity	2008	Okayama Astroph	Published Confirmed	0	Kunitomo et al. 2011
14 And b	14 And	0	1	1	Radial Velocity	2008	Okayama Astroph	Published Confirmed	0	Sato et al. 2008
14 Her b	14 Her	0	1	2	Radial Velocity	2002	W. M. Keck Obser	Published Confirmed	0	Wittenmyer et al. 200
14 Her b	14 Her	0	1	2	Radial Velocity	2002	W. M. Keck Obser	Published Confirmed	0	Gozdziewski et al. 20

Showing records 1 to 28 of 36404 (36404 total) DOI 10.26133/NEA12 Clear Checked Check All Reset Filters

Figure 5.8: Some data of the Nasa Exoplanet Archive table, regularly updated with increasing number of detections. Image from [5].

3.3.2 Description of the Habitabilita24 program

First and foremost, we load the CSV exoplanet catalog datafile named *nasa exo catalog*, localized in *file_path* and can be read thanks to the Table tool of the Astropy module. The CSV file contains data from the Nasa Exoplanet Archive table shown in figure 5.8.

We filter super-Earths from other exoplanets populations by taking the size and mass ranges mentioned in section 2.2.3: $1\ R_{\oplus} < R_{p,SE} \leq 1.8\ R_{\oplus}$ and $1\ M_{\oplus} < M_{p,SE} \leq 10\ M_{\oplus}$. These radii and masses ranges are assigned to the *super-earths* variable and are found in columns "pl_rade" and "pl_bmasse" of the CSV datafile, where these latter physical parameters are expressed in terms of Earth's radius and mass, respectively.

Then, since we assume a primary habitability based on the planetary equilibrium temperature that enables the stability of liquid water, i.e between 273 K and 373 K. Stellar luminosity is not automatically selected in the table, we can thus compute the luminosity by applying the Stefan-Boltzmann law because stellar radius (in "st_rad" column) and stellar effective temperature (in "st_teff" column) are available in the table. Stellar luminosity is assigned to the *Lstar* variable. As a result, the equilibrium temperature, stocked in the *Tequi* variable, is computed thanks to the stellar luminosity L_{star} and the planet semi-major axis given in the table within the "pl_orbsmax" column.

Overall, we define habitability of super-Earths by setting the equilibrium temperature in the range of temperature suitable for liquid water to exist on the planetary surface, as mentioned in the above paragraph. The array *habitable_super_earths* contain the names and characteristics of the potentially habitable super-Earths by taking the equilibrium temperature criterium for the sustainability of surface liquid water. In the table, the numerical equilibrium temperature is provided by the values of the "pl_eqt" column, and the habitabilita24 program examines if these temperatures data belong to the surface liquid water temperatures range. In addition, a plot is generated to verify the consistency between the equilibrium temperature derived from relation (i.3) and the numerical equilibrium temperatures given in the table, as shown in figure 5.9. The detailed list of habitable super-Earths is given in figure 6.0.

Then, we set a plot showing the distribution of exoplanets of masses expressed in terms of Jupiter mass with respect to their semi-major axis in AU, as shown in figure 6.1. This plot is set with a logarithmic scale on both axes for a better visualization of the datapoints statistical distribution.

Ultimately, the number of habitable zone-extrasolar planets is computed by considering their eccentricity, leading to an indubitable variation of the equilibrium temperature. This drastic temperature variation occurs in the orbital points that are referred to as the apoapsis and periapsis points, i.e the farthest and closest planetary orbital points, respectively. Based on the calculation of the *apoapsis* and *periapsis* variables, we can infer the values of the minimum (*Tequi_mini* variable*)* and maximum (*Tequi_maxi* variable*)* equilibrium temperatures of any planet and displays the list of habitable zone-planets with equilibrium temperatures comprised in the temperature range of surface liquid water.

3.3.3. Results

Therefore, the consistency between the computed equilibrium temperature by the Habitabilita24 Python program and the numerical values of equilibrium temperatures given in the 'pl_eqt' column within the table is displayed in figure 5.9. As a result, the program estimates that ten potentially habitable super-Earths exist, along with the display of their name, mass, radius and average equilibrium temperature, as shown in figure 6.0.

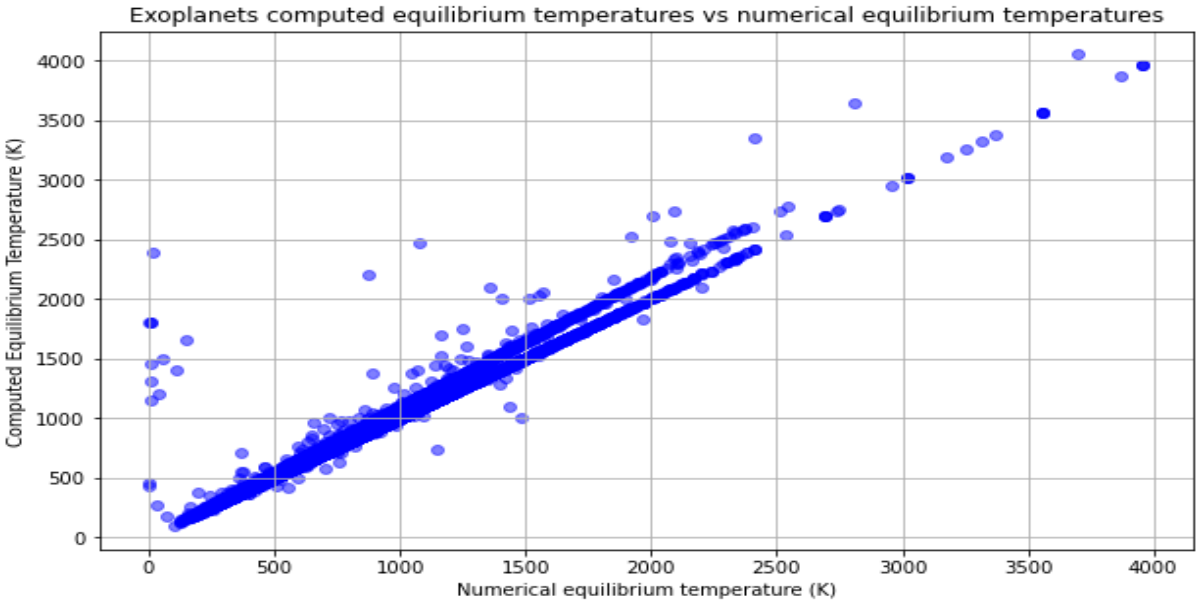

Figure 5.9: Plot showing the linear consistency between the computed equilibrium temperature and the numerical values given in the Nasa Exoplanet Archive table. Plot generated with the program detailed in appendix A.

pl_name	pl_bmasse	pl_rade	pl_eqt
K2-3 c	2.68	1.582	372
K2-3 d	1.6	1.62	312
K2-3 d	2.2	1.458	305
Kepler-138 d	2.1	1.51	345
TOI-1266 c	2.2	1.56	344
TOI-1266 c	6.4	1.673	347
TOI-1452 b	4.82	1.672	326
TOI-2095 b	4.1	1.25	347
TOI-2095 c	7.4	1.33	297
TRAPPIST-1 c	1.38	1.056	342

Figure 6.0: Results obtained with the habitibilita24 Python program, in which ten potentially habitable super-Earths are displayed with their mass ("pl_bmasse", expressed in Earth's mass), radius ("pl_rade", expressed in Earth's radius) and equilibrium temperature ("pl_eqt", expressed in K). These values are obtained with the program given in appendix A.

The plot obtained in figure 6.1 is consistent with Kepler space mission data although it does not only comprise this space mission data because most exoplanets have masses between that of the Earth and Neptune on extremely close orbits (less than 1 AU).

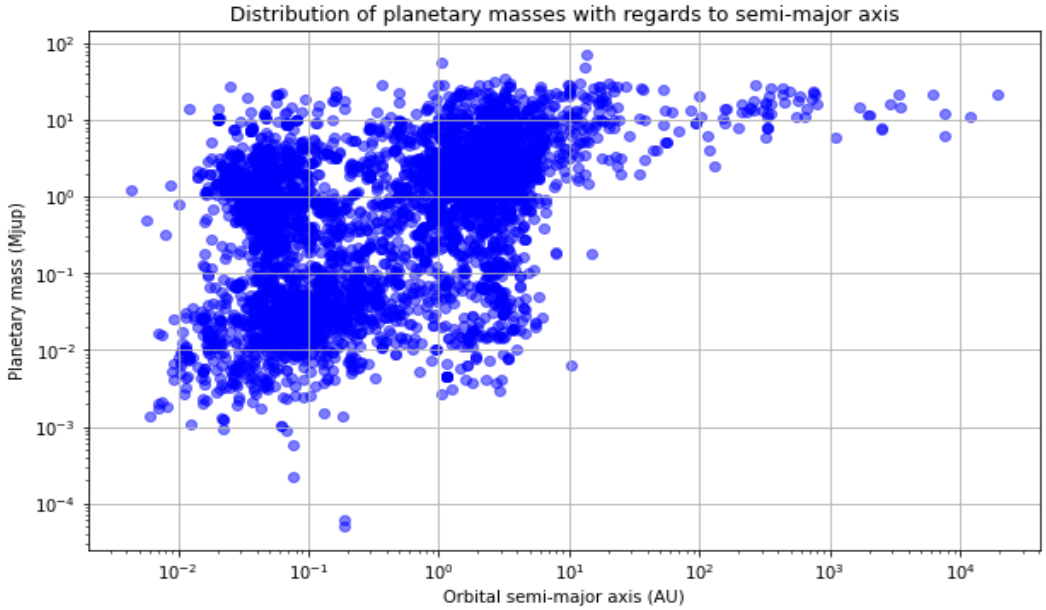

Figure 6.1: Plot showing the logarithmic-scale distribution of exoplanetary masses (in Jupiter mass M_{jup}) with respect to their semi-major axis (in AU). This plot was generated thanks to the python program given in appendix A.

Ultimately, the number of habitable zone-extrasolar planets is evaluated to 798 planets, which seems coherent because the computed values of their equilibrium temperatures are comprised in the temperatures range for the stability of liquid water on their surface. This result gives promising prospects for the search for habitability beyond our Solar System.

Chapter 4

Conclusion and future perspectives

In this thesis, after discussing the fundamental notions of exoplanetology by presenting a synthetic view of the main detection methods and exoplanetary populations, we investigated the potential habitability of the terrestrial planets known as super-Earths by synthetically reviewing literature on such planets. These latter, with typical radius such that $1R_\oplus < R_p < 1.8R_\oplus$ and mass such that $1\,M_\oplus < M_p < 10\,M_\oplus$ ranges represent a unique planetary type because such bodies are not found in our Solar System. Despite their uniqueness in terms of bulk density, these planets are often assimilated to terrestrial planets, especially in terms of internal structure. Differentiation models suggest that their internal structure consists of a crust, silicate-mantle and an iron core, like the Earth interior. However, breaking the interior degeneracy for such exoplanets is challenging because no in-situ data are available. The conventional study of planetary interiors is typically done by applying the seismic-refraction technique, aimed at measuring the speed of seismic waves (section 2.2.3) in different layers, which enables to determine the type of material and the depth of the layer. As a result, super-Earths would likely exhibit common geological processes with Solar System terrestrial planets, including plate tectonics as found on Earth. This process offers the advantage of recycling surface material and the interaction between the surface and the internal structure drives volcanic activity. Volcanic activity then leads to an outgassing mechanism which consists in releasing carbon dioxide, potentially changing the atmospheric composition and contributing to greenhouse effect, affecting surface habitability.

Currently, there is no clear census on the atmospheric composition of super-Earths but given their bulk density and internal structure it can be postulated that their atmosphere is not hydrogen/helium dominated as observed in gas giants or mini-Neptunes. Indeed, the radius distribution of small planets (figure 3.7) presents a significant radius valley between 1.5 $R_\oplus$ and 2.0 $R_\oplus$, particularly at 1.8 $R_\oplus$. This threshold value is set to distinguish super-Earths from sub-Neptunes, these latter are sufficiently massive and large to retain their primordial hydrogen/helium dominated atmosphere while super-Earths likely lose their primordial atmosphere. A clear characterization of super-Earth atmospheres is yet to be confirmed with subsequent transit spectroscopic observations by JWST and future telescopes. As shown in figure 4.2, the full or partial loss of the primordial atmosphere set by the initial protoplanetary disk gaseous composition leads to different atmospheric types. On one hand, complete loss of the primordial atmosphere leads to a secondary atmosphere, whose composition is driven by magma outgassing. As a result, the atmosphere is mostly made of volatiles, including water vapor, methane, nitrogen, carbon dioxide, carbon monoxide and hydrogen leftovers. Secondary atmospheres are thought to be found on terrestrial planets because of their rocky structure that is affected by geological processes, especially plate tectonics. On the other hand, hybrid atmospheres, thought to be super-Earths atmospheric type, have partially lost their primordial atmospheres, potentially due to magma outgassing but with the partial conservation of the initial hydrogen/helium envelope leftover. Hybrid atmospheres also contain volatiles, but where a significant amount of hydrogen and helium is found compared to secondary atmospheres.

As emphasized by the “planets are hard” diagram by Meadows & Barnes (2018), planetary properties are not sufficient factors to sustain habitable conditions. The architecture of the planetary system (section 3.1), including tidal forces between the planet and its moon, as well

as the location of the habitable zone are determinant parameters that can affect the long-term habitability on the surface of a super-Earth. Tidal force can for instance increase the height of waves if there is a significant water surface fraction (e.g water worlds) and induces tidal locking or tidal acceleration, impacting the planetary orbit stability. Overall, the location of the habitable zone, mostly driven by stellar activity, remains one fundamental parameter that controls the climate evolution on the planetary surface, especially leading to potential greenhouse effect if an important amount of instellation is affecting the planet.

Furthermore, since most Milky-Way stars are M-dwarfs, roughly 70% of the galactic stellar population, it is relevant to detect super-Earths around such prevalent stars. Orbiting a M-dwarf offers the advantage of long-term habitability (section 3.2.) because of a longer stellar activity along the main sequence, including XUV emission and stellar winds, thus affecting planet detections via Doppler spectroscopy and transit methods, as well as planetary climate evolution. Indeed, given the relatively small size of super-Earths, stellar activity of M-dwarfs occasionally induces a non-periodic component to the noise floor of the data known as the stellar jitter effect and resulting in a false positive detection, deeply compromising the detection of the exoplanet. Radiative activity of M-dwarfs via XUV and stellar winds emissions in the case of a nearby planet thus potentially leads to atmospheric escape. The addition of atmospheric escape and atmospheric erosion eventually drives water loss via water vapor photolysis and hydrogen/oxygen escape, as shown in figures 5.6 and 5.7.

Then, the filtering analysis of the Nasa Exoplanet Archive (Python program joint in appendix A) was implemented in order to determine how many super-Earths could be potentially habitable. This analysis is an elementary analysis of super-Earths habitability, i.e based on their equilibrium temperature allowing liquid water stability since the atmospheric composition of super-Earths is not provided by the database. Overall, the analysis program finds that ten super-Earths could be potentially habitable, among which one exoplanet of the TRAPPIST-1 system is given. This 7-planet system currently offers an important target for the search of habitable planets since three or four of the seven planets are in the habitable zone [107]. Additionally, the program finds that 798 exoplanets could be located in their habitable zone, which enables to enhance our search for habitable worlds even though the habitability analysis mainly relies on the planetary equilibrium temperature, as well as on the eccentricity for this specific result. Therefore, such results offer promising perspectives for the search of habitability within the rich framework of exoplanetology.

Regarding the perspectives of exoplanetary research, constant improvement of the current instrumentation is indubitably required. For instance, the Extremely Large Telescope (ELT) will represent the next enhanced observational instrument after the Very Large Telescope, fruitful instrumentation developed in the context of the European Southern Observatory (ESO) collaboration. The ELT will be the largest optical ground-based telescope in the years to come and will be able to directly image terrestrial planets in the habitable zone of their host star. The roadmap to the ELT is currently set in the context of the FADE (Forecast system for Atmosphere and Turbulence for ESO) project [105]. It is an automatic forecast system designed to assist observations at ESO, especially by mitigating atmospheric turbulence and aims at reducing the number of out-of-constraints observations due to unforeseen changes in meteorological or optical turbulence changes and best preparing the mode operations of the ELT, especially by gaining experimental insights based on the use of the forecast system [105]. Similarly, another telescope known as the Roman Space Telescope (RST) is scheduled for launch between late 2026 and early 2027 [106]. This telescope, equipped with the Roman Coronograph instrument, will demonstrate high-contrast imaging operations with state-of-the

art technologies [106]. One of the telescope tasks will be to demonstrate 10^{-7} contrast limits at 5σ in a 6–9λ/D area from a star in a broad 10% bandwidth centered at λ= 575 nm (threshold technical requirement, "TTR5"), but is in fact designed to reach better than 10^{-8} contrast limits in the same bandpass and within 3 to 9λ/D from the star [106]. These detection limits will enable us to constrain the visible reflected-light atmospheric characterization of giant extrasolar planets orbiting main-sequence stars as encountered for gas giants distances of the Solar System, i.e between 5 and 10 AU [106]. Nevertheless, the RST represents a milestone in demonstrating key technological capability with regards to the Coronograph instrument, which will be required for the setup of the Habitable Worlds Observatory (HWO). This NASA space mission will allow the unprecedented observations of extrasolar worlds through an extremely broad wavelength window, observed in UV, optical and IR bands [106]. This telescope is scheduled for launch for the 2040 decade and its prime science goal will be to detect biosignatures in potentially habitable exoplanets [106]. To reach this challenging goal, the telescope will be equipped with state-of-the art high-contrast spectro-imaging capabilities, enabling the detection of extrasolar planets that are 10^{10} times fainter than their host stars, which severely contrasts with best current contrast detection limit of 10^{-6} levels [106].

Overall, ongoing research and scheduled space missions must investigate the following fundamental questions:

- What is the fraction of habitable super-Earths in the Milky Way?
- How can we better constrain planetary atmospheres history from observations and models?
- How can factors and processes influencing long-term habitability be measured reliably from models?
- What is the continuous habitability zone in a multiple-star system, and can a planet be considered potentially habitable in such configuration?
- Can the fraction of habitable super-Earths be extrapolated to other spiral galaxies like Andromeda or Milky Way-like galaxies?

Appendix A

Python program for the analysis of the NASA Exoplanet Archive

In this appendix, we present the Habitibilita24 python program that is applied to analyze the Nasa Exoplanet Archive. The script displays the number of habitable super-Earths in the Milky Way, as well as the consistency between equilibrium temperatures estimations and numerical values of the NASA database, the distribution of exoplanetary masses with respect to their semi-major axis and the derivation of the number of habitable zone-planets that accounts for varying equilibrium temperatures due to eccentricity.

```
#Habitabilita24 PROGRAM

from astropy.table import Table
import matplotlib.pyplot as plt


# Global Purpose: assessing the habitability of a catalog of exoplanets taken from the NASA Exoplanet Archive

#Fundamental parameters:

albedo= 0.3 # (spherical Bond albedo for Earth as a reference)
sigma= 5.67E-8 # Stefan-Boltzmann constant in W m**-2 K**-4
pi=3.14159

#I Number of habitable super-Earths in the MW

#i: load the NASA Exoplanet Archive database

file_path="nasa exo catalog.csv"
table=Table.read(file_path,format='csv')

#ii: filter super-Earths from other planets

super_earths =table[(table['pl_bmasse'] > 1) & (table['pl_bmasse'] < 10) & (table['pl_rade'] > 1) & (table['pl_rade'] < 1.8)]

# #iii Computation of the equilibrium temperature

# #iii) 1) computation of the stellar luminosity via Stefan-Boltzmann law
Lstar=S*sigma*Teff**4
```

```
Lstar=4*pi*(table['st_rad']*696340E3)**2*sigma*table['st_teff']**4

# # #iii 2) average planet equilibrium temperature (based on semi-major axis)

Tequi=((Lstar*(1-albedo))/(pi*16*sigma*(table['pl_orbsmax']*1.5E11)**2))**0.25


# #iv create a variable containing habitable super-Earths

habitable_super_earths = super_earths[(super_earths['pl_eqt'] >= 273) &
(super_earths['pl_eqt'] <= 373)]

# # #v display of the list of the potentially habitable super-Earths and their number

habitable_super_earths_count=len(habitable_super_earths)

print(habitable_super_earths[['pl_name', 'pl_bmasse', 'pl_rade', 'pl_eqt']])

print("The number of habitable super-Earths is:",habitable_super_earths_count)


#II Consistency between computed equilibrium temperatures and numerical resuls from the
table

plt.figure(figsize=(10, 6))
plt.scatter(Tequi, table['pl_eqt'], color='blue', alpha=0.5)
plt.title('Exoplanets computed equilibrium temperatures vs numerical equilibrium
temperatures')
plt.xlabel('Numerical equilibrium temperature (K)')
plt.ylabel('Computed Equilibrium Temperature (K)')
plt.grid(True)
plt.xscale('linear')
plt.yscale('linear')
plt.show()


#III Distribution of planetary mass vs semi-major axis

planet_mass=table['pl_bmassj']
semi_major_axis=table['pl_orbsmax']


plt.figure(figsize=(10, 6))
plt.scatter(semi_major_axis, planet_mass, color='blue', alpha=0.5)
plt.title('Distribution of planetary masses with regards to semi-major axis')
plt.xlabel('Orbital semi-major axis (AU)')
plt.ylabel('Planetary mass (Mjup)')
plt.grid(True)
plt.yscale('log')
plt.xscale('log')
```

```
plt.show()


#IV Number of habitable zone-exoplanets

#vi: computation of the minimum and maximum equilibrium temperatures for an eccentric orbit and number of habitable zone-exoplanets

apoapsis=table['pl_orbsmax']*(1+table['pl_orbeccen']) # farthest distance to the star
periapsis=table['pl_orbsmax']*(1-table['pl_orbeccen']) #closest distance to the star

Tequi_maxi=((Lstar*(1-albedo))/(pi*16*sigma*(periapsis*1.5E11)**2))**0.25 #equilibrium temperature corresponding to the apoaxis
Tequi_mini=((Lstar*(1-albedo))/(pi*16*sigma*(apoapsis*1.5E11)**2))**0.25

habitable_zone_planets= table[(Tequi_mini>=273) & (Tequi_maxi<=373)]

print("The number of habitable zone-planets is
:",habitable_zone_planets[['pl_name','pl_rade','pl_bmasse','pl_eqt']])
habitable_zone_planets_count=len(habitable_zone_planets)
print(habitable_zone_planets_count)
```

Bibliography

[1] W. McDonough & T. Yoshizaki. *Terrestrial planet compositions controlled by accretion disk magnetic field*. Progress in Earth and Planetary Science, volume 8, issue 1, 2021.

[2] M. Yildiz et al. *Structure and composition of Jupiter, Saturn, Uranus and Neptune under different constraints and distortion due to rotation.* Monthly Notices of the Royal Astronomical Society, volume 528, issue 4, pages 6881-6894, 2024.

[3] NASA/JPL-Caltech. *Oort cloud and scale of the solar system (infographic)*, PIA22921, https://science.nasa.gov/resource/oort-cloud-and-scale-of-the-solar-system-infographic/#hds-sidebar-nav-1, 2018.

[4] M. Mayor & D. Queloz. *A Jupiter-mass companion to a solar-type star*. Nature, volume 378, pages 355–359, 1995.

[5] NASA Exoplanet Science Institute, *NASA Exoplanet Archive.* https://exoplanetarchive.ipac.caltech.edu/, 2024.

[6] N. Kitadai & S. Maruyama. *Origins of building blocks of life.*, Geoscience Frontiers, volume 9, issue 4, 2016.

[7] S. Kauffman et al. *Theory of chemical evolution of molecules compositions in the universe, in the Miller-Urey experiment and the mass distribution of interstellar and intergalactic molecules.* Journal of Theoretical Biology, volume 486, article 110097, 2020.

[8] L. Feng. *Nebula-Relay Hypothesis: Primitive Life in Nebula and Origin of Life on Earth.* Acta Astronomica Sinica, volume 62, no.3, 2021.

[9] I. de Pater & J. Lissauer. *Planetary Sciences, Updated Second Edition.* Cambridge University Press, 2015.

[10] F. Wesball et al. *The habitability of Venus.* Space Science Reviews, volume 219, issue 2, 2023.

[11] J. Kimura & N. Kitadai. *Polymerization of building blocks of life on Europa and other icy moons.* Astrobiology, volume 15, issue 6, pages 430-441, 2015.

[12] M. Lingam et al. *A Light Sail Astrobiology Precursor to Enceladus and Europa.* Acta Astronautica, volume 218, pages 251-268, 2024.

[13] R. Dayton-Oxland et al. *In-situ detection of Europa's water plumes is harder than previously thought.* Icarus, volume 395, article 115488, 2023.

[14] J. Wright & B. Gaudi. *Exoplanet Detection Methods.* Chapter 59 in *Planets Stars, and Stellar Systems* by T. Oswald et al, volume 3. Springer Reference, 2013.

[15] G. Chauvin. *Direct imaging of exoplanets: Legacy and prospects.* Comptes Rendus. Physique, Online first, pages 1-22, 2023.

[16] J.-P. Folcher et al. *Adaptive optics feedback control.* Refereed chapter in *New Concepts in Imaging: Optical and Statistical Models* by D. Mary C. Theys and C. Aime. EAS Publications Series, volume 59, pages 93-130, 2013.

[17] G. Kathuria. *Comparative analysis between the Hubble Space Telescope and the James Webb Space Telescope.* International Journal of Research and Analytical Reviews (IJRAR), volume 9, issue 4, 2022.

[18] J.-L. Beuzit et al. *SPHERE: the exoplanet imager for the Very Large Telescope.* Astronomy & Astrophysics, volume 631, id.A155, 2019.

[19] B. Gaudi. *Exoplanetary Microlensing.* Referred chapter in *Exoplanets* by S. Seager. The University of Arizona Press, 2011.

[20] F. De Paolis et al. *The Scales of Gravitational Lensing. Universe,* volume 2, issue 1, 2016.

[21] P. Schneider et al. *Gravitational lenses.* Astronomy and Astrophysics Library, Springer, second printing, 1999.

[22] A. Cassan et al. *One or more bound planets per Milky Way star from microlensing observations.* Nature 481, 167-169, 2012.

[23] R. Pudritz et al. *Planetary Systems and the Origins of Life.* Cambridge University Press, 2007.

[24] C. Lovis & D. Fischer. *Radial Velocity Techniques for Exoplanets*. Referred chapter in *Exoplanets* by S. Seager. The University of Arizona Press, pages 27-53, 2010.

[25] Borucki et al. *A 2.4 Earth-radius Planet in the Habitable Zone of a Sun-like Star.* The Astrophysical Journal, volume 745, issue 2, 2012.

[26] J. Winn. *Transits and Occultations.* Referred chapter in *Exoplanets* by S. Seager. The University of Arizona Press, pages 55-77, 2010.

[27] N. Madhusudhan et al. *Carbon-bearing Molecules in a Possible Hycean Atmosphere.* The Astrophysical Journal Letters, volume 956, issue 1, 2023.

[28] D. Catling & K. Zahnle. *The Planetary Air Leak.* Scientific American, volume 300, issue 5, pages 36-43, 2009.

[29] Y. Ito & M. Ikoma. *Hydrodynamic Escape of Mineral Atmosphere from Hot rocky Exoplanet. I. Model Description.* Monthly Notices of the Royal Astronomical Society, volume 502, issue 1, pages 750-771, 2021.

[30] R. Helled et al. *Uranus and Neptune: Origin, Evolution and Internal Structure.* Space Science Reviews, volume 216, issue 3, 2020.

[31] R. Helled & J J. Fortney. *The interiors of Uranus and Neptune: current understanding and open questions.* Philosophical Transactions of the Royal Society A, volume 378, issue 2187, 2020.

[32] A. G-Mesa et al. *Chemical diversity of the atmospheres and interiors of sub-Neptunes: a case study of GJ 436 b.* Monthly Notices of the Royal Astronomical Society, volume 513, issue 3, pages 4015-4036, 2022.

[33] L. Rogers. *Most 1.6 Earth-radius Planets are Not Rocky.* The Astrophysical Journal, volume 801, issue 1, 2015.

[34] T. Cavalié et al. *The Deep Composition of Uranus and Neptune from In Situ Exploration and Thermochemical Modeling.* Space Science Reviews, volume 216, issue 4, 2020.

[35] E. Bailey & D J. Stevenson. *Thermodynamically Governed Interior Models of Uranus and Neptune.* The Planetary Science Journal, volume 2, issue 2, 2021.

[36] P. Bodenheimer & J. B. Pollack. *Calculations of the accretion and evolution of giant planets: The effects of solid cores.* Icarus, volume 67, issue 3, pages 391-408, 1986.

[37] S. Seager et al. *Mass-Radius Relationships for Solid Exoplanets.* The Astrophysical Journal, volume 669, issue 2, pages 1279-1297, 2007.

[38] G. Chabrier et al. *A New Equation of State for Dense Hydrogen- Helium Mixtures.* The Astrophysical Journal, volume 872, issue 1, 2019.

[39] J. Haldermann et al. *AQUA: a collection of H20 equations of state for planetary models.* Astronomy & Astrophysics, volume 643, 2020.

[40] R. Hueso et al. *Convective storms and atmospheric vertical structure in Uranus and Neptune.* Philosophical Transactions of the Royal Society A, volume 378, issue 2187, 2020.

[41] J. Moses et al. *Atmospheric chemistry on Uranus and Neptune.* Philosophical Transactions of the Royal Society A, volume 378, issue 2187, 2020.

[42] M. Malik et al. *HELIOS: AN OPEN-SOURCE, GPU-ACCELERATED RADIATIVE TRANSFER CODE FOR SELF-CONSISTENT EXOPLANETARY ATMOSPHERES.* The Astronomical Journal, volume 153, issue 2, 2017.

[43] M. Malik et al. *Self-luminous and Irradiated Exoplanetary Atmospheres Explorer with HELIOS.* The Astronomical Journal, volume 157, issue 5, 2019.

[44] J. Fortney et al. *Hot Jupiters: Origins, Structure, Atmospheres.* Journal of Geophysical Research, volume 126, issue 3, 2021.

[45] D. Thorngren & J. Fortney. *Bayesian Analysis of Hot Jupiters Radius anomalies: Evidence for Ohmic Dissipation?* The Astronomical Journal, volume 155, issue 5, 2018.

[46] P. Sarkis et al. *Evidence of three mechanisms explaining the radius anomaly of hot Jupiters.* Astronomy & Astrophysics, volume 645, 2021.

[47] L. Teinturier et al. *The radiative and dynamical impact of clouds in the atmosphere of the hot Jupiter WASP-43b.* Astronomy and Astrophysics, volume 683, 2024.

[48] W. Pluriel. *Hot Exoplanetary Atmospheres in 3D.* Remote Sensing, volume 15, issue 3, 2023.

[49] S. Notsu et al. *The composition of hot Jupiter atmospheres assembled within chemically evolved protoplanetary discs.* Monthly Notices of the Royal Astronomical Society, volume 499, issue 2, pages 2229-2244, 2020.

[50] T. Guillot. *On the radiative equilibrium of irradiated planetary atmospheres.* Astronomy and Astrophysics, volume 520, 2010.

[51] B. Hansen. *On the Absorption and Redistribution of Energy in Irradiated Planets.* The Astrophysical Journal Supplement Series, volume 179, issue 2, pages 484-508, 2008.

[52] L. Parc et al. *From super-Earths to sub-Neptunes: Observational constraints and connections to theoretical models.* Astronomy & Astrophysics, volume 688, 2024.

[53] B. Fulton et al. *The California-Kepler Survey. III. A Gap in the Radius Distribution of Small Planets.* The Astronomical Journal, volume 154, issue 3, 2017.

[54] J. Owen & Y. Wu. *The Evaporation Valley in the Kepler Valley.* The Astrophysical Journal, volume 847, issue 1, 2017.

[55] S. Jin & C. Mordasini. *Compositional Imprints in Density-Distance-Time: A Rocky Composition for Close-in Low mass Exoplanets from the Location of the Valley of Evaporation.* The Astrophysical Journal, volume 853, issue 2, 2018.

[56] S. Ginzburg et al. *Core-powered mass loss and the radius distribution of small exoplanets.* Monthly Notices of the Royal Astronomical Society, volume 476, issue 1, pages 759-765, 2018.

[57] A. Gupta & H. Schlichting. *Sculpting the valley in the radius distribution of small exoplanets as a by-product of planet formation: the core-powered mass loss mechanism.* Monthly Notices of the Royal Astronomical Society, volume 487, issue 1, pages 24-33, 2019.

[58] H. Tanaka et al. *Three-Dimensional Interaction between a Planet and an Isothermal Gaseous Disk. I. Corotation and Lindblad Torques and Planet Migration.* The Astrophysical Journal, volume 565, issue 2, pages 1257-1274, 2002.

[59] J. Eager et al. *Unveiling the internal structure and formation history of the three planets transiting HIP 29442 (TOI-469) with CHEOPS*.* Astronomy & Astrophysics, 2024.

[60] A. Boujibar et al. *Super-Earths Internal Structures and Initial Thermal States.* Journal of Geophysical Research: Planets, volume 125, issue 5, 2020.

[61] A. Oganov. *Thermodynamics, Phase Transitions, Equations of State, and Elasticity of Minerals at High Pressures and Temperatures.* Treative on Geophysics, pages 121-152, 2007.

[62] P. Vinet et al. *Universal features of the equation of state of solids.* Journal of Physics: Condensed Matter, volume 1, pages 1941-1963, 1989.

[63] P. Driscoll & Z. Du. *Geodynamo Conductivity Limits.* Geophysical Research Letters, volume 46, issue 14, pages 7982-7989, 2019.

[64] H. van Heck & P. Tackley. *Plate tectonics on super-Earths: Equally or more likely than on Earth.* Earth and Planetary Science Letters, volume 310, issue 3, pages 252-261, 2011.

[65] D. Turcotte & G. Schubert. *Geodynamics: Application of Continuum Physics to Geological Problems.* Wiley & Sons, 1982.

[66] M. Tian & K. Heng. *Atmospheric Chemistry of Secondary and Hybrid Atmospheres of Super-Earths and Sub-Neptunes.* The Astrophysical Journal, volume 963, issue 2, 2024.

[67] P. Figueira et al. *Bulk composition of the transiting hot Neptune around GJ 436.* Astronomy & Astrophysics, volume 493, issue 2, pages 671-676, 2009.

[68] L. Rogers et al. *Formation and Structure of Low-density exo-Neptunes.* The Astrophysical Journal, volume 738, issue 1, pages 738-759, 2011.

[69] J. Fortney et al. *A Framework for Characterizing the Atmospheres of Low-mass Low-density Transiting Planets.* The Astrophysical Journal, volume 775, issue 1, 2013.

[70] L. Alderson et al. *JWST COMPASS: NIRSpec/G395H Transmission Observations of the Super-Earth TOI-836b.* The Astronomical Journal, volume 167, issue 5, 2024.

[71] F. Hawthorn et al. *A super-Earth and mini-Neptune transiting a nearby K-dwarf.* Monthly Notices of the Royal Astronomical Society, volume 520, issue 3, pages 3649-3668, 2023.

[72] L. Alderson et al. *Early Release Science of the exoplanet WASP-39b with JWST NIRSpec G395H.* Nature, volume 614, pages 664-669, 2023.

[73] T. Bell et al. *Eureka! : An End-to-End Pipeline for JWST Time-Series Observations.* The Journal of Open Source Software, volume 7, issue 79, 2022.

[74] T. Jansen et al. *Climates of Warm Earth-like Planets. II. Rotational "Goldilocks" Zones for Fractional Habitability and Silicate Weathering.* The Astrophysical Journal, volume 875, issue 2, 2019.

[75] S. Guzewich et al. *The Impact of Planetary Rotation Rate on the Reflectance and Thermal Emission Spectrum of Terrestrial Exoplanets around Sunlike Stars*. The Astrophysical Journal, volume 893, issue 2, 2020.

[76] J. Laskar & P. Robutel. *The chaotic obliquity of the planets.* Nature, volume 361, pages 608-612, 1993.

[77] P. Vervoort et al. *System Architecture and Planetary Obliquity: Implications for Long-term Habitability*. The Astronomical Journal, volume 164, issue 4, 2022.

[78] S. Kane. *Planetary Habitability*. The American Astronomical Society, IOP Publishing, 2021.

[79] J. Kasting et al. *Habitable Zones around Main Sequence Stars.* Icarus, volume 101, issue 1, pages 108-128, 1993.

[80] G. Habets & J. Heintze. *Empirical bolometric corrections for the main sequence.* Astronomy and Astrophysics Supplement Series, volume 46, pages 193-237, 1981.

[81] D. Whitmire & R. Reynolds. *Circumstellar Habitable Zones: Astronomical Considerations.* Edited by L. Doyle. Travis House Publications, pages 118-142, 1996.

[82] R. Kopparapu et al. *Habitable Zones around Main-sequence Stars: New Estimates.* The Astrophysical Journal, volume 765, issue 2, pages 131-146, 2013.

[83] S. Kane et al. *A Catalog of Kepler Habitable Zone Exoplanet Candidates.* The Astrophysical Journal, volume 830, issue 1, 2016.

[84] R. Kopparapu et al. *Habitable Zones around Main-sequence Stars: Dependence on Planetary Mass.* The Astrophysical Journal Letters, volume 787, issue 2, 2014.

[85] A. Shields et al. *The habitability of planets orbiting M-dwarf stars.* Physics Reports, volume 663, 2016.

[86] C. Lineweaver et al. *The Galactic Habitable Zone and the Age Distribution of Complex Life in the Milky Way*. Science, volume 303, issue 5654, 2004.

[87] L. Chomiuk & M. Povich. *Toward a Unification of Star Formation Rate Determinations in the Milky Way and Other Galaxies.* The Astronomical Journal, volume 142, issue 6, 2011.

[88] G. Kuiper. *The Empirical Mass-Luminosity Relation.* The Astrophysical Journal, volume 88, pages 472-507, 1938.

[89] L. Sackmann et al. *Our Sun. III. Present and Future.* The Astrophysical Journal, volume 418, pages 457-468, 1993.

[90] W. Morgan & P. Keenan. *Spectral Classification.* Annual Review of Astronomy and Astrophysics, volume 11, pages 29-50, 1973.

[91] European Southern Observatory (ESO). *Hertzsprung-Russel Diagram.* https://www.eso.org/public/unitedkingdom/images/eso0728c/, 2007.

[92] J. Bochanski et al. *The Luminosity and Mass Functions of Low-mass Stars in the Galactic Disk. II. The Field.* The Astronomical Journal, volume 139, issue 6, pages 2679-2699, 2010.

[93] I. Boisse et al. *Disentangling between stellar activity and planetary signals.* Astronomy & Astrophysics, volume 528, 2011.

[94] E. Newton et al. *The Rotation and Galactic Kinematics of Mid M Dwarfs in the Solar Neighborhood***.** The Astrophysical Journal, volume 821, issue 2, 2016.

[95] F. Hesar et al. *Advancing Machine Learning for Stellar Activity and Exoplanet Period Rotation.* Astronomy & Astrophysics, 2024.

[96] S. Boldt et al. *Stellar activity consequence on the retrieved transmission spectra through chromatic Rossiter-McLaughlin observations.* Astronomy & Astrophysics, volume 635, 2020.

[97] G. Anglada-Escudé et al. *A terrestrial planet candidate in a temperate orbit around Proxima Centauri.* Nature, volume 536, issue 7617, pages 437-440, 2016.

[98] J. Zuluaga et al. *Magnetic properties of Proxima Centauri b analogues.* Planetary and Space Science, volume 152, pages 55-67, 2018.

[99] W. Howard et al. *The First Naked-eye Superflare Detected from Proxima Centauri.* The Astrophysical Journal Letters, volume 860, issue 2, 2018.

[100] I. Ribas et al. *The habitability of Proxima Centauri b. I. Irradiation, rotation and volatile inventory from formation to the present.* Astronomy & Astrophysics, volume 596, 2016.

[101] J. M. Rodríguez-Mozos & A. Moya. *Erosion of an exoplanetary atmosphere caused by stellar winds.* Astronomy & Astrophysics, volume 630, 2019.

[102] V. Airapetian et al. *How Hospitable Are Space Weather Affected Habitable Zones? The Role of Ion Escape*. The Astrophysical Journal Letters, volume 836, issue 1, 2017.

[103] R. Luger & R. Barnes. *Extreme Water Loss and Abiotic O2 Buildup on Planets Throughout the Habitable Zones of M Dwarfs*. Astrobiology, volume 15, issue 2, 2015.

[104] I. Palubski et al. *Habitability and Water Loss Limits on Eccentric Planets Orbiting Main-sequence Stars*. The Astrophysical Journal, volume 890, issue 1, 2020.

[105] E. Masciadri et al. *FATE - an operational automatic system for optical turbulence forecasting at the Very Large Telescope.* SPIE Conference Proceedings, volume. 13097, eprint arXiv:2409.05133, 2024.

[106] E. Choquet et al. *ESCAPE project: investigating active observing strategies and post-processing methods for exoplanet high-contrast imaging with future space missions***.** Proceedings of the 2024 SPIE Astronomical Telescopes + Instrumentation conference, eprint arXiv:2409.02019, 2024.

[107] M. Gialluca et al. *The Implications of Thermal Hydrodynamic Atmospheric Escape on the TRAPPIST-1 Planets.* The Planetary Science Journal, volume 5, issue 6, 2024.

Acknowledgements

Beforehand, I want to acknowledge my thesis advisor, Prof. Leonardo Testi, for his invaluable guidance, encouragement, and expertise. Your insights and constructive feedback have been significant in shaping my research and enhancing my understanding of the field of exoplanetary science.

I am also appreciative to all the professors of the DIFA during the two years of the program for their inspiring lectures and relevant support for the exams. Your rich expertise in various fields of astrophysics has deeply enriched my work and inspired me to think critically about my research.

Subsequently, I want to extend my appreciation to my colleagues for their camaraderie, collaboration and constructive advice, in particular Alessio, Sekhar, Lorenzo, and Davide. The stimulating discussions and shared experiences have made this journey enjoyable and fulfilling.

Next, I want to express my gratitude to all researchers and visiting lecturers at the 7th Institute of Space Science (ICE) Summer School: Multiwavelength Approach to Exoplanetary Systems for providing a broad complementary knowledge of exoplanetary science, which was of crucial importance for my thesis work.

A special thanks to my family and friends for their unconditional support and encouragement. Your belief in my abilities has motivated me to persevere through challenges and strive for excellence.

Ultimately, I would like to acknowledge all exoplanetary researchers who have been constantly improving the understanding of exoplanets by their groundbreaking publications, as well as underlining the richness of their results. In addition, I would like to acknowledge the resources and data provided by the NASA Exoplanet Archive and the various observatories that have contributed to the field of exoplanet research. Their work has paved the foundation for my own research and has been truly a source of inspiration.

Thank you all for being part of this rewarding journey.